2010

Investigating Breast Cancer Metastasis to the Brain with Cellular MRI

Mevan Perera
Western University

Investigating Breast Cancer Metastasis to the Brain with Cellular MRI

(Spine Title: Investigating Breast Cancer Metastasis to the Brain with Cellular MRI

(Thesis Format: Integrated Article)

by

Mevan Perera

Graduate Program

in

Medical Biophysics

Submitted in partial fulfillment
of the requirements for the degree of
Master of Science

School of Graduate and Postdoctoral Studies
The University of Western Ontario
London, Ontario
August 2010

THE UNIVERSITY OF WESTERN ONTARIO
FACULTY OF GRADUATE STUDIES

Certificate of Examination

Supervisor

Paula J. Foster, Ph.D.

Examining Board

Dwayne N. Jackson, Ph.D

Giles Santyr, Ph.D

Alison Allan, Ph.D

The thesis by

Mevan Perera

entitled:

INVESTIGATING BREAST CANCER METASTASIS TO THE BRAIN WITH CELLULAR MRI
is accepted in partial fulfillment
of the requirements for the degree of
Master of Science

Date

Chair of Examining Board

Abstract

Brain metastasis due to breast cancer is a devastating complication that effects many people every year and its prognosis is dismal, fewer than 20% of patients reach the one year survival period after initial diagnosis. Herein we report the temporal and spatial monitoring of the development of experimental brain metastasis in mice. The metastatic potential of two highly brain metastatic breast cancer cell lines was investigated in vivo at multiple time points. This involved comparing distribution patterns, growth rates and tumor volumes between the two cell lines. We also labeled cells with MPIO contrast agents and tracked the distribution of cells on day 1 in the brain using MRI, the finding was correlated to the corresponding distribution of metastases at the endpoint. This model gives new insight into the nature of breast cancer metastasis to the brain and is a piece to the puzzle for solving this complex disease.

Keywords: Magnetic Resonance Imaging (MRI); brain metastasis; breast cancer; mouse model; MPIO.

Acknowledgments

First and foremost I would like to thank my supervisor Dr. Paula Foster for all of her help and guidance over the last two years. I thank her for having faith and patience in me through all of my setbacks and struggles. Being under her tutelage has been an invaluable experience; I have matured and grown as a person and student of science. Most importantly after the last two years I can consider her to be a friend. I would also like to acknowledge members of my advisory committee Drs. Ann Chambers and Lynne-Marie Postovit for their help and guidance throughout my project.

I would also like to thank all members of the Foster lab whose help and support has benefitted me throughout my time here. I would especially like to thank Emeline Ribot, Christiane Mallett, Shruti Krishnamoorty, Jenny Noad, Vasiliki Economopolous, Catherine McFadden, Jon Snir, Roja Rohani and Carmen Simedrea for making me laugh and helping me get through my day.

Finally I would like to thank my parents, brother for their love and support over the last two years. I would also like to thank the friends that I have made over the last two years for showing me there is a life outside of graduate school.

TABLE OF CONTENTS

List of Figures

List of Tables

List of Equations

List of Acronyms and Abbreviations

ADC	Apparent diffusion coefficient
ASL	Arterial spin labeling
BBB	Blood Brain Barrier
BLI	Bioluminescence imaging
b-SSFP	Balanced Steady State Free Precession
CAM	Cellular Adhesion Molecules
CNR	Contrast to Noise Ratio
CT	Computed Tomography
DCE	Diffusion Contrast Enhanced MRI
DMEM	Dulbecco's modified Eagle's medium
DSW	Dynamic Susceptibility Weighted MRI
EAE	Autoimmune encephalomyelitis
ECM	Extracellular matrix
EGF	Epidermal Growth Factor
EGFP	enhanced green fluorescent protein
FA	Flip angle
FBS	Fetal Bovine Serum
FID	Free Induction Decay
FBV	Fractional blood volume
FOV	Field of view
Gd	Gadolinium
Gd-DTPA	Gadopentate dimeglumine
GFP	Green fluorescent protein
GRE	Gradient Echo
H&E	Hematoxylin and eosin
HBSS	Hank's Balanced Salt Solution
HER2	Human epithelial growth factor receptor-2
ICP-MS	Inductively coupled plasma mass spectroscopy
IV	Intravenous
IVVM	Intravital Vidoemicroscopy
K	Permeability
MPIO	Micron-Sized Superparamagnetic Iron-Oxide
MRI	Magnetic Resonance Imaging
MS	Multiple Sclerosis
MHz	Megahertz
NEX	Number of averages
NMR	Nuclear Magnetic Resonance
PBS	Phosphate Buffered Saline
PET	Positron Emission Tomography
PLL	Poly-L-Lysine
PPB	Perl's Prussian Blue
rBW	Receiver bandwidth
rCBV	relative cerebral blood volume

RF	Radiofrequency
SE	Spin Echo
SNR	Signal to Noise Ratio
SPECT	Single photon emission computed tomography
SPIO	Superparamagnetic Iron Oxide
SSFP	Steady State Free Precession
T	Tesla
TE	Echo Time
TEM	Transmission electron microscopy
TR	Repition Time
US	Ultrasound
USPIO	Ultrasmall Superparamagnetic Iron-Oxide
VEGF	Vascular Endothelial Growth Factor

List of Symbols

S	Spin Angular momentum
s	nuclear spin
μ	magnetic moment
M	magnetization
M_0	net magnetization
Mz	magnetization on z-axis
B_0	main magnetic field
T	Tesla
ω_0	larmour frequency
α	RF pulse

List of Appendices

Chapter 1: Introduction

1.1 Metastasis

1.1.1 Breast Cancer

Breast cancer remains a serious, life-threatening disease that can affect anyone. An estimated 23,200 Canadian women will be diagnosed with breast cancer and 5,300 will die from it in 2010 (1).

1.1.2 Metastasis

The majority of breast cancer deaths are due to the occurrence of systemic metastases (1). Metastasis is the spread of malignant cells from the original tumor. The spreading of cancer cells causes 90% of deaths related to solid tumors (2). The process of metastasis is best described by a series of events known as the "metastatic cascade" (3). The sequence of events includes: detachment, intravasation, transport, extravasation, colonization, and angiogenesis (4). Once a normal cell has acquired the genetic changes that transform it into a tumor cell, the detachment process begins. Cellular Adhesion Molecules (CAMs) are cell surface proteins that allow binding of cells to each other, or to the extracellular matrix (ECM) (5). Metastatic tumor cells have the ability to turn off and on various CAMs and gain the ability to detach from the tumor mass and invade underlying stroma (6). Tumor cells destined to form metastases move toward the circulation, this is the process known as

intravasation (7). The cells breach and degrade the basement membrane and ECM by releasing various proteolytic enzymes that target a number of different proteins including collagens, laminin and fibronectin (7). Once in the circulation cancer cells are most vulnerable to the elements of the immune system and must withstand the assault from natural killer cells, macrophages, as well as endure the shear forces attributed to increased blood velocity (8). Cancer cells overcome these transport obstacles by associating themselves with platelets and leukocytes, which can act as escorts (9). Selectins, a subset of CAMs, allow tumor cells to attach to platelets and leukocytes and thus facilitate their transport (9). The circulating tumor cells eventually arrest in a vascular bed and this process of arrest is related to the size of the cell relative to the capillary bed (10-12). Capillaries are small (approximately 3-8μm in diameter) and are designed to allow the passage of red blood cells – which average 7 μm in diameter and are highly deformable – whereas many cancer cells are quite large (20 μm or more in diameter). Cancer cells that arrest due to size restriction in any organ will be determined by physical factors, such as the relative sizes of cells and the capillaries, the blood pressure in the organ and the deformability of the cell (41). Like intravasation, extravasation involves cancer cells releasing various proteolytic enzymes that breakdown the ECM and surrounding endothelial cell layer to gain access to the tissue parenchyma (13). Colonization is considered the rate-limiting step of the metastatic cascade; if the cancer cells are unable to grow and form a mass they usually die (14).

In 1889, Dr. Stephen Paget proposed the "seed" and "soil" theory to describe the nature of metastasis; where the seed is the cancer cell and its

survival or ability to germinate into a tumor mass is dependant on the "soil" or tissue microenvironment (15). Since then the propensity for metastatic tumors to develop in specific organs has been demonstrated (16-18). An opposing theory for metastasis which was proposed by American pathologist James Ewing in 1928 stated that cancer cells are not predisposed to develop in certain tissues and the site of metastasis is only dependent on mechanical factors, such as the location of the primary tumor and circulatory patterns (41). Studies have appeared that support both of these theories (19-21); however it is accepted that metastasis is likely a mixture of both of these theories and that one is not exclusive from the other (22).

It is widely accepted that metastasis is an inefficient process particularly at the point of colonization (22). One study involving a metastatic mouse model and melanoma cells found that 80% of cells survived up to the point of extravasation, however less than 3% formed micrometastases and only 1% continued to form clinically apparent metastases (23).

Angiogenesis is the final step of the metastatic cascade; a tumor cannot grow beyond 1 to 2 mm^3 unless it acquires its own blood supply (24, 25). Vascular endothelial growth factor (VEGF) and epidermal growth factor (EGF) are known to induce new blood vessel formation (26, 27). A long list of cytokines, growth factors, immunologic mediators, and molecular pathways play a role. Not all of the mechanisms and factors that drive this process have been identified, and it continues to be an area of ongoing research.

1.1.3 Dormancy

Instead of dying or proliferating into a mass during the colonization process, metastatic cells may have a third possible fate, they may go into a state of dormancy (14). At some later time factors in the microenvironment may trigger their proliferation switch and the cancerous cells may undergo unrestrained growth. However, in all likelihood, the so-called "dormant cells" are actively proliferating but held in check by increased apoptosis and inhibition of angiogenesis. It may remain in this state until the aforementioned equilibrium is disrupted and one or more cells gain the ability of unrestrained growth (26). The exact mechanisms/processes are unknown and this is a very active area of research, important findings in this area will likely lead to a paradigm shift in the treatment of metastatic cancer.

1.1.4 Breast Cancer Metastasis in the Brain

A major concern when dealing with metastatic breast cancer is brain metastases. Of the 22,700 women diagnosed with breast cancer in 2009 (1), 10-16% of these patients developed brain metastases (28-30). The prognosis of the disease is dismal; the one year patient survival is less than 20% upon initial diagnosis (31, 32). The nature of brain metastasis is complex and poorly understood. Brain metastases are generally diagnosed at a late stage of the disease progression (4) and treatment options are limited with varying success. Whole brain irradiation continues to be the standard clinical practice for treating brain metastases but it remains inefficient. It has also been associated with neurocognitive decline and studies have shown that cancer cells in

heterogeneous populations exhibit radio-resistance thus making radiotherapy less effective over time (33, 34).

The pharmaceutical industry has faired no better with treating brain metastases and, in the case of trastuzumab, resulted in an increased incidence of brain metastases (35, 36). Trastuzumab is a monoclonal antibody that has had success with treating systemic metastases below the neck that overexpressed the human epidermal growth factor receptor-2 (HER2) gene (37, 38). Although found in normal cells, its overexpression in metastatic cancer cells has been associated with rapid cell proliferation and an unusually high metastasis to the brain. Prolonged treatment was associated with improvements in patient survival however, it failed to penetrate the blood brain barrier (BBB) (36). The BBB is part of the brain's unique microenvironment and it is composed of non-fenestrated, tightly packed endothelial cells. It excludes the passage of most water-soluble chemotherapeutic agents when given in standard doses, thus allowing the brain to serve as a sanctuary site for micrometastases too small to disrupt the barrier. When a metastatic brain tumor forms it is almost always associated with peritumoral vasogenic edema. The edema is the result of the leakage of protein and other substances across the disrupted BBB within the tumor (4). The substances are not recognized by the normal brain and diffuse from the tumor into the surrounding brain and thus increase the brain water. In addition, when VEGF is produced by the tumor, it may diffuse in the normal brain and increase permeability of normal vessels. Furthermore when metastases are present in the brain, the immune system has difficulty differentiating it from normal tissue. In fact microglial cells, which are the brain's macrophages,

become activated and form a clear boundary between the tumor mass and brain tissue (39). It is quite possible that microglia create an altered brain microenvironment that is more permissive to tumor growth/invasion.

As mentioned earlier, primary tumors are composed of a heterogenous group of cells. When a subset of cells arrives at a distant secondary site, the biological behavior of the developing metastasis may differ significantly from that of the primary tumor. The metastasis itself may contain a heterogenous population of cells and two metastases within the brain may differ from one another (40-42). The heterogeneity of metastases may explain why metastases respond to treatment differently from the primary tumor (42) and it serves as an additional impediment to designing effective cancer therapeutics. It is not uncommon for patients with presumably cured cancer to develop solitary metastases in the brain years later; this is most common amongst breast cancer and melanoma (4).

1.1.5 Modeling Breast Cancer Metastasis to the Brain

The development of model systems is a promising strategy for studying the biology and pathology of brain metastasis and for evaluating potential therapeutic leads. Xenograft model systems of brain metastasis in mice have been developed. Models of breast cancer metastasis to the brain have been described, with preferential metastasis to the brain via hematogenous spread (43-46). Two of the model systems, developed in parallel, used in vivo passage in the mouse to select highly brain metastatic derivative lines of human MDA-MB-231 breast cancer cells. The Price and Yoneda labs performed successive

rounds of culture of isolated experimental brain metastases and re-injection into mice to produce cell lines with enhanced brain metastatic potential (43, 45). From the Yoneda lab, MDA-MB-231 parental breast carcinoma cells were injected into the left cardiac ventricle and isolated brain metastases were resected, recultured and reinjected. After six rounds of selection the brain seeking MDA-MB-231BR (231BR) cell line was established (43), and it metastasized to the brain with 100% frequency and was undetectable in other organs. The 231BR cell line has since served as the foundation for many experimental brain metastasis studies (47-50). Fitzgerald et al. demonstrated that metastases have a much higher propensity to develop in the cortex and hippocampus vs. the olfactory bulb and basal ganglia (47). In the same study they showed that the mouse brain responds to the presence of 231-BR cells with extensive gliosis, where reactive glia are recruited around and within brain metastases, this was observed as early as 14 days post injection. They compared the mouse model findings to clinically resected brain metastases and found similar results regarding microglia recruitment and cell proliferation and apoptosis. Using immunofluorescence they detected proliferative cells and little to no apoptotic cells amongst metastases using the mouse model. There was a similar finding in the clinically resected brain metastases with the exception of apoptotic cells being detected only in areas of necrosis. In another study Palmieri et al. developed the MDA-MB-231BR/HER2 (231BR/HER2) subclone such that the HER2 gene was transfected into 231BR cells. Comparison between the two cell lines revealed no difference in the incidence of metastasis in nude mice but metastases that expressed HER2 in cohort with epidermal growth

factor receptor (EGFR) levels were 3-fold larger in size than metastases of the 231BR lineage (51).

In another study using nude mice, Kim et al. showed that elevated VEGF expression contributed to the ability of breast cancer cells to form brain metastases. Furthermore they showed that targeting endothelial cells with a VEGF-receptor tyrosine kinase inhibitor reduced angiogenesis and restricted the growth of brain metastases (45). In spite of these findings, there was no difference in the periods of survival between mice treated with the VEGF inhibitor and controls. Since the brain is highly vascularized, the necessity of neo-angiogenesis to maintain metastasis survival has been called into question.

Experimental brain metastasis studies using either breast cancer or melanoma have shown that metastases formed along pre-existing blood vessels rather than inducing angiogenesis. Kusters et al. showed that brain metastasis from a melanoma lineage could grow up to 3mm (52) without inducing an angiogenic switch described by Folkman (53), but instead utilized preexisting blood vessels. A similar study even showed that vessel density was in fact lower in areas of metastatic growth in comparison to normal brain regions (54). Both Kim and Kusters show contrary findings regarding the role of angiogenesis in metastasis growth. Furthermore, Ebos et al. showed that while anti angiogenic therapies decreased primary tumor growth they actually increased local invasion and distant metastasis (55). These findings demonstrate a need for further preclinical studies into anti-angiogenic therapies in the context of brain metastasis.

1.1.6 Methods to Study Brain Metastasis

Traditionally, histology has been used to investigate the progression of metastatic cells in the brain when using animal models. This involves tissue fixation, embedding, sectioning, mounting and staining (56). Stains are used to increase the contrast between cells and the organelles within them. When dyes are tagged to antibodies, individual cells of interest can be identified (57). This is very beneficial for investigating metastases with heterogeneous cell populations and for identifying the corresponding changes in the brain microenvironment at the cellular level. Histology offers a detailed look at the events in the metastatic process but only provides a snap shot of one point in time. Since animals have to be sacrificed it is not possible to do in vivo studies that investigate tumor development at multiple timepoints in the same animal. Furthermore, histological studies generally sample partial sections of the mouse brain; thus the information obtained is an estimate of what is occurring throughout the whole brain.

MRI is the gold standard imaging modality to diagnose tumors clinically. It offers the opportunity for high resolution imaging, excellent soft tissue contrast, it is depth independent and can be used to image the whole body or brain. Furthermore MRI has been used to investigate metastatic disease and other pathologies in preclinical animal models (58-60). Downsides to MRI include the long scan times and high cost of operation, but the benefits of MR override its limitations. Cancer and metastasis are pathologies that continue to be an emotional, financial and scientific burden. However, there is tremendous growth in the research and development of MRI and, as result, smaller lesions can be

detected in images, image acquisition is faster and overall treatments are improving.

MRI is based on the relaxation of nuclei in an external magnetic field after being perturbed by a radio frequency (RF) pulse. Different tissues and pathologic lesions have different rates of relaxation; tissue contrast with MRI is achieved by exploiting these differences.

1.2 MRI

1.2.1 The Larmor Frequency

All nuclei with an odd number of protons and/or neutrons possess a non-zero angular momentum, or nuclear spin, s, which results in spin angular momentum S and produces a small magnetic moment μ. The orientation of the magnetic moment is along the spin axis and its magnitude is given by:

$$\mu=\gamma S$$

Equation 1.1: Magnetic Moment

where γ is the gyromagnetic ratio and is specific for every atom. The most abundant atom in the body is hydrogen, which contains one proton and has its own magnetic moment, MR imaging usually consists of imaging protons. Protons in a sample are randomly oriented and this orientation results in a net magnetic moment or magnetization, M_0 of zero since the individual moments cancel each other out (61). If the sample were to be placed in an external magnetic field B_0, then the magnetic moments align with the field, either in the same direction as the magnetic field (parallel) or in the opposite direction (antiparallel). By convention the direction of B_0 is defined to be in the z-direction. A slight excess of protons preferentially orient themselves in the parallel state since it is of lower energy. The resulting net magnetic moment M_0, which is the sum of all of the magnetic moments in the sample, is in the same direction as B_0. The actual

orientation of the protons is slightly tipped away from the B_0 axis (62). The protons experience a torque once the external magnetic field is applied and precess at a frequency known as the Larmor frequency ω_0, where,

$$\omega_0=\gamma B_0.$$

Equation 1.2: Larmour Frequency

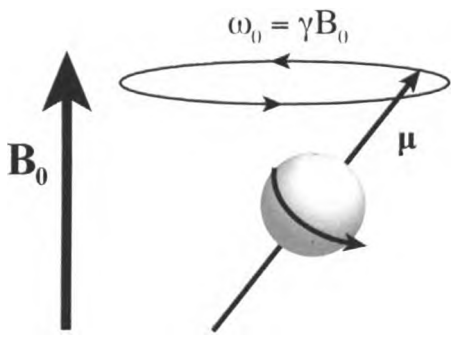

Figure 1.1: Proton Spin experiencing an external magnetic field

When a radiofrequency (RF) pulse is applied to the sample with an external field, at a frequency that matches the Larmor frequency (62) of the protons within the sample, its energy is absorbed by the protons and they are elevated to a higher energy state and develop a spin that is anti parallel to that of the main magnetic field, this causes M_0 to rotate away from the direction of the main field or z-axis (63). This is known as nuclear magnetic resonance (NMR). Once the RF pulse is removed three things occur. First, the magnetization vector continues to precess about the z-axis at the Larmor frequency. The rotating magnetization induces an electromotive force (EMF) in a radiofrequency coil.

The signal measured is known as a free induction decay (FID) curve and is the basic NMR signal that is recorded (63). Second, the magnetization begins to return to its original position along Mz and third, the protons that were precessing in phase with each other begin to dephase. The last two characteristics are known as relaxation effects and are a source of contrast within MR images (64).

To spatially locate the NMR signal, magnetic field gradients are applied in the x, y and z direction which change the local magnetic fields. The way in which these gradients are applied is dependant on the pulse sequence that is being applied. The strength, duration and frequency in which the gradients are applied capture differences in the relaxation times in the sample and create the contrast and signal intensity seen in MR images.

1.2.2 Relaxation

Relaxation effects begin immediately after the RF pulse is turned off, two types of relaxation effects occur: a.) T1 and b.) T2 relaxation. Once the RF pulse is turned off, the absorbed energy is released into the surroundings, or the lattice. T1 relaxation characterizes the return of the net magnetization to its equilibrium state parallel to the z-axis. T2 relaxation is characterized by a loss of phase coherence of the spins in the xy plane. As the net magnetization precesses in the transverse plane each individual spin begins to precess at a different Larmour frequency. As the spins diphase in the transverse plane their signals begin to cancel each other out leading to a loss of net signal. This is caused by two main sources. The first is the energy exchange between molecules through vibrations and/or rotations. This is known as true spin-spin relaxation (T2). The second is

due to magnetic field inhomogeneities (T2') (65). Magnetic field inhomogeneities are caused by variations in the static magnetic field B_0; in the sample the different magnetic susceptibilities change the local magnetic field at tissue boundaries. The total transverse relaxation (T2*) is given by (66):

$$1/T2^* = 1/T2 + 1/T2'$$

Equation 1.3: Components of T2 Relaxation

T1 and T2 relaxation rates vary amongst different tissues in the body. These differences are exploited to generate contrast amongst tissues. The choice of generating primarily T1 or T2 contrast amongst tissues is user dependent and the choice is usually based on the type of tissues to be imaged, the scan time and signal to noise ratio (SNR). This will be further discussed in later sections.

1.2.3 Spatial Encoding

A time varying magnetic field generates a time varying electric field, the resultant electric field results in current in the coil. The coil integrates the signal over the entire volume, at this point there is no way to interpret the received signal and from which tissues in the sample it originated. If we were to interpret the sample as a collection of voxels, where each voxel contributed a finite amount of the total signal received in the coil, we can think of spatial encoding as distinguishing each voxel. The field gradients make the magnetic field vary with position (67), this is done through three different gradients: a.) slice select

gradient, b.) phase encode gradient and c.) frequency encode gradient. As a result of these gradients the signal from each voxel will be encoded with a unique frequency and phase value. The slice of interest is selected by applying an RF pulse in conjunction with a slice select gradient. The frequency of the RF pulse corresponds to the Larmour frequency of the location of interest, which as mentioned before changes linearly in the sample because of the applied gradient. When the RF pulse is applied, only those protons with the Larmour frequency that matches the frequencies of the RF pulse will be tipped into the transverse plane. All frequencies outside the RF bandwidth will not be excited. By defining the bandwidth of the RF pulse to be a certain range of frequencies, the thickness of the slice can also be defined. Decreasing the bandwidth of the RF pulse or increasing the strength of the slice select gradient can produce thinner slices.

1.2.3.1 Phase Encoding

Phase encoding is done after the slice has been selected. The phase encode process can be considered long and tedious since one MR excitation is required for each line of phase encoding data. When the gradient is turned on, the precession of the nuclei appears to speed up or slow down according to their position along the phase encode gradient. When the gradient is removed, the nuclei revert back to their original frequencies but precess at a different phase. The phase of the signal is said to vary in the direction of the gradient (67).

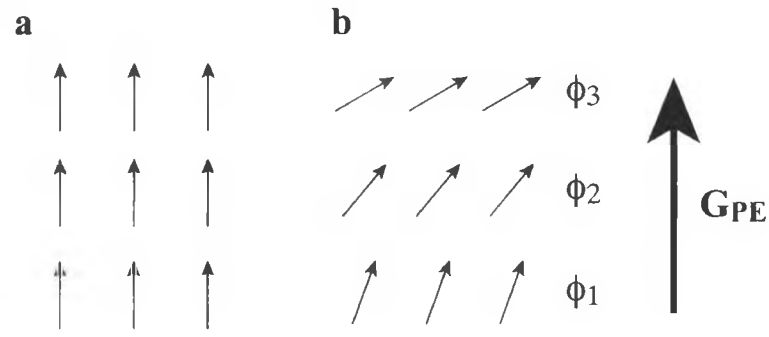

Figure 1.2: Out of Phase spins during phase encoding

1.2.3.2 Frequency Encoding

As the name suggests the application of the frequency encoding gradient causes protons in the sample to spin at different frequencies. The frequency of the signal then varies in the direction of the frequency encode gradient (67). Unlike Spatial encoding, frequency encoding is rapid; all spatial frequency information from one MR signal following one RF excitation can be acquired. It is during this step that the data readout occurs.

1.2.3.3 Fourier Transform

After implementation of the three spatial encoding gradients the resulting signal from each location or voxel has a unique frequency and phase. The time dependant signal can then be processed using a mathematical technique known as the Fourier transformation. The Fourier transform takes a signal in the time domain and decomposes it into its frequency components (67). The MR image can then be reconstructed in the time domain by using an inverse Fourier transform.

1.2.4 MRI Pulse Sequences

1.2.4.1 Spin Echo

MRI pulse sequences manipulate the relaxation effects of nuclei to generate the contrast needed. The spin echo (SE) pulse sequence is one of the most widely used sequences, it consists of one 90° pulse and at least one 180° pulse (67, 63). The 90° pulse tips the magnetization into the transverse plane and then the gradients perform the necessary spatial encoding. However prior to reading out the signal, a 180° pulse is applied and this refocuses the magnetization in the transverse plane to form an echo. The 180° pulse is applied at a time TE/2, where TE is the echo time (63, 67). The contrast produced by SE sequences is dependent on the timing parameters, generally for T1-weighted contrast a short TE and short TR (repetition time between 90° pulses) is required and T2-weighted images require a relatively long TE and TR. A timing diagram of the most simple SE sequences are shown below.

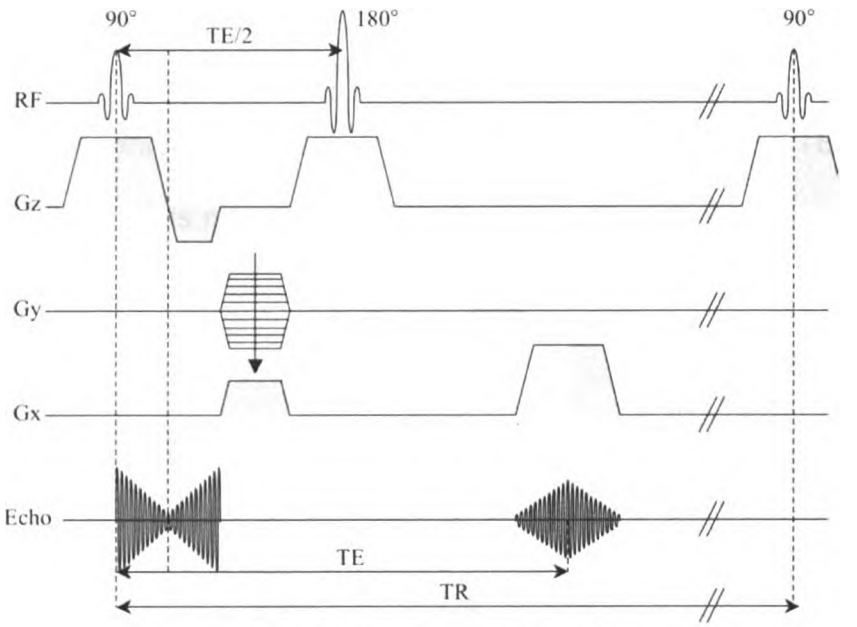

Figure 1.3: Spin Echo Pulse Sequence

1.2.4.2 Gradient Echo

The gradient echo (GE) pulse sequence is the other main branch of pulse sequences most widely used. In GE, speed is enhanced by using a small flip angle (less than 90°) which allows for shorter TRs and essentially shorter scan times than SE pulse sequences. This is possible because a full T1 recovery is not necessary before the next RF excitation. Gradient echo sequences do not correct dephasing of spins due to magnet inhomogeneities and local susceptibility changes are not compensated and thus the time decay of the MR signal is dependant on T2* not T2. This results in smaller signal from GE sequences compared to those from a SE sequence of an identical sample at the same TE. The dephasing and rephasing of the MR signal by the imaging gradients allow for the echo to be formed (63, 67). A slice refocusing gradient is applied after the RF pulse along with the phase and frequency encode gradients.

The frequency encoding gradient is used to completely dephase the magnetization such that the maximum coherence is achieved when the second frequency encoding (readout) gradient is applied. At time TE an echo is formed and the signal is measured. A timing diagram of the most simple GE sequences are shown below.

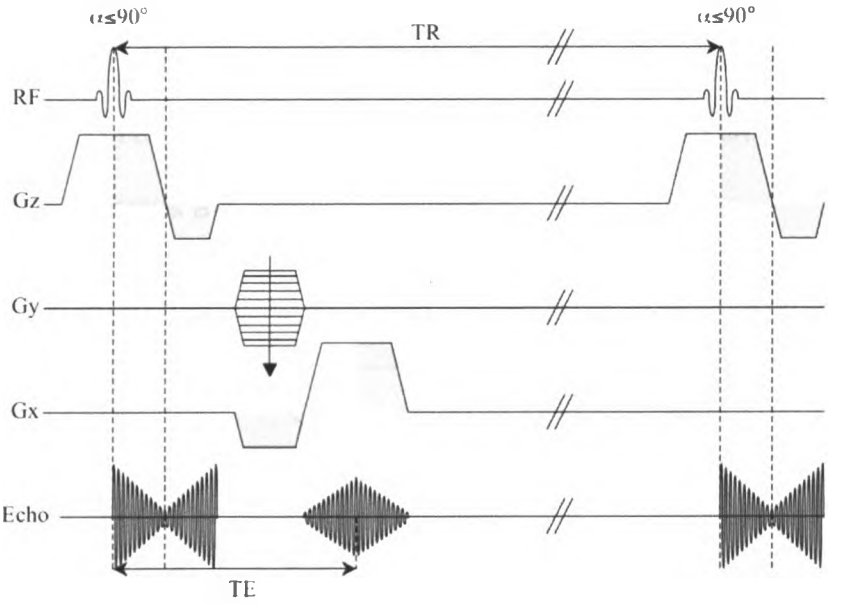

Figure 1.4: Gradient Echo Pulse Sequence

1.2.4.3 Balanced Steady State Free Precession (b-SSFP)

Steady-state free precession (SSFP) is a type of gradient echo sequence that describes the behavior of the net magnetization when the same RF pulse is repeatedly applied to the sample at regular time intervals. An initial RF pulse tips the magnetization an angle $\alpha/2$; a series of alternating $\pm\alpha$ pulses is then applied where the magnetization is tipped an angle of $\alpha/2$ from the z-axis, steady state is

then reached. Reaching steady state is dependant on the size of the α tip and the the tissue being excited. Since there are both longitudinal and transverse components present during the signal acquisition the signal itself is dependant on the T2/T1 ratio (68). Balanced-SSFP sequences also offer the highest signal-to-noise (SNR) ratio per unit time of any pulse sequence.

Three conditions must be met before the steady-state condition can occur. One is that TR<<T2<<T1. This limits the amount of T1 recovery and dephasing effects due to intrinsic T2. The second is that all dephasing effects must be the same between each RF pulse and lastly α and TR must remain constant (69). The timing diagram shows a b-SSFP sequence.

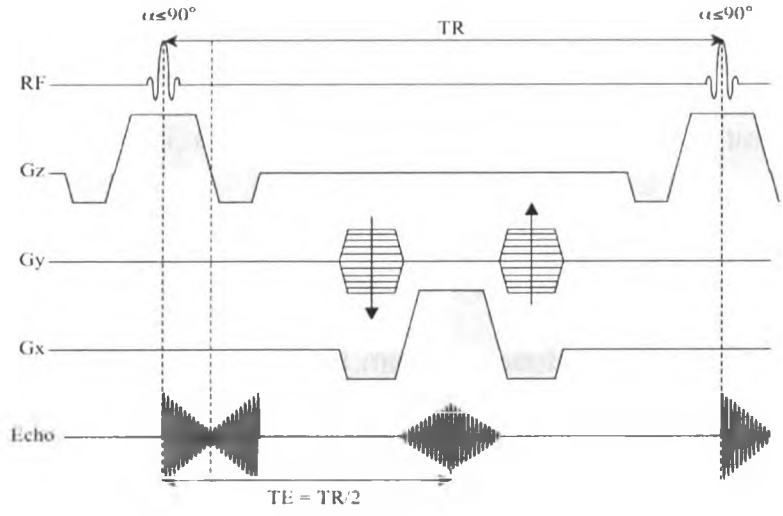

Figure 1.5: b-SSFP Pulse Sequence

In the timing diagram it can be seen that a RF pulse is applied with a tip angle α after which the spatial encoding gradients are applied. After several TR periods (~5T2/TR) the magnetization will be in steady state and data acquisition will begin (69). The b-SSFP sequence is considered balanced because all three

gradients are refocused. SSFP sequences do not refocus the dephasing effects due to the frequency encoding gradient and the net magnetization before the next RF pulse is zero. The net magnetization for b-SSFP at the beginning of the sequence until the next RF pulse is nearly identical with the exception of small T1 and T2 effects occurring during TR (68).

1.2.5 Cancer and MRI

Cancerous tissues have different relaxation rates in comparison to normal tissue, this discovery revealed a property whereby the two tissues could be differentiated with magnetic resonance (70). This property has been exploited with MRI for the diagnosis of glioma tumors in the brain. Using Dynamic Contrast Enhanced (DCE) MRI, Graif et al. showed that when glioma tumors were present the T1 and T2 values were shortened in gray and white matter (71). After the administration of gadolinium-DTPA the T1 values of the glioma decreased between 16%-33% of the original measurements and the MR images displayed high contrast between the tumor and brain parenchyma. Furthermore DCE MRI has the ability to measure fractional blood volume (fbv) and microvascular permeability (k) in brain tumors (72-74). Roberts et al. showed that fbv and k values measured in patients with glioma tumors could be correlated with tumor grade (72).

More recent studies have used DCE T1-w and dynamic susceptibility weighted (DSW) T2-w MRI to estimate cerebral perfusion, cerebral blood volume and blood brain barrier permeability (75-77) when tumors were present in the brain;

perfusion maps could then be created to display these parameters which in turn aid in the diagnosis of brain tumors.

MRI is also the imaging modality of choice in the clinical setting for the diagnosis of brain metastases; it has the ability to detect multiple lesions throughout the whole brain and serves as a preoperative tool to surgery or radiosurgery. Tsutsumi and colleagues were able to identify multiple parenchymal lesions using MRI (78). Following brain metastasis diagnosis the patient received gamma knife radiosurgery to control the lesions; the treatment planning was based on the MRI findings. MRI is also useful for characterizing tumor reoccurrence and tumors with necrotic regions during postoperative follow-up. Hoefnagels et al. used DSW MRI of patients with single or multiple metastases in the brain and the acquired data was used to construct relative cerebral blood volume (rCBV) maps to identify necrosis or predict tumor reoccurrence (74). The findings from the rCBV maps were validated with histology of the resected metastases.

MRI is still far from perfect with regards to detecting brain metastases; Yoo and colleagues were unable to locate brain micrometastases with MRI prior to performing lung surgery, however, post-operative scans had revealed the presence of lung metastases in the brain (79). In spite of this, it should be noted that MRI technology is developing at a rapid rate. Studies have shown that imaging techniques such as arterial spin labeling (ASL) is a good alternative to susceptibility contrast MRI for the diagnosis of brain tumors and metastases, especially when intravenous injection is not possible. Lehmann et al.

demonstrated that all lesions in the brain could be detected using ASL and from the data, informative cerebral blood flow maps could be created (80).

Furthermore high field MRI scanners such as 7T systems are being employed for the detection of brain metastases. Monninghoff and colleagues compared the detection capabilities of brain metastases between a 7T system and 1.5T MR system. They found the 7T system could detect almost as many metastases as the 1.5T and could produce higher spatially resolved images of the brain and was superior at detecting brain hemorrhaging (81).

1.2.6 MRI and Preclinical Studies of Cancer

MRI is widely used in preclinical studies to examine the anatomy of both primary tumors and metastatic lesions and examine their responses to various treatments. It has been used to visualize the growth and development of primary tumors of the breast, liver and brain that have been implanted into experimental mouse and rat models (82-86). Similarly MRI parameters have been optimized to detect single or multiple metastatic lesions in the brain, liver and other secondary organs. MRI has the potential to detect metastases distributed throughout the whole body and to characterize them based on their volume, vasculature and permeability.

Song et al. used MRI to detect brain metastases using a rat model of brain metastatic breast cancer. They found that many of the metastases had formed in cortex regions of the brain as opposed to the olfactory bulb and cerebellum (82). These findings raised new questions as to whether a higher proportion of metastases formed in the cortex because it is a more vascularized

region, whether larger metastases have a higher vascular density and whether or not necrosis occurred. The T2*-w MRI technique employed by this group cannot determine those answers, however, DCE MRI and DWI techniques may provide the answers to those questions since they have the capability to provide both functional and physiological information.

Barck et al. used DWI on mice that had transplanted tumors in the breast. From the data acquired they created apparent diffusion coefficient maps (ADC) and were able to characterize and differentiate regions of necrosis from regions in the tumor with viable cell populations (83). DCE-MRI studies of animal tumor models obtain data that focuses on the washout of Gd-DTPA agents in tumors. The washout kinetics data found in these studies can be correlated with tumor vasculature during post-mortem histological analysis. This is an area of ongoing research but has the potential to be a predictive factor for tumor vascularization.

Similar to the study conducted by Song, Simões and colleagues were able to identify regions in the brain harboring multiple or single brain metastases due to breast cancer using DWI weighted MRI (84). They created ADC maps to differentiate the tumor mass from edema and normal brain tissue and since imaging was done at multiple time points they created growth curves for the developing metastases. The applications of DWI MRI are growing, scientists have used diffusion weighted sodium MRI to image tumor response to a chemotherapeutic agent in rats (87). Advances in this area may eventually be applied to image brain metastases response to treatment.

1.2.7 MRI Contrast Agents

MRI contrast agents shorten the relaxation properties of tissues. All contrast agents shorten both T1 and T2 times of the surrounding tissues, but most contrast agents affect one relaxation time more than the other. Two classes of MRI contrast agents exist: 1.) paramagnetic and 2.) superparamagnetic. Most paramagnetic contrast agents are gadolinium based and are known for mainly shortening the T1 properties of the sample when administered (88). Gadolinium (Gd) has seven unpaired electrons in its electronic structure and consequently has strong paramagnetic properties (89). It is toxic in its elemental state and hence is usually chelated to a ligand, which preserves its paramagnetic properties but can also be cleared by the body through normal renal functions (89). When Gadolinium based contrast agents are administered water protons are exchanged amongst those bound to the Gd agent and the bulk water in the system (88). This in turn speeds up the rate at which nuclei return to a lower energy state after being excited by an RF pulse or the rate of Mz recovery (90). The T1 shortening appears as bright signal on T1 weighted images (89).

Superparamagnetic contrast agents are considered T2-shortening agents. T2-shortening agents are iron oxide based and are usually known by the acronym SPIO (SuperParamagnetic Iron Oxide). When they are placed within a sample the large magnetic moment caused by the external magnetic field induces local magnetic field gradients causing protons in the vicinity of the contrast agent to experience a different frequency than the protons further away from the contrast agent, the contrast agent essentially creates a large inhomogeneity. Like all inhomogeneities it increases the rate of dephasing by

protons and reduces the T2* as well as T1. Pulse sequences that are T2* weighted are used to exploit this phenomenon and the area of the surrounding contrast agent appears as a region of hypointensity or signal loss (91). The part of the SPIO particle that is responsible for producing contrast is the crystallites of iron-oxide that are located in the particle's core. The crystallite consists of magnetite ($Fe_2^{3+}O_3Fe^{2+}O$) and it has its own magnetic domain (91). These magnetic domains are randomly oriented when an external magnetic field is not present but align parallel to the field when it is present.

SPIO particles are classified according to their hydrodynamic diameter, which is the total diameter of the particle (iron-oxide core and the coat). The hydrodynamic diameters of ultra-small SPIO (USPIO, example generic name Combidex®), SPIO (example generic name Feridex®), and micron-sized SPIO (MPIO) are roughly 10-40nm, 80-150nm, and 0.9-8.5μm respectively (92, 93).

1.3 Cellular MRI

1.3.1 Cell Labeling

Contrast agents are the foundation of cellular MRI and are required to allow cells to be detected against the background tissue in MR images. SPIO agents are the most commonly used contrast agents for cellular MRI studies. Their use is attractive to cellular MRI studies for multiple reasons: i.) they are commercially available in a wide range of sizes and surface coatings (93), ii.) they can be biodegradable (93) and iii.) they have greater relaxivity effects in comparison to gadolinium (94, 95).

SPIO agents have been used for both active in vivo cell labeling and for labeling cells in vitro in cell culture. Active labeling employs an intravenous injection of contrast agent that is meant to be taken up by phagocytic cells in the blood, labeling them in-vivo. This type of labeling is especially effective for studying diseases and organs, which involve inflammation and phagocytic immune cells. The immune cells become labeled in-vivo and can migrate to the site of disease, and their hypointense appearance on MR images provides information about their presence and location. This technique has been employed to study animal models of autoimmune encephalomyelitis (EAE), where macrophages in brain lesions were identified (96).

A similar approach has been used to detect metastasis in the lymph nodes and liver. After injection of intravenous USPIO, nodes that normally appeared hyperintense on account of metastasis had developed heterogenous contrast

within the nodes. The dark areas on the MR images were the result of iron uptake by normal node tissue, which contained phagocytic immune cells (97). Kupffer cells are macrophages in the liver and they phagocytose SPIO particles after IV administration. Since tumor tissues lack Kupffer cells, they appear hyperintense in comparison to the hypointense Kupffer cells. Active labeling with SPIO particles has also been used to study macrophage infiltration in stroke (98), arthritis (99) and spinal cord injury (100).

Many cellular MRI studies utilize prelabeling of cells with SPIO for the purposes of cell tracking, cell quantification and injection validation, to name a few. This technique has been applied to visualizing the arrest of metastatic breast cancer cells in the brain (101), tracking the fate of transplanted stem cells (102-105) and pancreatic islets (106-110) and monitoring adoptively transferred dendritic cells in cancer immunotherapy (111-114).

The amount of contrast agent taken up by the cells is dependant on the cell type, contrast agent and the concentration of the contrast agent. Simple incubation can be used for phagocytic cells but is insufficient for labeling non-phagocytotic cells, for example mesenchymal stem cells and HeLa cells do not take up SPIO particles efficiently after 24-48 hours of incubation (115), but rather methods such as electroporation have been utilized to label these cells (116). Other methods of labeling nonphagocytic cells have applied the use of transfection agents such as protamine sulphate and poly-L-lysine which have been shown to increase iron uptake. Iron particles coated with the transfection agent can chaperon the particle into the cell. The transfection agent is incubated with the iron particles and the two undergo an electrostatic interaction; the result

is a negatively charged iron particle that can enter the cell. Iron uptake in mesenchymal stem cells, mouse lymphocytes, rat oligodendrocytes and HeLa cells increased 2-70 times when SPIO particles were coated with PLL compared to an incubation of bare SPIO particles (117). The amount of iron taken up by the cell is one of the most important factors determining the MRI detectability.

1.3.2 MRI Requirements for Cellular Imaging

There are several MRI requirements that are important for detecting iron labeled cells. Most studies use T2-weighted SE or T2*-weighted GE imaging. Dodd et al were the first to show that single iron labeled cells could be imaged (118). This was done in vitro, with T cells labeled with SPIO and suspended in gel, and imaged with GE at 7 Tesla. Dodd and colleagues showed that longer echo times and higher spatial resolution were important factors for detecting cells in gradient echo images. The signal loss created by iron labeled cells is often referred to as the blooming artifact and this artifact is much more pronounced in GE images compared to SE images.

In this thesis the bSSFP imaging sequence is used for iron-labeled cell detection. Heyn et al. demonstrated a linear relationship between the intracellular iron content and the contrast generated by iron labeled cells in bSSFP images at 1.5T. They also showed that bSSFP images have approximately 7x the SNR efficiency of spoiled GE images and that this impacts the ability to detect iron-labeled cells (119,120). Ramadan et al. have shown that (49) an increase in the repetition time and the SNR produce a dramatic increase in the contrast generated by iron-labeled cells in bSSFP images acquired at 3T.

The high resolution and high SNR required for cellular imaging are most often achieved using high field MRI scanners that are dedicated to imaging small animals. High field scanners allow for high SNR when acquiring highly spatially resolved images in a relatively short scan times in comparison to low field scanners. In spite of this high field scanners are associated with poor field homogeneity and longer T1 relaxation times. For this reason, some cellular MRI studies have been conducted on lower field scanners (1.5T and 3.0T) and sometimes with the addition of a custom built insert gradient coil which allows high resolution, fast imaging and effectively converts the clinical MRI system into a micro-imaging system without altering the magnetic field strength (49,101,119,120). High SNR can still be achieved in these systems through the use of custom made RF coils that are designed specifically for the type of animal or animal anatomy that is being imaged and by using highly SNR efficient pulse sequences such as the b-SSFP pulse sequence.

More recently, acquisition protocols have been modified to make cells labeled with USPIO appear hyperintense relative to a dark background, which facilitates detection and localization. Some of the strategies to produce this type of contrast include (1) off resonance pulses to refocus signal from water protons in close proximity of the USPIO (121) and (2) Inversion-recovery with On-resonance water suppression (IRON) (122). One of the disadvantages of these bright contrast techniques is that normal anatomic background of the image is lost and the bright contrast image has to be overlaid with a standard gradient echo or spin-echo anatomical image.

1.3.3 Cellular MRI and Cancer Studies

The development of effective cancer therapies has been hampered in part by the inability to non-invasively track cancer cell progression from the initial cancerous lesion to the formation of a metastatic tumor. Iron oxide based MR contrast agents have enabled clinicians and scientists to identify tumors and metastases with greater efficacy and investigate the spread of cancer cells through hemodynamic and lymphatic pathways.

USPIO have been utilized to identify lymph node metastasis amongst women with breast cancer. After intravenous administration nodes with metastases have heterogeneous contrast within the nodes when imaged with MRI, the dark areas are the result of iron uptake by normal node tissue which contain phagocytic immune cells (97). This method has been applied with great accuracy for diagnosing lymph metastasis. Similarly, a study showed SPIO-enhanced MRI was superior at detecting liver metastases in patients from colorectal cancer vs. CT and gadobenate dimeglumine-enhanced MRI. The SPIO technique detected lesions with 100% accuracy while the other modalities were significantly less (123).

More recently, USPIO particles have been used to image the microvasculature in glioma tumors. Christoforidis and colleagues administered USPIO particles intravenously in rats bearing tumors. The USPIO particles appeared as hypointense regions within the tumor using GE images (124). Post-mortem histological analyses confirmed the USPIO particles had arrived at the tumor vasculature.

Since SPIO particles are non-toxic to cancer cells, it is possible to label cells in culture prior to injection. MRI can then be used to visualize the metastatic progression of cells in vivo at an early stage to the formation of a mass. During progressive cell divisions the label becomes diluted and the MR hypointense signal becomes lost when imaging at later timepoints. This was shown in a study by Heyn et al. where brain metastatic breast cancer cells were labeled with MPIO particles and injected into the left ventricle of the heart in nude mice. MRI was used to image the brain at multiple time points and initially many signal voids were present (101). However at subsequent imaging time points the voids were present in fewer numbers and it is presumed the cells were dividing and the agent was diluted.

More recent studies have focused on using iron oxide contrast agents to visualize changes in the brain microvasculature when brain metastases are being treated with anti-angiogenic drugs. JuanYin and colleagues administered Cediranib, an anti-VEGF receptor drug to a treatment mouse group that had brain metastases; they injected mice with USPIO particles intravenously to monitor changes in the brain microenvironment (125). Initially, brain metastatic breast cancer cells were labeled with MPIO prior to injection and imaged with MRI on day 3 postinjection; this technique enabled them to verify the success of their injections. T2* imaging of mice injected with USPIO indicated a higher cerebral blood volume within metastases and their surrounding area. It also indicated the drug was effective at inhibiting angiogenesis since USPIO infiltration was lower amongst metastases in the treated group.

1.3.4 Targeted Imaging of Cancer

Targeted MRI makes use of a special class of imaging probes that are conjugated to specific antibodies or proteins that are overexpressed on cell surfaces. Amino acids, such as glutamine, are required for cell proliferation, which makes it ideal for the engineering of a targeted contrast agent. Gadolinium chelates conjugated to glutamate residues have been developed as targeted MR contrast agent for cancer. After intravenous injection of the contrast agent, tumors from neuroblastoma cells in normal mice and in Her2/neu transgenic mice which developed mammary carcinomas, could be visualized (126). A similar approach has been applied to CD20 which is a protein expressed on mature B-cells, lymphoma cells and melanoma cells. USPIO conjugated to anti-CD20 antibody was shown to target lymphoma cells injected into nude mice resulting in a decrease in signal within the tumor (127).

In order for targeting agents to be effective at targeting various cells, the target cell must overexpress the molecule or receptor of interest and the receptor must also be internalized and recycled quickly in order to maximize uptake of the agent.

1.3.5 Limitations of Cellular MRI for Preclinical Studies of Cancer

The major advantage of the application of cellular MRI to cancer is the ability to visualize cells on high resolution MR images with excellent soft tissue contrast. In spite of this, cellular MRI is still a developing field and there are several caveats. Sufficient contrast can only be achieved by the availability of

high affinity contrast agents at the target area and this requires overcoming biological delivery barriers such as cell membranes, and the blood brain barrier in the case of visualizing brain metastatic cancer cells.

Prelabeling cancer cells with iron, for preclinical investigations, is a way around this obstacle but the agent becomes diluted during subsequent cell divisions and cell contrast is generally limited to early time points. In spite of this, studies have indicated that single cells could still be visualized in vivo as late as 7 weeks after injection when labeled with iron (128).

Another potential limitation of the use of iron for labeling cells is that dead labeled cells or iron particles released by dead/dying cells could be taken up by bystander cells (such as macrophages) and the signal loss could be misinterpreted as the original labeled cell. Pawelczyk and colleagues (129) used a Boyden Chamber model of inflammation to examine the frequency of transfer of iron from labeled bone mesenchymal stem cells or cancer cells to activated macrophages. Fluorescence activated cell sorting and fluorescence microscopy revealed that only 5-15% of the iron label was taken up by the macrophages. Their results advise caution when tracking iron-labeled cells for long periods of time but also suggest that the amount of transfer from dead cells to bystander cells is below the MRI detection level for transplants of 2 million iron-labeled cells or less.

These claims are valid and highlight the need for histological or immunohistochemical validation after the final MRI experiment when tracking a metastatic cell population. Many metastatic cell populations are transfected with plasmids that overexpress green fluorescent protein+ (GFP+). This allows for

correlations between metastatic cell populations as perceived on MR images with metastatic cell population as determined by histology.

Although iron based contrast agents are generally perceived to be non toxic, when used in high concentrations for in vivo studies it has been known to interact with a number of metabolic pathways that may induce oxidative stress (130, 131).

1.4 Project Overview

Brain metastases are among the most feared and debilitating complication of systemic cancer. Historically they affect approximately 10-16% of patients diagnosed with metastatic breast cancer and the one-year patient survival is less than 20% upon initial diagnosis (28-30). The development of brain metastasis models offers the hope of further understanding the nature of brain metastatic breast cancer cells and their interaction with the brain microenvironment. Histology is the main tool used to investigate brain metastasis in animal models and many of the findings have been promising. A drawback of histology is its inability to examine metastasis throughout the whole brain; also, the time point of the study is limited to the endpoint. Previous studies have shown that MRI can detect metastatic breast cancer cells in vivo in the brain of mice when labeled with MPIO particles. The whole brain can be visualized and the development of metastases can be studied non-invasively at multiple time points.

In 1889, British physician Stephen Paget proposed the "seed and soil" hypothesis to explain the formation of metastasis. He postulated, "the distribution of the secondary growth is not a matter of chance...when a plant goes to seed, its seeds are carried in all directions; but they can only live and grow if they fall on congenial soil (15)." That is to say, the tumor cell (seed) can only flourish if it encounters a hospitable organ (soil). Other studies have contended that the metastatic disease is the product of hemodynamic factors (41).

Based on histological findings by Palmieri et al (46). and Fitzgerald et al (47). we hypothesized that metastasis to the brain will conform to a pattern, where, some brain regions would be more predisposed to its formation than others. Also, it was our goal to develop a technique to determine tumor growth rates when using a brain metastatic mouse model of breast cancer. MRI was used to compare the metastatic potential of two highly brain metastatic human breast cancer cell lines in mice: (1) MDA-MB-231BR and (2) MDA-MB-231BR/HER2; this involved investigating the incidence of metastases formation in different regions of the brain and comparing the tumor volumes at different time points, the latter allowed us to examine and compare the growth rates of the metastases in mice between the two cell lines. Furthermore, we examined the effect of varying the concentration of breast cancer cells delivered intravenously had on tumor size. Also, we performed an MRI scan on day 1 post injection to examine the distribution of voids in different regions of the brain and correlated the finding with the subsequent distribution of metastases at the endpoint of the study. This study is described in Chapter 2 and is to be submitted as a manuscript for publication. In Chapter 3 the findings of this study are reviewed and related it to the work of others in the field of investigating brain metastasis.

1.5 REFERENCES

1. Canadian Cancer Statistics 2010. Canadian Cancer Society. www.cancer.ca

2. Gupta GP, Massague J, Cancer metastasis: Building a framework. Cell. 2006 Nov 17; 127(4): 679-95

3. Nathoo N, Chahlavi A, Barnett GH. Pathobiology of brain metastases. J Clin Pathol 2005; 58(3):237-242

4. Raizer JJ, Abrey LE "Brain Metastases". Springer 2007

5. Cavallaro U, Christofori G: Cell adhesion in tumor invasion and metastasis; loss of the glue is not enough. Biochim Biophs Acta Rev Cancer 2001; 1552(1):39-45

6. Steeg PS: Tumor metastasis: mechanistic insights and clinical challenges. Nat Med 2006; 12(8):895-904

7. Wyckoff JB, Jones JG, Condeelis JS. A critical step in metastasis: *In vivo* analysis of intravasation at the primary tumor. Cancer Research 2000;60(9):2504-2511

8. Hanna N: Inhibition of experimental tumor metastasis by selective activation of natural killer cells. Cancer Res 1982; 42(4): 1337-1342.

9. Borsig L, Wong R, Hynes RO. Synergistic effects of L- and P-selectin in facilitating tumor metastasis can involve non-mucin ligands and implicate leukocytes as enhancers of metastasis. Proc Natl Acad Sci U S A 2002;99(4):2193-2198

10. Pasqualini R, Arap W: Profiling the molecular diversity of blood vessels. Cold Spring Harb Symp Quant Biol 2002; 67:223-225.

11. Trepel M, Arap W, Pasqualini R: In vivo phage display and vascular heterogeneity: implications for targeted medicine. Curr Opin Chem Biol 2002; 6(3):399-404.

12. Brayton J, Qing Z, Hart MN. Influence of adhesion molecule expression by human brain microvessel endothelium on cancer cell adhesion. J Neuroimmunol 1998; 89(1-2):104-112.

13. Puduvalli VK: Brain metastases: biology and the role of the brain microenvironment Curr Oncol Rep 2001; 3(6):467-475.

14. Hedley BD, Allan AL, Chambers AF: Tumor dormancy and the role of metastasis suppressor genes in regulating ectopic growth. Future Oncol 2006;2(5):627-641.

15. Paget S. The distribution of secondary growths in cancer of the breast. The Lancet. 1889;1:99-101.

16. Poste G, Doll J, Hart IR, Fidler IJ. In vitro selection of murine B16 melanoma variants with enhanced tissue-invasive properties. Cancer Res. 1980 May;40(5):1636-44.

17. Hart IR, Fidler IJ. Role of organ selectivity in the determination of metastatic patterns of B16 melanoma. Cancer research. 1980;40:2281-7

18. De la Monte SM, Moore GW, Hutchins GM. Nonrandom distribution of metastases in neuroblastic tumors. Cancer. 1983 Sept 1;52(5):915-25

19. Saitoh H, Yoshida K, Uchijima Y, Kobayashi N, Suwata J, Kamata S. Two different lymph node metastatic patterns of prostate cancer. Cancer. 1990 Apr 15;65(8):1843-6.

20. Rose PG, Piver MS, Tsukada Y, Lau TS. Metastatic patterns in histologic variants of ovarian cancer. An autopsy study. Cancer. 1989 Oct 1;64(7):1508-13.

21. Weiss L. Comments on hematogenous metastatic patterns in humans as revealed by autopsy. Clin Exp Metastasis. 1992 May; 10(3): 191-9.

22. Chambers AF, Groom AC, MacDonald IC, Dissemination and growth of cancer cells in metastatic sites. Nat Rev Cancer. 2002 Aug;2(8):563-72.

23. Luzzi KJ, MacDonald IC, Schmidt EE. Multistep nature of metastatic inefficiency – Dormancy of solitary cells after successful extravasation and limited survival of early micrometastases. Am J Pathol 1998; 153(3):865-873.

24. Folkman J: Tumor angiogenesis: therapeutic implications. N Engl J Med 1971;285(21): 1182-1186.

25. Folkman J: How is blood vessel growth regulated in normal and neoplastic tissue? G.H.A. Clower Memorial Award Lecture. Cancer Res 1986; 46:467-473.

26. Kirsch M, Schackert G, Blkack PM: Angiogenesis, metastasis, and endogenous inhibition. J Neuro-Oncol 2000; 50(1-2):173-180.

27. Folkman J, Klagsbrun M: Angiogenic factors. Science 1987; 235(4787):442-447.

28. Weil RJ, Palmieri DC, Bronder JL, Stark AM, Steeg PS. Breast cancer metastasis to the central nervous system. Am J Pathol 2005;167(4):913-20.

29. Lin NU, Bellon JR, Winer EP. CNS metastases in breast cancer. J Clin Oncol 2004;22(17):3608-17.

30. DiStefano A, Yong Yap Y, Hortobagyi GN, Blumenschein GR. The natural history of breast cancer patients with brain metastases. Cancer 1979;44(5):1913-8.

31. Weil RJ, Palmieri DC, Bronder JL, Stark AM, Steeg PS. Breast cancer metastasis to the central nervous system. Am J Pathol 2005;167(4):913-20.

32. Harputluoglu H, Dizdar O, Aksoy S. Characteristics of breast cancer patients with central nervous system metastases: A single-center experience. J Natl Med Assoc 2008;100(5):521-6.

33. Lee K, Kang JE, Lee JJ, Won M. LW6, a novel HIF-1 inhibitor, promotes proteasomal degradation of HIF-1 alpha via up-regulation of VHL in a colon cancer line. Biochem Pharmacol. 2010; 52(5):915-25

34. Li Z, Rich JN. Hypoxia and Hypoxia Inducible Factors in Cancer Stem Cell Maintenance. Curr Top Microbiol Immuno. 2010.

35. Stemmler HJ, Kahlert S, Siekiera W, Untch M, Heinrich B, Heinemann V. Characteristics of patients with brain metastases receiving trastuzumab for HER2 overexpressing metastatic breast cancer. Breast 2006;15(2):219-25.

36. Baculi RH, Suki S, Nisbett J, Leeds N, Groves M. Meningeal carcinomatosis from breast carcinoma responsive to trastuzumab. J Clin Oncol 2001;19(13):3297-8.

37. Smith I, Procter M, Gelber RD. 2-year follow-up of trastuzumab after adjuvant chemotherapy in HER2-positive breast cancer: A randomised controlled trial. Lancet 2007;369(9555):29-36.

38. Marty M, Cognetti F, Maraninchi D. Randomized phase II trial of the efficacy and safety of trastuzumab combined with docetaxel in patients with human epidermal growth factor receptor 2-positive metastatic breast cancer administered as first-line treatment: The M77001 study group. J Clin Oncol 2005;23(19):4265-74.

39. He BP, Wang JJ , Zhang X. Differential reactions of microglia to brain metastasis of lung cancer. Mol Med 2006; 12(7-8):161-170.

40. Goodison S, Kawai K, Hihara J. Prolonged dormancy and site-specific growth potential of cancer cells spontaneously disseminated from nonmetastatic breast tumors as revealed by labeling with green fluorescent protein. Clin Cancer Res 2003;9:3808–14.

41. Chambers AF, Groom AC, MacDonald IC. Dissemination and growth of cancer cells in metastatic sites. Nat Rev Cancer 2002;2:563–72.

42. Naumov GN, Townson JL, MacDonald IC. Ineffectiveness of doxorubicin treatment on solitary dormant mammary carcinoma cells or late-developing metastases. Breast Cancer Res Treat 2003;82:199–206.

43. Yoneda T, Williams PJ, Hiraga T, Niewolna M, Nishimura R. A bone-seeking clone exhibits different biological properties from the MDA-MB-231 parental human breast cancer cells and a brain-seeking clone in vivo and in vitro. J Bone Miner Res 2001;16(8):1486-95.

44. Chen EI, Hewel J, Krueger JS, Adaptation of energy metabolism in breast cancer brain metastases. Cancer Res 2007;67(4):1472-86.

45. Kim LS, Huang S, Lu W, Lev DC, Price JE. Vascular endothelial growth factor expression promotes the growth of breast cancer brain metastases in nude mice. Clin Exp Metastasis 2004;21(2):107-18.

46. Palmieri D, Lockman PR, Thomas FC. Vorinostat inhibits brain metastatic colonization in a model of triple-negative breast cancer and induces DNA double-strand breaks. Clin Cancer Res 2009;15(19):6148-57.

47. Fitzgerald DP, Palmieri D, Hua E. Reactive glia are recruited by highly proliferative brain metastases of breast cancer and promote tumor cell colonization. Clin Exp Metastasis 2008;25(7):799-810.

48. Song HT, Jordan EK, Lewis BK. Rat model of metastatic breast cancer monitored by MRI at 3 tesla and bioluminescence imaging with histological correlation. J Transl Med 2009;7:88

49. Ramadan SS, Heyn C, Mackenzie LT, Chambers AF, Rutt BK, Foster PJ. Ex-vivo cellular MRI with b-SSFP: Quantitative benefits of 3T over 1.5 T. MAGMA 2008;21(4):251-9.

50. Thomas FC, Taskar K, Rudraraju V. Uptake of ANG1005, a novel paclitaxel derivative, through the blood-brain barrier into brain and experimental brain metastases of breast cancer. Pharm Res 2009;26(11):2486-94.

51. Palmieri D, Bronder JL, Herring JM. Her-2 overexpression increases the metastatic outgrowth of breast cancer cells in the brain. Cancer Res 2007;67(9):4190-8.

52. Kusters B, Leenders WP, Wesseling P. Vascular endothelial growth factor-A(165) induces progression of melanoma brain metastases without induction of sprouting angiogenesis. Cancer Res 2002;62(2):341–5.

53. Folkman J. What is the evidence that tumors are angiogenesis-dependent? J Natl Cancer Inst 1990;82:4–6.

54. Carbonell WS, Ansorge O, Sibson N, Muschel R. The vascular basement membrane as "soil" in brain metastasis. PLoS One 2009;4(6):e5857.

55. Ebos JM, Lee CR, Cruz-Munoz W, Bjarnason GA, Christensen JG, Kerbel RS. Accelerated metastasis after short-term treatment with a potent inhibitor of tumor angiogenesis. Cancer Cell 2009;15(3):232–9.

56. Presnell JK, Schreibman MP, Humason GL. Humason's animal tissue techniques. 5th ed. Baltimore: John Hopkins University Press; 1997.

57. Bergman RA, Afifi AK, Heidger PM. Histology. Philadelphia: Saunders; 1996.

58. Jensen LR, Huuse EM, Bathen TF. Assessment of early docetaxel response in an experimental model of human breast cancer using DCE-MRI, ex vivo HR MAS, and in vivo 1H MRS. NMR Biomed 2010;23(1):56-65.

59. Black PC, Shetty A, Brown GA. Validating bladder cancer xenograft bioluminescence with magnetic resonance imaging: The significance of hypoxia and necrosis. BJU Int 2010.

60. Wu X, Feng Y, Jeong EK, Emerson L, Lu ZR. Tumor characterization with dynamic contrast enhanced magnetic resonance imaging and biodegradable macromolecular contrast agents in mice. Pharm Res 2009;26(9):2202-8.

61. Pykett IL, Newhouse JH, Buonanno FS, Brady TJ, Goldman MR, Kistler JP, et al. Principles of nuclear magnetic resonance imaging. Radiology. 1982 Apr;143(1):157-68.

62. Haacke EM. Magnetic resonance imaging: Physical principles and sequence design. New York: J. Wiley-Liss; 1999.

63. Nishimura DG. Principles of magnetic resonance imaging. United States of America: Dwight G. Nishimura; 1996.

64. Brown MA, Semelka RC. MRI: Basic principles and applications. 1st ed. United States of America: Wiley-Liss Inc.; 1995.

65. Smith RC, Lange RC. Understanding magnetic resonance imaging. USA: CRC Press; 1997.

66. Ma J, Wehrli FW. Method for image-based measurement of the reversible and irreversible contribution to the transverse-relaxation rate. J Magn Reson B.; 1996.

67. McRobbie DW, Moore EA, Graves MJ, Prince MR. MRI from Picture to Proton, Cambridge University Press, Cambridge, 2008.

68. Scheffler K, Lehnhardt S. Principles and applications of balanced SSFP techniques. Eur Radiol. 2003 Nov; 13(11):2409-18.

69. Scheffler K. A pictorial description of steady-states in rapid magnetic resonance imaging. Concepts Magn Reson. 1999;11(5):291-304.

70. Wallis F, Gilbert FJ. Magnetic resonance imaging in oncology: An overview. J R Coll Surg Edinb. 1999 Apr;44(2):117-25.

71. Graif M, Bydder GM, Steiner RE, Niendorf P, Thomas DG, Young IR. Contrast-enhanced MR imaging of malignant brain tumors. AJNR Am J Neuroradiol 1985;6(6):855-62.

72. Roberts HC, Roberts TP, Bollen AW, Ley S, Brasch RC, Dillon WP. Correlation of microvascular permeability derived from dynamic contrast-enhanced MR imaging with histologic grade and tumor labeling index: A study in human brain tumors. Acad Radiol 2001;8(5):384-91.

73. Roberts HC, Roberts TP, Brasch RC, Dillon WP. Quantitative measurement of microvascular permeability in human brain tumors achieved using dynamic contrast-enhanced MR imaging: Correlation with histologic grade. AJNR Am J Neuroradiol 2000;21(5):891-9.

74. Hoefnagels FW, Lagerwaard FJ, Sanchez E, et al. Radiological progression of cerebral metastases after radiosurgery: Assessment of perfusion MRI for differentiating between necrosis and recurrence. J Neurol 2009;256(6):878-87.

75. Galie M, Farace P, Merigo F, et al. Washout of small molecular contrast agent in carcinoma-derived experimental tumors. Microvasc Res 2009;78(3):370-8.

76. Jensen LR, Huuse EM, Bathen TF, et al. Assessment of early docetaxel response in an experimental model of human breast cancer using DCE-MRI, ex vivo HR MAS, and in vivo 1H MRS. NMR Biomed 2010;23(1):56-65.

77. Larsson HB, Courivaud F, Rostrup E, Hansen AE. Measurement of brain perfusion, blood volume, and blood-brain barrier permeability, using dynamic contrast-enhanced T(1)-weighted MRI at 3 tesla. Magn Reson Med 2009;62(5):1270-81.

78. Tsutsumi S, Yasumoto Y, Oizumi H, Ito M. Chondrosarcoma with atypical clinical presentation treated by gamma knife radiosurgery for multiple brain metastases--case report. Neurol Med Chir (Tokyo) 2010;50(6):502-5.

79. Yoo H, Jung E, Nam BH, et al. Growth rate of newly developed metastatic brain tumors after thoracotomy in patients with non-small cell lung cancer. Lung Cancer 2010.

80. Lehmann P, Monet P, de Marco G. A comparative study of perfusion measurement in brain tumours at 3 tesla MR: Arterial spin labeling versus dynamic susceptibility contrast-enhanced MRI. Eur Neurol 2010;64(1):21-6.

81. Monninghoff C, Maderwald S, Theysohn JM, et al. Imaging of brain metastases of bronchial carcinomas with 7 T MRI - initial results. Rofo 2010.

82. Song HT, Jordan EK, Lewis BK, et al. Rat model of metastatic breast cancer monitored by MRI at 3 tesla and bioluminescence imaging with histological correlation. J Transl Med 2009;7:88

83. Barck KH, Willis B, Ross J, French DM, Filvaroff EH, Carano RA. Viable tumor tissue detection in murine metastatic breast cancer by whole-body MRI and multispectral analysis. Magn Reson Med 2009;62(6):1423-30.

84. Simoes RV, Martinez-Aranda A, Martin B, Cerdan S, Sierra A, Arus C. Preliminary characterization of an experimental breast cancer cells brain metastasis mouse model by MRI/MRS. MAGMA 2008.

85. Wu X, Feng Y, Jeong EK, Emerson L, Lu ZR. Tumor characterization with dynamic contrast enhanced magnetic resonance imaging and biodegradable macromolecular contrast agents in mice. Pharm Res 2009;26(9):2202-8.

86. Wu X, Jeong EK, Emerson L, Hoffman J, Parker DL, Lu ZR. Noninvasive evaluation of antiangiogenic effect in a mouse tumor model by DCE-MRI with gd-DTPA cystamine copolymers. Mol Pharm 2010;7(1):41-8.

87. Schepkin VD, Lee KC, Kuszpit K, Rehemtulla A, Ross BD. Proton and sodium MRI assessment of emerging tumor chemotherapeutic resistance. NMR Biomed. 2006; 19: 1035-42.

88. Caravan P. Strategies for increasing the sensitivity of gadolinium based MRI contrast agents. Chem Soc Rev. 2006;35:512-23.

89. Caravan P, Ellison JJ, McMurry TJ, Lauffer RB. Gadolinium (III) chelates as MRI contrast agents: Structure, dynamics, and applications. Chem Rev. 1999 Sep 8;99(9):2293-352.

90. Brown MA, Semelka RC. MRI: Basic principles and applications. 1st ed. United States of America: Wiley-Liss Inc.; 1995.

91. Corot C, Robert P, Idee JM, Port M. Recent advances in iron oxide nanocrystal technology for medical imaging. Adv Drug Deliv Rev. 2006 Dec 1;58(14):1471-504.

92. Modo MMJJ. Molecular and cellular MR imaging. Hoboken: CRC Press; 2007.

93. Shapiro EM, Skrtic S, Koretsky AP. Sizing it up: Cellular MRI using micron–sized iron oxide particles. Magn Reson Med. 2005 Feb;53(2):329-38.

94. Brekke, C. Cellular multiparametric MRI of neural stem cell therapy in a rat glioma model. Neuroimage, 2007. 37(3): p. 769-82.

95. Modo, M. Tracking transplanted stem cell migration using bifunctional, contrast agent-enhanced, magnetic resonance imaging. Neuroimage, 2002. 17(2): p. 803-11.

96. Oweida AJ, Dunn EA, Foster PJ. Cellular imaging at 1.5T: Detecting cells in neuroinflammation using active labeling with superparamagnetic iron oxide. Mol Imaging. 2004 Apr;3(2):85-95.

97. Weissleder R, Elizondo G, Wittenberg J, Lee AS, Josephsen L, Brady TJ. Ultrasmall superparamagnetic iron oixde: An intravenous contrast agent for assessing lymph nodes with MR imaging. Radiology. 1990 May;175(2):494-8.

98. Schroeter M, Jander S, Huitinga I, Witte OW, Stoll G. Phagocytic response in photochemically induced infarction of rat cerebral cortex. The role of resident microglia. Stroke. 1997 Feb;28(2):382-6.

99. Dardzinski BJ, Schmithorst VJ, Holland SK, Boivin GP, Imagawa T, Watanabe S, et al. MR imaging of murine arthritis using ultrasmall superparamagnetic iron oxide particles. Magn Reson Imaging. 2001 Nov;19(9):1209-16.

100. Dunn EA, Weaver LC, Dekaban GA, Foster PJ. Cellular imaging of inflammation after experimental spinal cord injury. Mol Imaging. 2005 Jan-Mar;4(1):53-62.

101. Heyn C, Ronald JA, Ramadan SS. In vivo MRI of cancer cell fate at the single-cell level in a mouse model of breast cancer metastasis to the brain. Magn Reson Med 2006;56(5):1001-10.

102. Yao Y, Li Y, Ma G. In vivo magnetic resonance imaging of injected endothelial progenitor cells after myocardial infarction in rats. Mol Imaging Biol 2010.

103. Henning TD, Boddington S, Daldrup-Link HE. Labeling hESCs and hMSCs with iron oxide nanoparticles for non-invasive in vivo tracking with MR imaging. J Vis Exp. 2008 Mar 31;(13). pii: 685. doi: 10.3791/685.

104. Sykova E, Jendelova P. In vivo tracking of stem cells in brain and spinal cord injury. Prog Brain Res. 2007;161:367-83.

105. Lee IH, Bulte JW, Schweinhardt P, Douglas T, Trifunovski A, Hofstetter C, Olson L, Spenger C. In vivo magnetic resonance tracking of olfactory ensheathing glia grafted into the rat spinal cord. *Exp Neurol.* 187: 509-516 (2004).

106. Evgenov NV, Medarova Z, Pratt J, Pantazopoulos P, Leyting S, Bonner-Weir S, Moore A. In vivo imaging of immune rejection in transplanted pancreatic islets. Diabetes. 2006 Sep;55(9):2419-28.

107. Berkova Z, Jirak D, Zacharovova K, Kriz J, Lodererova A, Girman P, Koblas T, Dovolilova E, Vancova M, Hajek M, Saudek F. Labeling of pancreatic islets with iron oxide nanoparticles for in vivo detection with magnetic resonance. Transplantation. 2008 Jan 15;85(1):155-9.

108. Tai JH, Foster P, Rosales A, Feng B, Hasilo C, Martinez V, Ramadan S, Snir J, Melling CW, Dhanvantari S, Rutt B, White DJ. Imaging islets labeled with magnetic nanoparticles at 1.5 Tesla. Diabetes. 2006 Nov;55(11):2931-8.

109. Jirak D, Kriz J, Strzelecki M, Yang J, Hasilo C, White DJ, Foster PJ. Monitoring the survival of islet transplants by MRI using a novel technique for their automated detection and quantification. MAGMA. 2009 Aug;22(4):257-65.

110. Kriz J, Jirak D, White D, Foster P. Magnetic resonance imaging of pancreatic islets transplanted into the right liver lobes of diabetic mice. Transplant Proc. 2008 Mar;40(2):444-8.

111. Dekaban GA, Snir J, Shrum B, de Chickera S, Willert C, Merrill M, Said EA, Sekaly RP, Foster PJ, O'connell PJ. Semiquantitation of Mouse Dendritic Cell Migration In Vivo Using Cellular MRI. J Immunother. 2009 Apr;32(3):240-51.

112. Ahrens ET, Feili-Hariri M, Xu H, Genove G, and Morel PA. Receptor-mediated endocytosis of iron-oxide particles provides efficient labeling of dendritic cells for in vivo MR imaging. *Magn Reson Med. 2003;* **49:** 1006-1013.

113. Long CM, van Laarhoven HW, Bulte JW, Levitsky HI. Magnetovaccination as a novel method to assess and quantify dendritic cell tumor antigen capture and delivery to lymph nodes. Cancer Res. 2009 Apr 1;69(7):3180-7.

114. Rohani R, de Chickera S, Willert C, Chen Y, Dekaban GA, Foster PJ. In vivo cellular MRI of dendritic cell migration using MPIO particles. Mol Imaging Bio in press.

115. Frank JA, Miller BR, Arbab AS, Zywicke HA, Jordan EK, Lewis BK. Clinically applicable labeling of mammalian and stem cells by combining superparamagnetic iron oxides and transfection agents. Radiology. 2003 Aug;228(2):480-7

116. Suzuki Y, Zhang S, Kundu P, Yeung AC, Robbins RC, Yang PC. In vitro comparison of the biological effects of three transfection methods for magnetically labeling mouse embryonic stem cells with ferumoxides. Magn Reson Med. 2007 Jun;57(6):1173-9.

117. Frank JA, Anderson SA, Kalsih H, Jordan EK, Lewis BK, Yocum GT. Methods for magnetically labeling stem and other cells for detection by in-vivo magnetic resonance imaging. Cytotherapy. 2004;6(6):621-5.

118. Dodd SJ, Williams M, Suhan JP, Williams DS, Koretsky AP, Ho C. Detection of single mammalian cells by high-resolution magnetic resonance imaging. Biophys J. 1999 Jan;76(1 Pt 1):103-9.

119. Heyn C, Bowen CV, Rutt BK and Foster PJ. Detection threshold of single SPIO-labeled cells with FIESTA. Magn Reson Med 2005 53: 312-320.

120. Heyn C, Ronald JA, Mackenzie LT, MacDonald IC, Chambers AF, Rutt BK, and Foster PJ. In vivo magnetic resonance imaging of single cells in mouse brain with optical validation. Magn Reson Med. 2006; 55: 23-29.

121. Cunningham CH, Arai T, Yang PC, Conolly SM. Positive contrast magnetic resonance imaging of cells labeled with magnetic nanoparticles. Magn. Reson. Med. 53 (2005) 999-1005.

122. Stuber M, Gilson WD, Schar M, Kedziorek DA, Hofmann LV, Bulte JWM, Kraitchman DL. Positive contrast visualization of iron oxide-labeled stem cells using inversion-recovery with ON-resonant water suppression (IRON).

123. Hekimoglu K, Ustundag Y, Dusak A. Small colorectal liver metastases: Detection with SPIO-enhanced MRI in comparison with gadobenate dimeglumine-enhanced MRI and CT imaging. Eur J Radiol 2009.

124. Christoforidis GA, Yang M, Kontzialis MS, Larson DG, Barth RF. High resolution ultra high field resonance imaging of glioma microvascularity and hypoxia using ultra-small particles of iron oxide. Invest Radiol. 2009 Jul;44(7):375-83.

125. JuanYin J, Tracy K, Zhang L. Noninvasive imaging of the functional effects of anti-VEGF therapy on tumor cell extravasation and regional blood volume in an experimental brain metastasis model. Clin Exp Metastasis 2009;26(5):403-1

126. Geninatti Crich S, Cabella C, Barge A, Belfiore S, Ghirelli C, Lattuada L. In vitro and in-vivo magnetic resonance detection fo tumor cells by targeting glutamine transporters with gd-based probes. J Med Chem. 2006 Aug 10;49(16):4926-36.

127. Baio G, Fabbi M, det Totero D, Ferrini S, Cilli M, Derchi LE. Magnetic resonance imaging at 1.5T with immunospecific contrast agent in vitro and in-vivo in a xenotransplant model. MAGMA. 2006 Dec;19(6):313-20.

128. Hoehn M, Kustermann BJ, Blunk J, Wiedermann D, Trapp T, Buhrle. Monitoring of implanted stem cell migration in vivo: a highly resolved in vivo magnetic resonance imaging investigation of experimental stroke in rat. Proc. Natl Acad Sci USA. 99 2002 16267-72.

129. Pawelczyk E, Arbab AS, Chaudhry A, Balakumaran A, Robey PG, Frank JA. In vitro model of BrdU or iron oxide nanoparticle uptake by activated macrophages from labeled stem cells: implications for cellular therapy. Stem Cells.2007-0707. 2008

130. Stroh A, Zimmer C, Gutzeit C, Jakstadt M, Marschinke F, Jung T, Pilgrimm H, Grune T. Iron oxide particles for molecular magnetic resonance imaging cause transient oxidative stress in rat macrophages. Free Radical Biol Med. 36 (2004) 976-984.

131. Pouliquen D, Le Jeune JJ, Perdrisot R, Ermias A, Jallet P. Iron oxide nanoparticles for use as an MRI contrast agent: pharmacokinetics and metabolism. Magn Reson Imaging. 1991;9(3):275-83.

Chapter 2: Spatial and Temporal Differences in the Development of Brain Metastases due to Breast Cancer Detected by In Vivo MRI

Disclosure: Cell Culture and labeling was done by Catherine McFadden and Emeline Ribot. Also Flow Cytometry was done by Karen Morely and Catherine McFadden. All left ventricle injections and histology were performed by Carmen Simedrea. MRI scanning and analysis was done by Mevan Perera

2.1 INTRODUCTION

Ten to twenty percent of metastatic breast cancer patients will develop brain metastases (1-3). Untreated, the median survival time is 2–3 months and with aggressive treatment is usually extended only marginally, to 4–12 months (4). The incidence of brain metastases in breast cancer patients is increasing (5). This is especially true for women with human epidermal growth factor receptor 2 (HER2/neu) - positive breast cancer (6). This is because patients are surviving primary cancers for longer periods of time as a result of the development of therapeutic agents that successfully treat systemic, but not brain metastases (7). For example, trastuzumab (Herceptin®), a monoclonal antibody which interferes with the HER2/neu receptor, has been shown to be effective at treating systemic metastases in patients with HER2 positive tumors, however, prolonged treatment has shown a high incidence of brain metastases (24-48%) (8). This is likely due to the drug's poor penetration of the blood brain barrier due to its large size, essentially making the brain a sanctuary site for metastases (9).

To study the mechanisms of breast cancer metastasis to the brain, and to investigate promising new therapies for the treatment of brain metastases, mouse models have been developed using human breast cancer cell lines (10-13). Metastases in these mouse models have been characterized by histology, immunohistochemistry, fluorescence imaging and microscopy (14-16). These techniques allow for measurements of the numbers of metastases, the cross-sectional area of metastases and for an analysis of cellular markers of apoptosis and proliferation and other phenotypic characteristics of the tumor.

A limitation of these methods is the need to sacrifice the animal and therefore only an endpoint analysis is permitted. In vivo microimaging technologies, including high-resolution magnetic resonance imaging (MRI), micro-computed tomography (CT) and small-animal positron emission tomography (PET), have shown great utility for characterizing small-animal models of disease (17-19). Anatomical MRI is particularly well suited for studies of brain metastasis because it is noninvasive, three-dimensional, has excellent soft tissue contrast and has no limitation in depth of penetration.

Cellular MRI is a relatively new field of imaging which uses labeling of cells with iron particles, along with the acquisition of high resolution images, to track the fate of cells after their injection or transplantation. This imaging approach is has been used to detect and track a variety of cell types in a number of different animal models of disease (20-25). Areas containing iron-labeled cells appear as regions of low signal intensity (or signal voids) on MRI images, creating negative contrast (26-31). Previous work by the Foster lab, and others, has shown that

even single iron-loaded cells can be detected in vivo by MRI, as signal voids in vivo in the mouse brain (27-29). Heyn et al. monitored the fate of individual cancer cells in the mouse brain and showed that single iron-labeled cells are initially detected as discrete signal voids, and that with time the signal void caused by the iron label is replaced by signal hyperintensity, as cells proliferate diluting the label and developing into metastases (27).

A wealth of information can be derived about the development of metastases from in vivo 3D cellular MRI, when compared to traditional histological analyses. In this study we assess the metastatic potential of two highly brain metastatic human breast cancer cell lines, using multiple MR scans of each mouse over the course of metastasis formation. This approach allowed us to quantify both growing metastases as well as persistent, dormant tumor cells, in the full brain volume of each mouse and at multiple time points. To the best of our knowledge this is the first report of the in vivo spatial and temporal monitoring of the development of experimental brain metastasis by MRI in mice.

2.2 MATERIALS AND METHODS

2.2.1 Cell Culture and MPIO labeling

Two human breast cancer cell lines were used (i) MDA-MB-231BR (231BR), which are a highly brain metastatic derivative of the human MDA-MB-231 breast cancer cell line (16), and (ii) a version of 231BR which were transfected with the human epidermal growth factor receptor-2 (HER2) gene

MDA-MB-231BR/HER2 (231BR/HER2) (17). Both cell lines were previously transfected with enhanced green fluorescent protein (EGFP) using a retroviral vector.

Both cell lines were maintained in media containing 10% FBS at 37°C and 5% CO_2. When labeling with MPIO, 1.5 x 10^5 cells/mL were plated in 2mL of DMEM medium containing 10% FBS per well of a six well plate and allowed to adhere for 24 hours. 24uL of Flash Red Bangs Beads (Bangs Laboratories, Fishers, IN, USA) in 2mL of media were added to each well giving 5.8 x 10^8 MPIO/well and then incubated for 24 hrs. The cells were then washed thoroughly with 2mL of Hanks buffered salt solution (HBSS) to remove unincorporated MPIO.

To detect intracellular uptake of MPIO particles, MPIO-labeled cells were collected following overnight culture, washed 3X with buffer, and deposited onto glass microscope slides using a cytospin centrifuge. Cells were stained for iron with Perl's Prussian blue (PPB) and counter stained with eosin. The EGFP-positive cancer cells and the flash red fluorophore of MPIO-labeled cells were also visualized with fluorescence microscopy on a Zeiss Axioplan 2 microscope. MPIO labeling was further verified with inductively coupled plasma mass spectroscopy (ICP-MS).

For transmission electron microscopy (TEM) cells were fixed overnight in 2.5% glutaraldehyde in 0.1 sodium cacodylate buffer at 4 degrees C, washed in 0.1 M sodium cacodylate buffer, postfixed in 1% osmium tetroxide in 0.1 M

cacodylate buffer for one hour, washed in the buffer and enrobed in noble agar. After washes in distilled water they were stained in 2% uranyl acetate for two hours, dehydrated in a graded series of ethanols, cleared in propylene oxide and embedded in Epon 812 resin. Thin sections were mounted on 300 mesh formvar-carbon coated copper grids, stained with 2% uranyl acetate followed by lead citrate, and viewed on the Philips 410 transmission electron microscope at magnifications as high as 52000x.

The trypan blue exclusion assay was performed to determine the viability of MPIO-labeled and unlabeled control cells. The amount of apoptotic and necrotic cell death was determined by staining cells with 7-Amino-Actinomycin (7-AAD; Becton Dickinson, NJ, USA) and Annexin V (Becton Dickinson, NJ, USA) and analysis was carried out using flow cytometry.

2.2.2 Animal Preparation

Four groups of nude mice (female, nu/nu, 6-8 weeks old, 18-22g, Charles River Laboratories, Wilmington, MA, USA) were studied. Mice were anaesthetized with isofluorane (2% in oxygen) and a 0.1 ml HBSS solution containing MPIO-labeled cancer cells was injected into the left ventricle of the beating heart using a 27 Gauge needle inserted between the third and fourth ribs perpendicular to the sternum, as previously described (26). Mice in Group 1 (n=15) were injected with 175,000 231BR/HER2 cells, mice in Group 2 (n=6) were injected with 175,000 231BR cells, mice in Group 3 (n=6) were injected with 50,000 231BR/HER2 cells. A fourth group of mice (n=8) were also injected with

175,000 231BR/HER2 cells but scanned at different timepoints. The mice were cared for in accordance with the Canadian Council on Animal Care, and under a protocol approved by the University of Western Ontario Animal Care and Veterinary Services. Table 2.1 summarizes the animal groups.

Table 2.1: Summary of groups: # of mice, cell type, number of cells injected

Group #	#of mice	Cell type	# of cells injected
1	5	MDA-MB-231BR/HER2	175000
2	5	MDA-MB-231BR	175000
3	5	MDA-MB-231BR/HER2	50000
4	5	MDA-MB-231BR/HER2	175000

2.2.3 Magnetic Resonance Imaging

Imaging was performed on a 1.5T GE CV/I whole-body clinical MR scanner using a custom-built gradient coil (inner diameter = 12 cm, maximum gradient strength = 600 mT/m, and a peak slew rate = 2000 T/m/s). Prior to being scanned, mice were anaesthetized with isofluorane (2% in oxygen) and were then placed within a custom-built solenoidal mouse head radiofrequency (RF) coil (inner diameter = 1.5 cm). In vivo images were acquired using the 3D balanced steady state free precession (bSSFP) gradient echo pulse sequence.

A relatively short scan was performed on all mice on the same day as the cell injection in order to assess the success of the left ventricle injections and to

select mice to include in the longitudinal imaging study. The bSSFP parameters for these scanning sessions were: 200μm isotropic resolution, TR/TE of 3.2/1.6ms, 35° flip angle (FA), 8 signal averages (NEX) and a receiver bandwidth (rBW) of ±21kHz. The scan time was approximately 8 minutes. Only mice that had numerous regions of signal void visible in the brain on day 0, confirming delivery of cells to the brain, were included in the study.

Group 1 mice were scanned on days 16, 19, 23, 26 and 29 post-injection. Group 2 mice were scanned on days 19, 23, 26 and 29 post-injection, since tumors were not evident until day 19 in Group 1. Group 3 mice were only scanned on day 29. The bSSFP parameters for these imaging sessions were: 100μm isotropic resolution, TR/TE of 5.4/2.7ms, 35° FA, 4 NEX, ±31kHz rBW, and 4 RF phase cycles. Scan times for Groups 1-3 were 62 minutes each. Group 4 mice were scanned on days 1 and 35 post-injection. For the day 1 scanning session the TR/TE was changed to 25/12.5ms to maximize the ability to detect signal voids due to iron and the NEX and resolution were reduced to keep the scan time under an hour; NEX=2, resolution =150x150x200μm. Scan time was 48 minutes for mice in Group 4.

2.2.4 MRI Data Analysis

All of the brain metastases were counted manually in each image for all mice. There were between 152 to 168 MR image slices for each mouse brain. The tumor volumes (all) and the signal void volume (Group 4, day 1 scans) were measured from MR images. All measurements were performed using the image

analysis program VG Studio (Volume Graphics, Heidelberg, Germany). The program allowed the acquired MR data to be visualized in the axial, coronal, sagittal and 3D views.

Individual tumor volumes were measured by a semi-automatic segmentation technique. The operator selects a threshold gray level value, within the tumor, and the tumor region of interest is automatically generated, and the volume calculated in mm^3. The void volume measurement is similar. The threshold for identifying voids is set by averaging the mean pixel intensity of the voids with the mean pixel intensity of the background brain tissue. The resulting pixel intensity is set as the maximum void pixel intensity and the program automatically finds and sums all voids. The total void volume for the brain and brain regions is given in mm^3.

Each of these measurements were obtained for the full volume of the whole mouse brain and for specific brain regions. The brain was divided into four regions: the olfactory, cortex, central brain and posterior brain regions. The olfactory region contained the olfactory bulb and the anterior olfactory nucleus. The cortex region contained the frontal cortex and the cerebral cortex. The central brain region included the hypothalamus, thalamus, midbrain, caudate putamen, ventral striatum, and the basal forebrain. The posterior brain consisted of the cerebellum, pons and medulla. The volume of each of these brain regions was determined.

The number of tumors per region was calculated as a percentage of the total number of tumors in the whole brain. This was determined for all brain

regions at each time point for mice in each group. The volumes of tumors were plotted versus time to assess the tumor growth rates. This was performed for Groups 1 and 2, for all metastases that were first present on day 19.

2.2.5 Statistical Analysis and Growth Plots

Statistical analyses were performed using GraphPad Prism software. Histogram plots were constructed that showed the mean tumor volume and the standard error of the mean (SEM), comparing the BR and HER2 groups at each time point. This was done for the whole brain, cortex, central brain, posterior and olfactory regions. Mann-Whitney tests were conducted to determine if the HER2 and BR groups were significantly different, a separate test was done at each time point to compare the groups. Both sets of data had a non-parametric distribution, this was determined by a Kolmogorov-Smirnov test for normality. Kruskall-Wallis (non-parametric One Way ANOVA) tests were performed to determine if the change in tumor volume between timepoints (19-23), (23-26) and (26-29) was significantly different. This was done for both group 1 and group 2.

2.2.6 Tumor Growth Rate Analysis

Tumor growth rates were determined for mice in Groups 1 and 2 for all metastases that were first apparent in images acquired on day 19. The tumor growth was characterized as either: exponential, logarithmic or linear. To determine this xy plots of volume (mm^3) vs. time (days) of individual tumors was constructed, where the tumor's volume at days: 19, 23, 26 and 29 was plotted.

The type of growth was determined by analyzing the R^2 value of the line of best fit for the three growth types. The growth type with the highest R^2 value was determined to be the best representation of the tumor growth.

2.2.7 Histological Analysis

Following the last in vivo MRI scanning session, mice were euthanized and perfused with cold saline followed by 3.75% formalin. The mouse brains were then removed and cryoprotected in concentrations of sucrose gradient (10%, 20%, then 30% for 24 hrs), then immersed in OCT compound, oriented in a sectioning plane parallel to that of the MR images, and frozen using liquid nitrogen. Continuous 10-μm frozen sections were collected and every second slide was stained for hematoxylin and eosin (H&E). Metastases were then imaged at high and low magnification using a Nikon digital camera and a DXM1200 microscope. The histology images were uploaded into ImageJ (NIH, USA) and the cross sectional area of tumors was measured with the tracing tool from the image processing toolkit.

2.3 RESULTS

2.3.1 Cell Labeling

MPIO was taken up by 231BR and 231BR/HER2 cells and did not affect cell viability. Transmission electron microscopy images show that MPIO particles were taken up into endosomes within cells. Figure 2.1A&B shows a representative EM microscopy image of MPIO-labeled 231BR/HER2 cells. Fluorescence microscopy images show the presence of red fluorescent MPIO particles within 231BR cells, which appear green due to GFP expression (Figure 2.1C). PPB staining also showed that the iron particles were located within the cells (Figure 2.1D).

Labeling cells with MPIO did not affect cell viability, as the trypan blue exclusion assay showed that 98% of labeled and 2% of unlabeled cells were viable after harvesting. There was no significant difference between MPIO-labeled or unlabeled cell populations when Annexin V or 7 AAD, markers for apoptosis and necrosis, were assessed by flow cytometry; representative plots for unlabeled and labeled 231BR cells are shown in Figure 2.2.

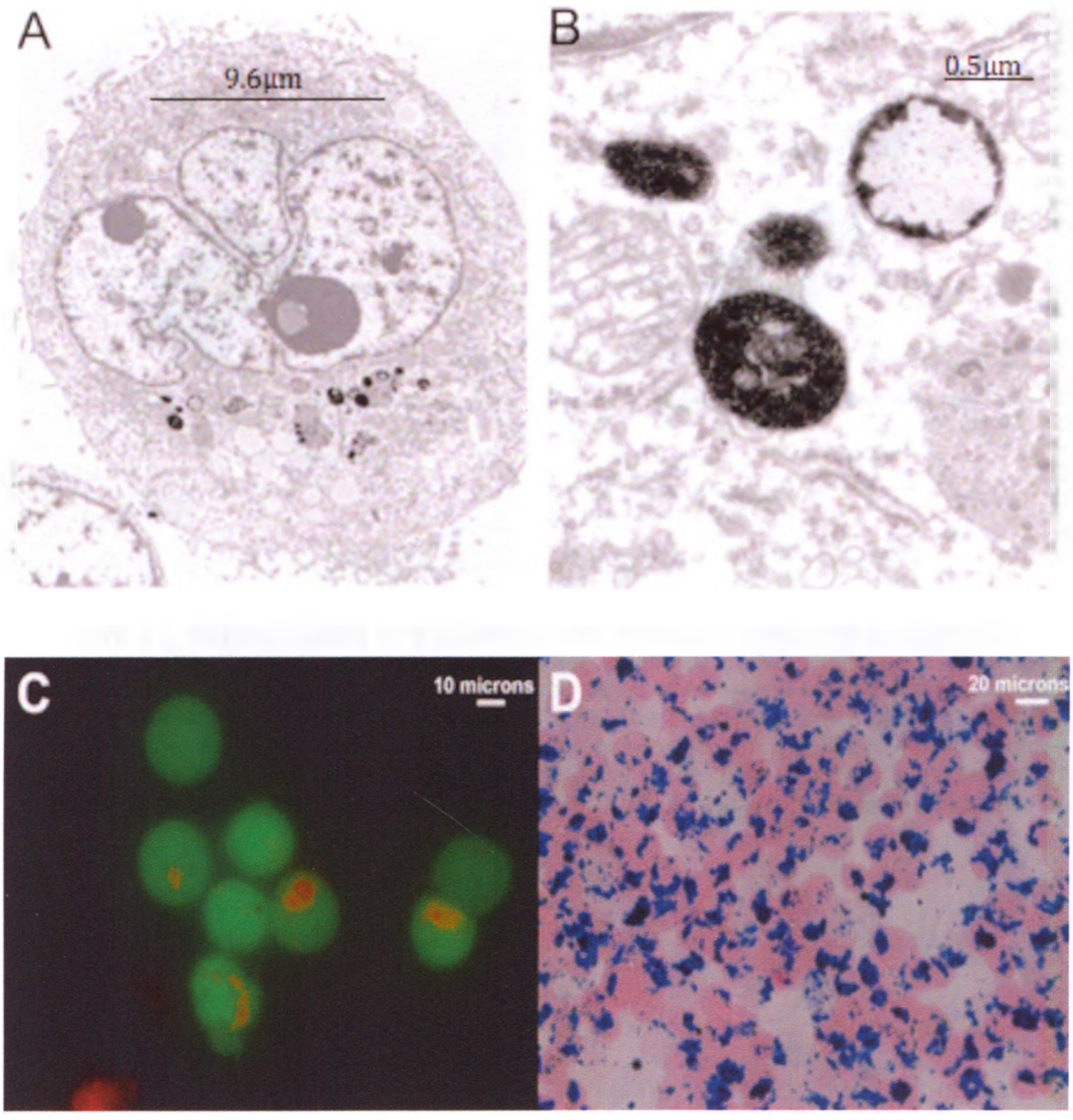

Figure 2.1: MPIO labeling of breast cancer cells. Representative transmission electron microscopy images of MPIO-labeled 231BR/HER2 cells are shown at magnifications of x5500 (A), and x520000 (B). The MPIO particles are compartmentalized in endosomes in the cell cytoplasm and appear as dark punctate regions. Fluorescence microscopy images (C) show the fluorescent tag of MPIO (red) within the GFP positive cells (green); the images are shown at a 100x magnification. (D) Iron appears blue in Perl's Prussian blue stained cytospins (40x).

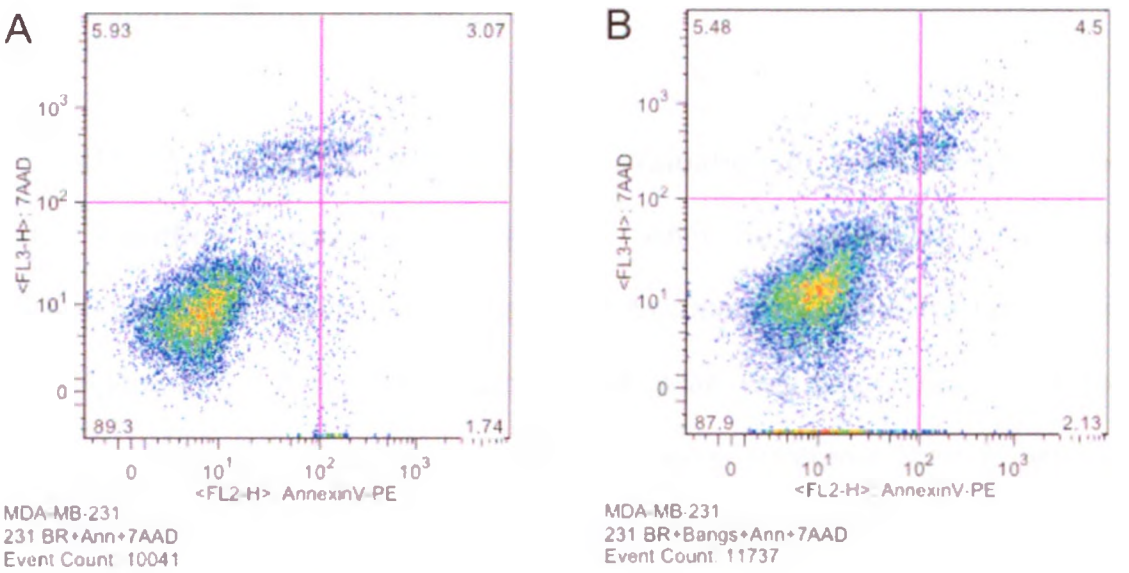

Figure 2.2: Representative flow cytometry dot plots of labelled and unlabeled breast cancer cells. 7AAD/Annexin staining of either unlabeled or MPIO-labeled 231BR cells. There was no significant difference in the percentages of Annexin V positive (apoptotic) cells for unlabeled (1.74%) or MPIO labeled (2.13%). The 7-AAD positive population contains nonviable cells. There was no significant difference in the percentages of 7-AAD positive cells for unlabeled (5.93%) or MPIO labeled (5.48%) MSC. There was also no difference in the percentages of cells that were 7AAD+/Annexin+ which indicates later stage apoptosis.

2.3.2 Imaging – Whole Brain Analysis

MPIO cell labeling allowed for an evaluation of the success of the cardiac injection at day 1 post injection. After the injection of iron-labeled cells MRI images of the mouse brain showed discrete signal voids throughout the brain (Figure 2.3). A relatively quick 'scout' scan was taken the day of the injection to determine if the cardiac injections were successful and to remove mice without good injections from the longitudinal imaging study.

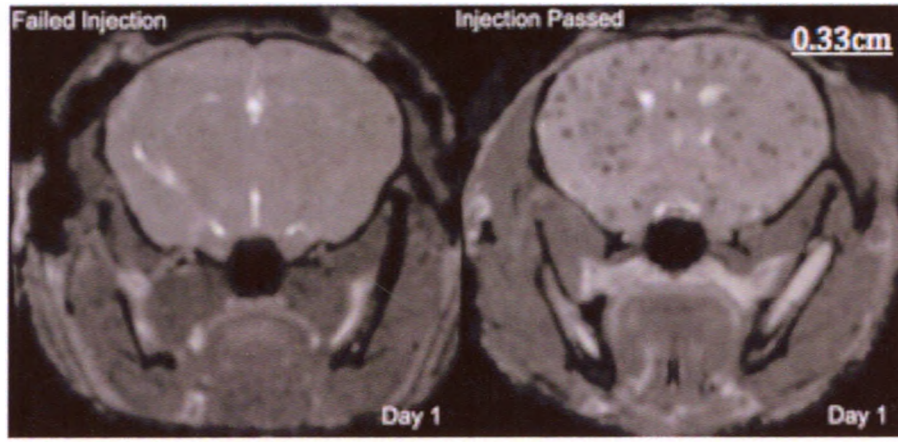

Figure 2.3: Assessing Injections with Cellular MRI
Representative mouse brain images acquired on day 1 post cell injection.
MRI was used to assess the success of intracardiac left ventricle cell injections. Cells labeled with MPIO appear as small signal voids (black). An example of a brain image that indicates that the injection failed (A) shows relatively few voids in comparison to a successful injection with many voids distributed throughout the brain (B).

In Figure 2.3 representative scout images are shown for an example of a failed injection (2.3A), where only a few voids can be detected, and for a mouse with a proper injection (2.3B) where many more voids can be seen in the brain. In Group 1, 8/12 mice had successful intracardiac injections. In Groups 2 and 3 all

injections were successful. In Group 4, 7/8 injections were successful. For each group, 5 of the mice with good injections were selected to follow longitudinal MRI imaging.

There was no difference in the mean number of metastases that developed in mice injected with either 231BR or 231BR/HER2 cells. In bSSFP images, metastases appear with higher signal intensity compared to normal background brain tissue. 3D MRI allowed for images to be examined in all three orientations for the presence of metastases (Figure 2.4).

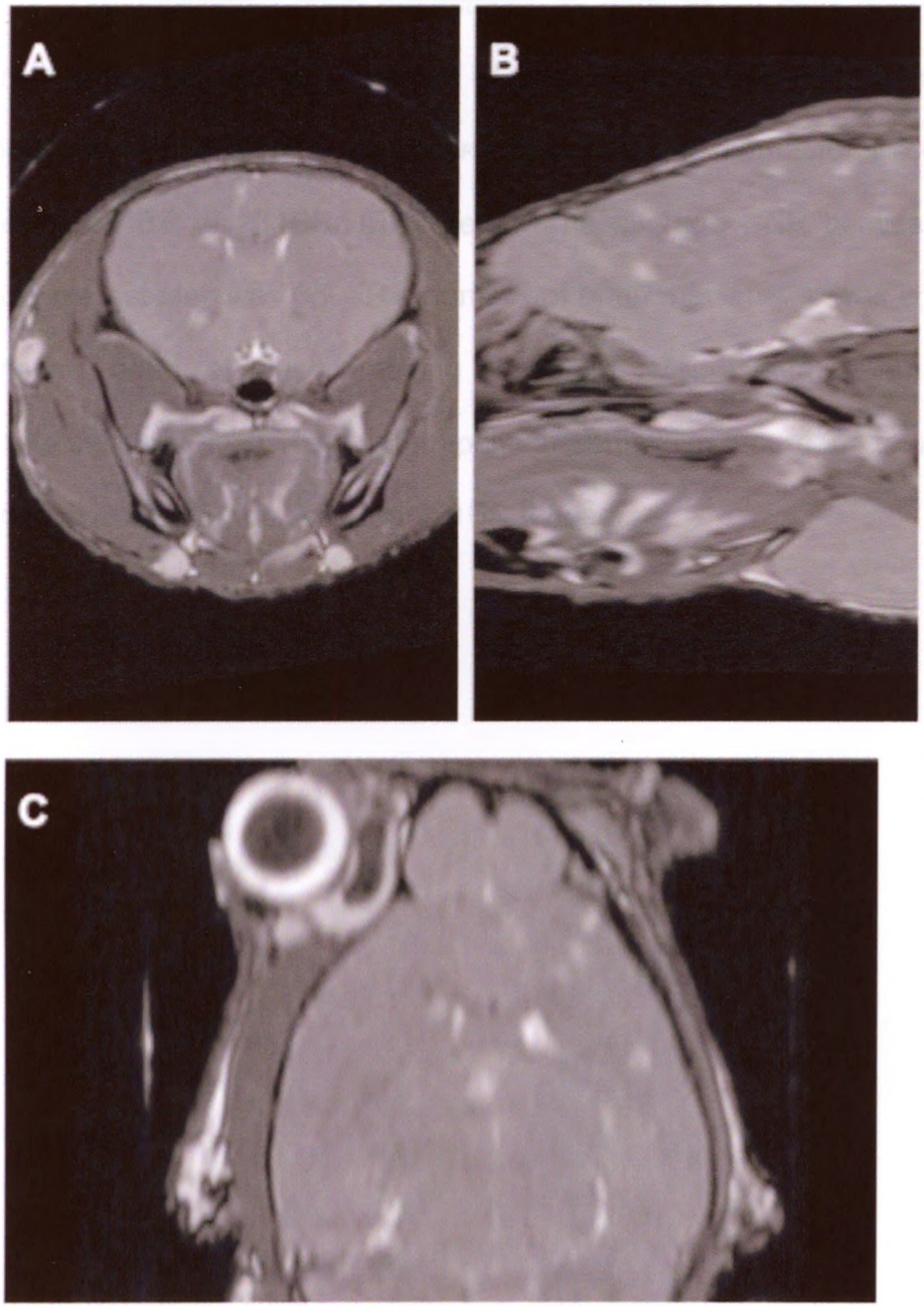

Figure 2.4: Multiplane view of mouse brain. MRI data was acquired in 3D; shown is: axial A, saggittal B and coronal C views of mouse brain. The image set was constructed with OsiriX image visualization software.

MRI detected brain metastases as early as 19 days post-injection for all mice. New metastases appeared at each imaging timepoint, up to and including endpoint scans. Brain metastases appeared the same for mice injected with either 231BR or 231BR/HER2 cells. The average CNR between normal brain and metastases was 35. The number of brain metastases was counted for each mouse brain at each imaging timepoint. Representative images of brain metastases at each imaging timepoint are shown in Figure 2.5 for a 231BR/HER2 mouse and in Figure 2.6 for a 231BR mouse.

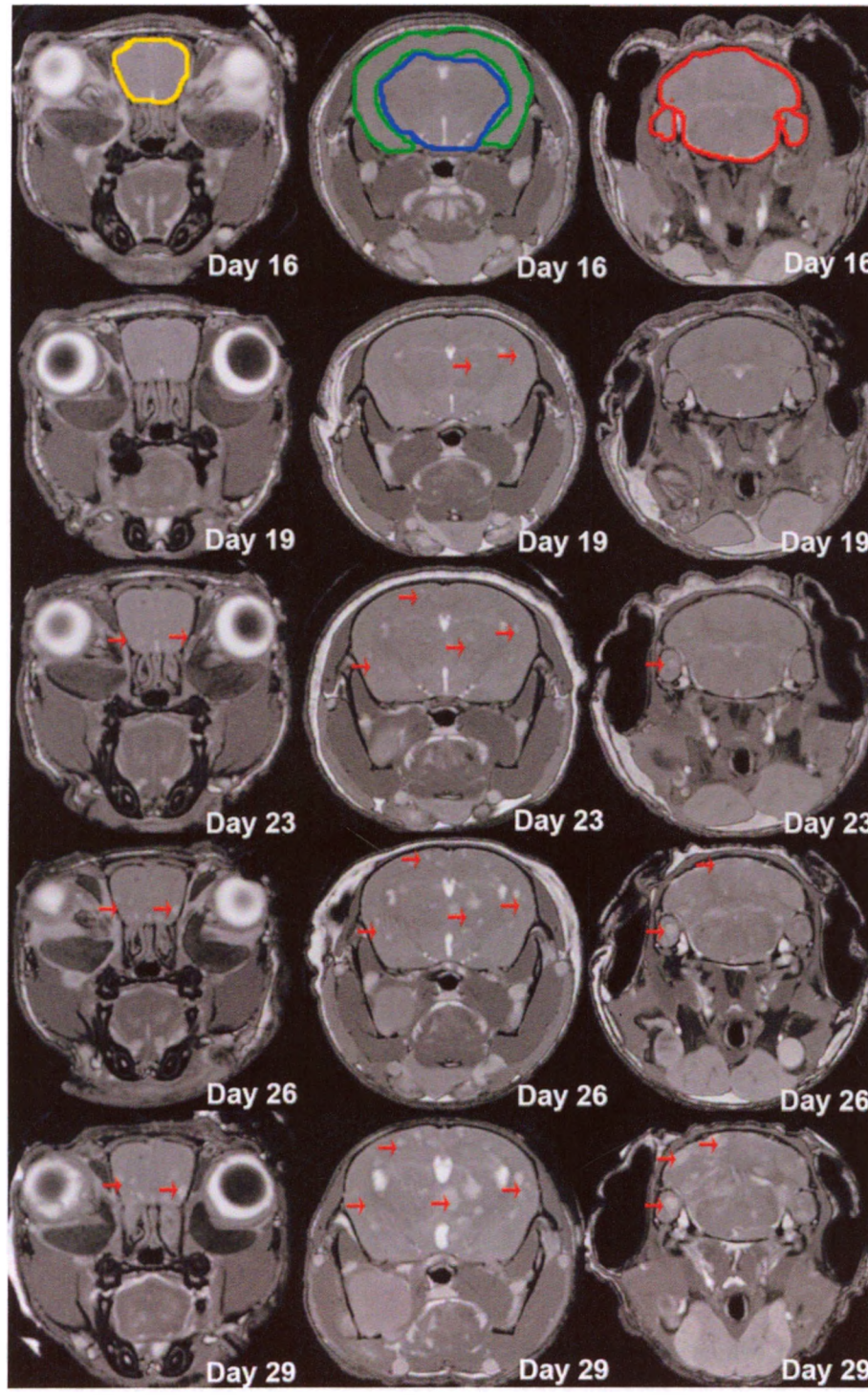

Figure 2.5: Monitoring Tumor Growth MDA-MB-231BR/HER2 Representative mouse brain images showing the development of brain metastases of a mouse injected with 231BR/HER2 cells. Metastases appear as regions with high signal compared to normal brain (arrows). Metastases were first apparent in images at Day 19. Metastases development is shown for tumors forming in the olfactory region (outlined yellow), the cortex (outlined green), central brain (outlined blue) and the posterior region (outlined red).

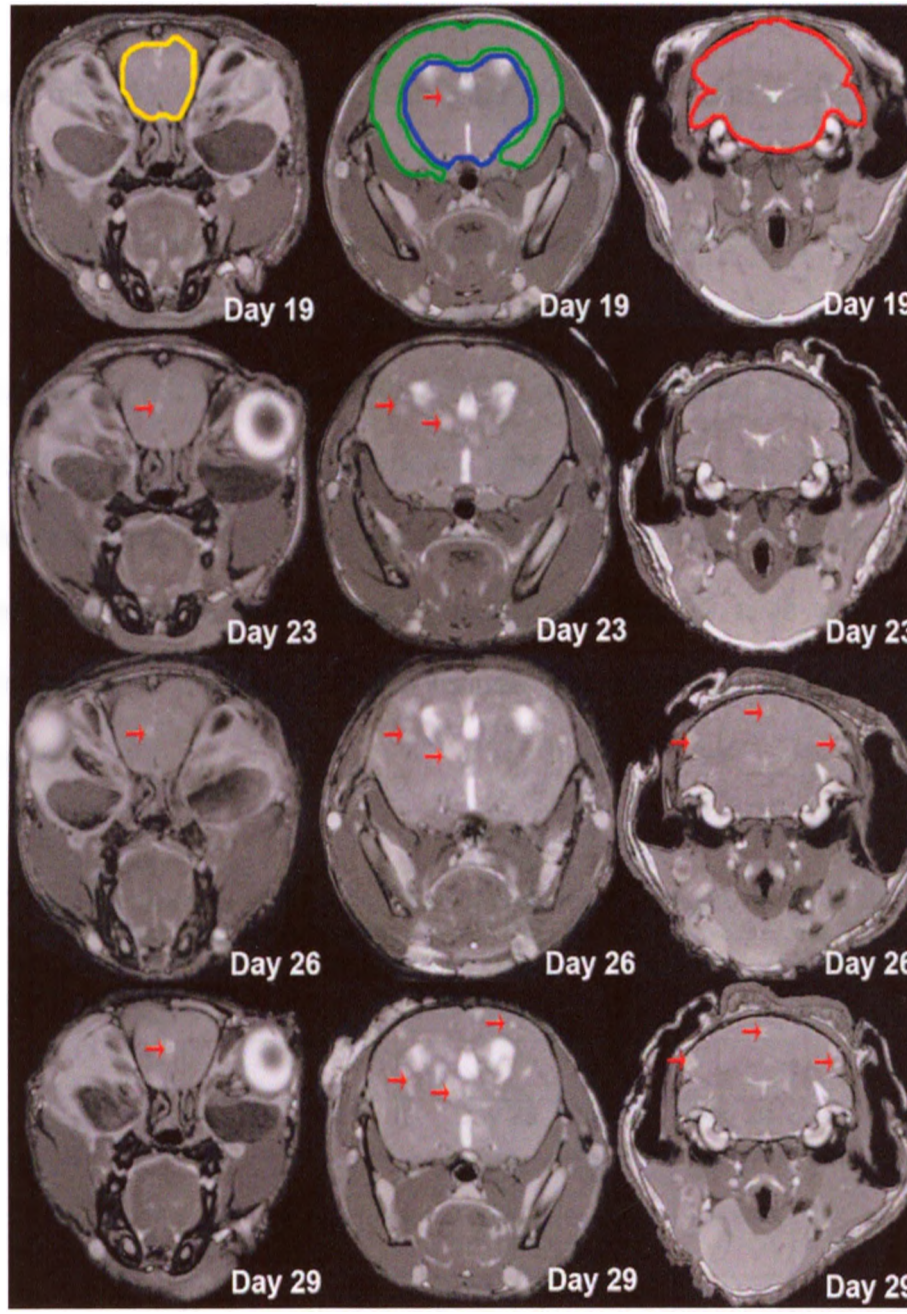

Figure 2.6: Monitoring Tumor Growth MDA-MB-231BR Representative mouse brain images showing the development of brain metastases of a mouse injected with 231BR cells. Metastases appear as regions with high signal compared to normal brain (arrows). Metastases were first apparent in images at Day 19. Metastases development is shown for tumors forming in the olfactory region (outlined yellow), the cortex (outlined green), central brain (outlined blue) and the posterior region (outlined red).

The number of metastases present at each timepoint varied substantially between mice for both groups. The total number of tumors at the first imaging timepoint varied between 4 and 64 for mice injected with 231BR cells (Table 2.2) and between 17 and 101 for mice injected with 231BR/HER2 cells (Table 2.3). There was no statistically significant difference in the mean number of metastases for mice injected with 231BR cells compared to mice injected with 231BR/HER2 cells for any timepoint, where $P<0.05$. At endpoint the mean number of tumors for mice injected with 231BR cells was 119±57.4 and the mean number of tumors for mice injected with 231BR/HER2 cells was 84±75. The dash in the table denotes that the mouse was sacrificed before imaging could commence.

Table 2.2: Summary of the number of metastases, 231BR/HER2, in MR images of the whole mouse brain for mice injected with 175 000 231BR/HER2 cells (Group 1). A dash indicates that the mouse was sacrificed before imaging could take place at the given time point.

	Group 1			
	Day 19	Day 23	Day 26	Day 29
M1	20	32	42	43
M2	74	121	-	-
M3	101	161	190	-
M4	91	148	169	171
M5	17	26	32	38
Total	303	488	433	252
Mean ± standard deviation	61±40	98±64	108±83	84±75

Table 2.3: Summary of the number of metastases, 231BR, in MR images of the whole mouse brain for mice injected with 175 000 231BR cells (Group 2). A dash indicates that the mouse was sacrificed before imaging could take place at the given time point.

	Group 2			
	Day 19	Day 23	Day 26	Day 29
M1	25	61	105	127
M2	38	56	139	-
M3	4	12	20	45
M4	24	75	88	120
M5	64	119	104	185
Total	155	323	456	477
Mean ± standard deviation	31±22	65±38	91±44	119±57.4

Brain metastases were larger in mice injected with 231BR/HER2 cells relative to mice injected with 231BR cells. During the analysis of tumor volumes the volume of each tumor counted at each imaging timepoint was determined; in total 2888 tumor volumes were determined. The mean tumor volume was larger for mice in Group 1, that received 175,000 231BR/HER2 cells, compared to mice in Group 2, that received 175,000 231BR cells (Figure 2.7A). Figure 2.7B shows an illustration of the surface rendering performed for measuring tumor volumes.

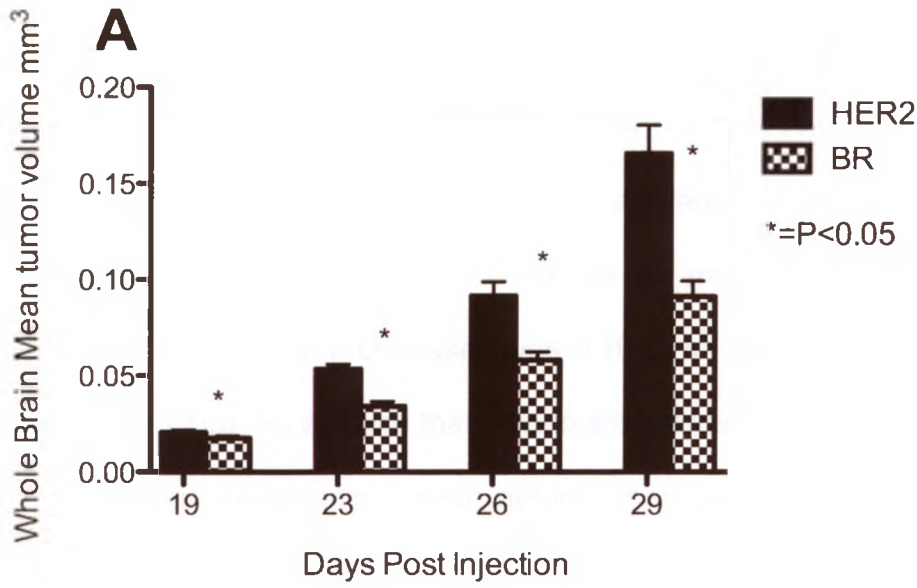

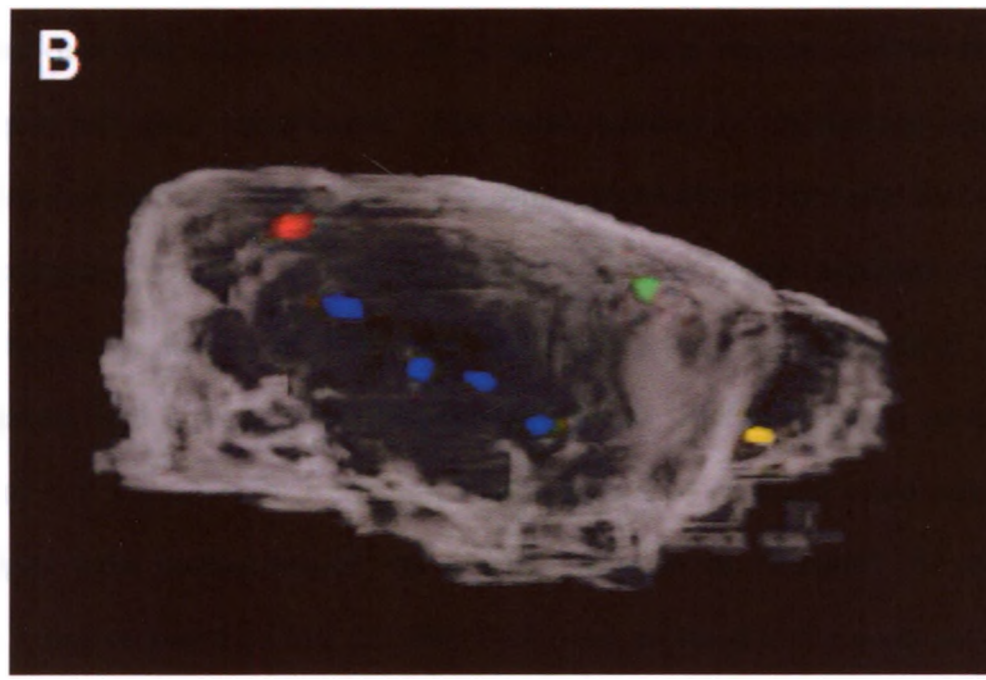

Figure 2.7: Tumor Volumes, HER2 vs. BR (A) Mean tumor volumes in the whole brain. The black bars represent the tumor volumes for mice in Group 1, injected with 175,000 231BR/HER2 cells, and show that at each time point the mean tumor volume was greater for these mice than for mice in Group 2, injected with 175,000 231BR cells (checked bars). The asterisk denotes statistical significance where $p<0.05$, where the HER2 group had a larger mean tumor volume. The number of tumors whose volume was measured is summarized in table 2.2 and 2.3 in the row "total". **(B)** 3D rendering of the brain metastases from MR images of a mouse at day 29 post injection; yellow denotes metastases those that formed in the olfactory region, green in the cortex, blue in the central brain and red denotes metastases that formed in the posterior region.

Brain metastases were larger in mice that developed fewer tumors at endpoint. When comparing the volumes of tumors from mice that developed fewer than or greater than 50 metastasis by endpoint we observed that mice with fewer metastases had larger metastases on average. This was independent of the cell line. The mean tumor volume for all mice in Groups 1 or 2, that developed fewer than 50 metastases was 0.16 mm^3, compared to a mean tumor volume of 0.08 mm^3 for all mice that developed greater than 100 metastases.

A similar observation was noted when comparing the volumes of metastases at endpoint for mice in Group 3, that received 50,000 231BR/HER2 cells and had fewer than 50 metastases by the endpoint, with mice in Group 1, that had over 100 metastases by the endpoint. Mice injected with fewer cells developed far fewer metastases. The mean number of metastases (mean ± standard deviation) for mice in Group 3, which received 50,000 cells was 19.0 ± 6.70, compared to 160.0 ± 35.6 for mice in Group 1, which received 175,000 cells. However, the mice that received fewer cells, and developed fewer metastases, had a significantly larger mean tumor volume (mean ± standared error) (0.172 ± 0.025 mm^3) compared with mice that received more cells and developed more metastases (0.108 ± .016 mm^3), where $P<0.0001$. All mice in Group 3, that received 50,000 231BR/HER2 cells, survived to the endpoint of the study.

2.3.3 Imaging – The Distribution of Metastases

The majority of the brain metastases were located in the cortex and central brain regions. This is illustrated in Figure 2.8. A similar trend in the spatial distribution of brain metastases was observed in all mice examined, regardless of cell line or cell number. At the endpoint more than 90% of all brain metastases were located in the cortex and central brain regions. In Group 2 mice, 50-60% of metastases were in the cortex, 25-32% were in the central brain, 6-10% were in the posterior brain and 3-6% of metastases were located in the olfactory region. Similarly, for mice in Group 1 60-69% of metastases were in the cortex, 26-31% were in the central brain, 1-5% were in the posterior brain and 2-3.5% of metastases were located in the olfactory region. Mice in Group 3 were only examined at endpoint. In this group 59% of the metastases were in the cortex, 32% were in the central brain, 7% were in the posterior brain and 2% of metastases were located in the olfactory region

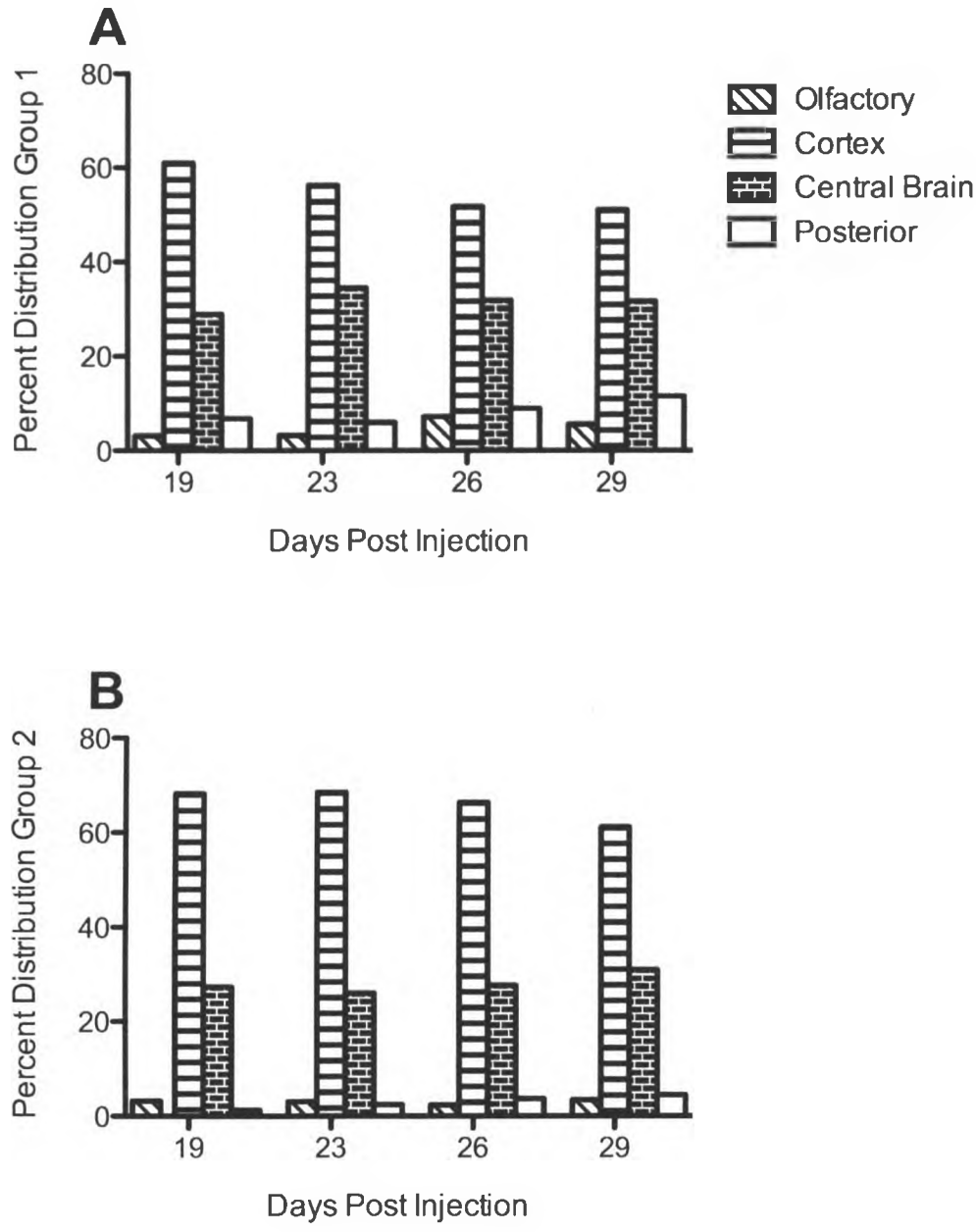

Figure 2.8: The relative distribution of metastases in the mouse brain is shown for Group 1 n=5 mice(A) and Group 2 n=5 mice (B). The percent distribution of tumors in each brain region is shown for all time points. In both groups more than 50% of the metastases were located in the cortex, at all timepoints. Between 25-30% of metastases formed in the central brain for both Group 1 and 2 at each time point. Fewer metastases were located in the posterior and olfactory regions. For Group 1 there were 6-10% in the posterior region and 3-6% in the olfactory region. For Group 2, 1-5% of metastases were in the posterior brain and 2-3.5% were in the olfactory region. The distribution was determined for the compiled number of metastases of the n=5 mice from each group. Percentage was used because some mice were sacrificed before the day 29 endpoint.

The volumes of brain metastases were different between brain regions. Figure 2.9 shows the mean tumor volumes for each of the different brain regions. In the cortex and central brain regions (2.9A., 2.9.B) the mean tumor volume was larger for mice in Group 1 compared to mice in Group 2, at each timepoint. This is the same observation as for the tumor volumes in the whole brain (Fig. 2.7). In the olfactory region (2.10A) the mean volume at endpoint is larger for mice in Group 1, although this difference did not reach statistical significance, where $p<0.05$. The trend in the posterior brain region (2.10.A) is similar to the cortex and central brain regions although the differences between the two cell types are not significant at two of the timepoints.

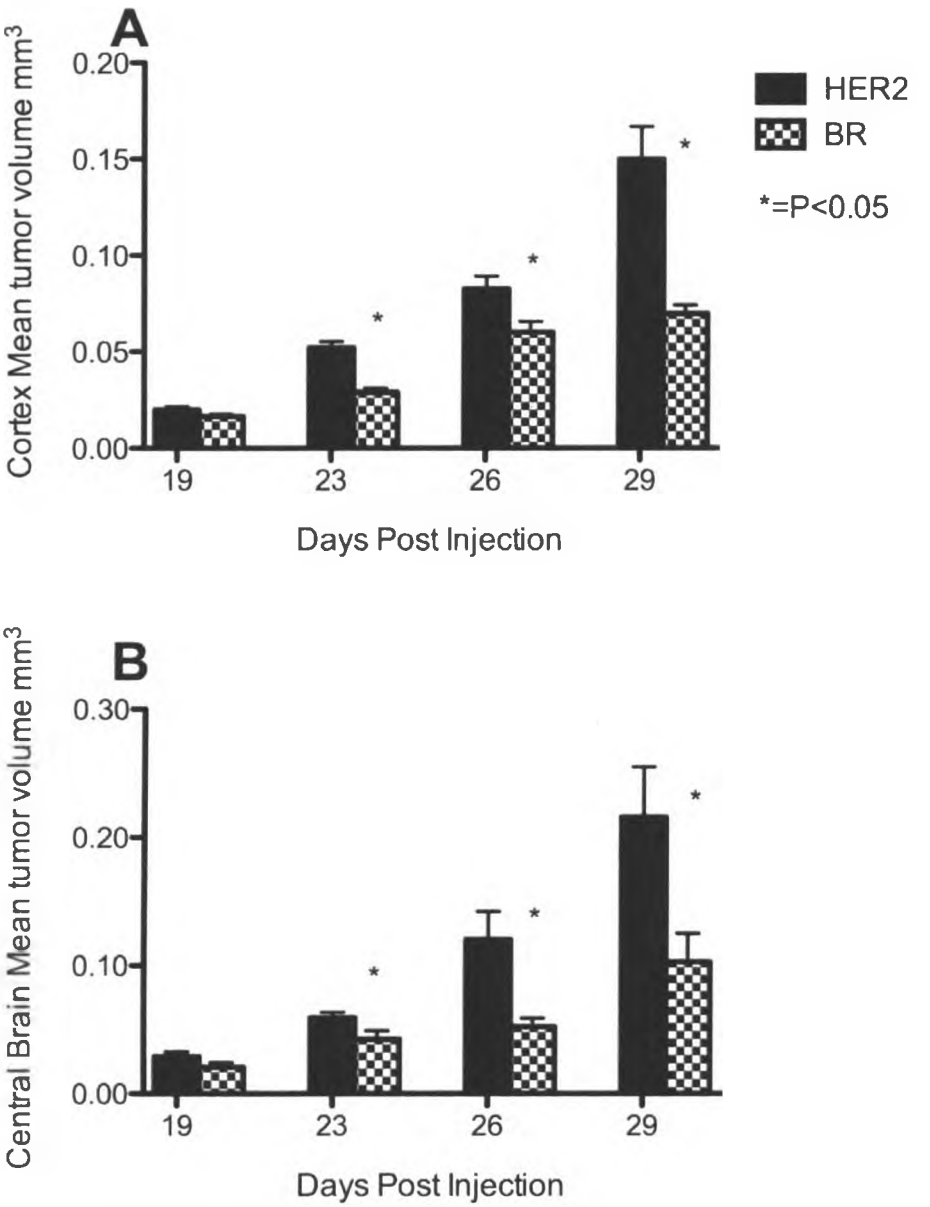

Figure 2.9: Mean tumor volumes in brain regions, HER2 vs. BR. Shown are the mean tumor volumes of HER2 and BR progeny found in the Cortex (A) and Central Brain (B) at time points: 19, 23, 26 and 29. Asterisks denote statistical significance, where $p<0.05$. Group 1 (HER2) metastases were significantly larger than Group 2 (BR) metastases in the cortex and central brain at days 23, 26 and 29 post injection. The highest number of metastases were found in these two regions and similar to the whole brain the mean tumor volume of the HER2 tumors was significantly larger than the BR group.

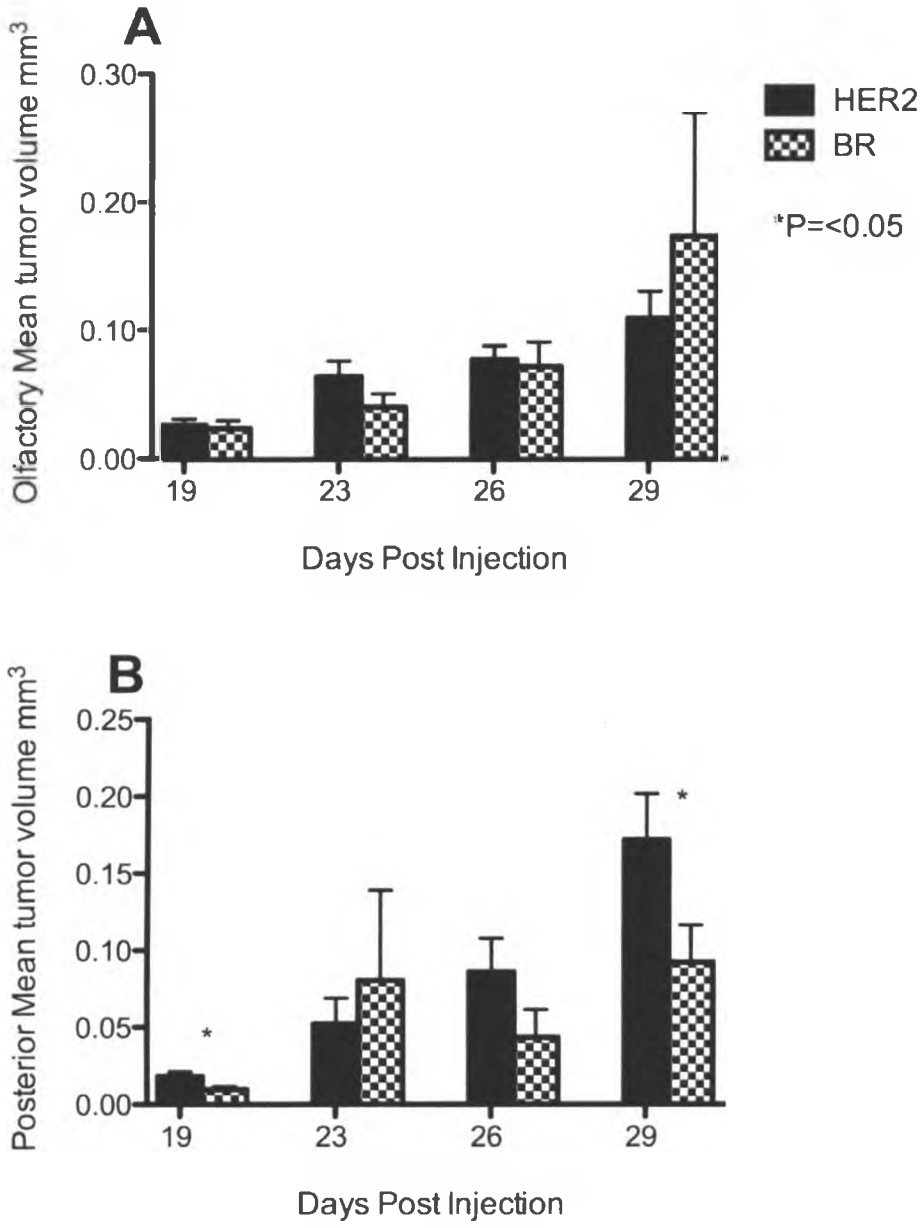

Figure 2.10: Mean tumor volumes in brain regions, HER2 vs. BR. Shown are the mean tumor volumes of HER2 and BR progeny found in the Olfactory (A) and Posterior (B) at time points: 19, 23, 26 and 29 Asterisks denote statistical significance, where $p<0.05$. The volumes of metastases in the olfactory region were not different between the two groups. Mice from Group 1 had significantly larger metastases in the posterior region than Group 2 at days 19 and 29 post injection. The fewest number of metastases were found in these regions. Of note is the appearance that the mean tumor volume for the BR in the posterior (B) at day 26 is lower than day 23 and this may be attributed to a number of factors such as (1) small image artifact that may appear to be tumors and was measured, (2) new small metastases that would have reduced the overall group mean and (3) unstable conditions that may have reduced the size and number of tumors.

The number of developing brain metastases does not reflect the size of the brain region. Next we asked whether the reason there were more metastases located in the cortex and central brain regions was simply because these brain regions were larger than the others. We determined the mean brain volume and the mean volumes of each brain region. The individual brain region volumes were (mean ± standard deviation) : cortex = 141.51 ± 9.09 mm^3, central brain = 143.06 ± 6.81 mm^3, posterior brain = 104.8 ± 4.05 mm^3 and olfactory region = 22.4 ± 3.39 mm^3. The average volume of the whole brain was 411.5 ± 19.9 mm^3; therefore the cortex occupied approximately 34% of the whole brain, the central brain 35%, the posterior brain 26% and the olfactory region 5%. Comparing the percentage of the whole brain occupied by a certain brain region, with the percentages of each brain region occupied by tumors, indicates that the size of the brain region is not likely a major determinant of the incidence of metastases. For example the volumes of the cortex and the central brain are nearly equal despite large differences in the numbers of metastases. The volume of the posterior brain region is 26% of the brain and only 1-10% of metastases were located in this region.

The majority of the arresting cells were located in the cortex and central brain regions. We assessed the distribution of the signal voids that were visible on day 1 after cell injection, due to the arrest of MPIO-labeled cells, for mice in Group 4, which were injected with 175,000 231BR/HER2 cells, and compared it to the distribution of brain metastases at endpoint. A trend for the distribution of signal voids was found which mimicked the trend for the distribution

of brain metastases (Figure 2.11). On day 1, 51% of the void volume was located in the cortex, 27% in the central brain, 16% in the posterior brain and 6% in the olfactory region. At endpoint 54% of metastases were found in the cortex, 34% were located in the central brain, 10% in the posterior brain and 2% were located in the olfactory region. The distribution of brain metastases for this group of mice was very close to what we had previously observed in all other mice. This suggests that the distribution of brain metastases is related to the initial distribution of arresting cells.

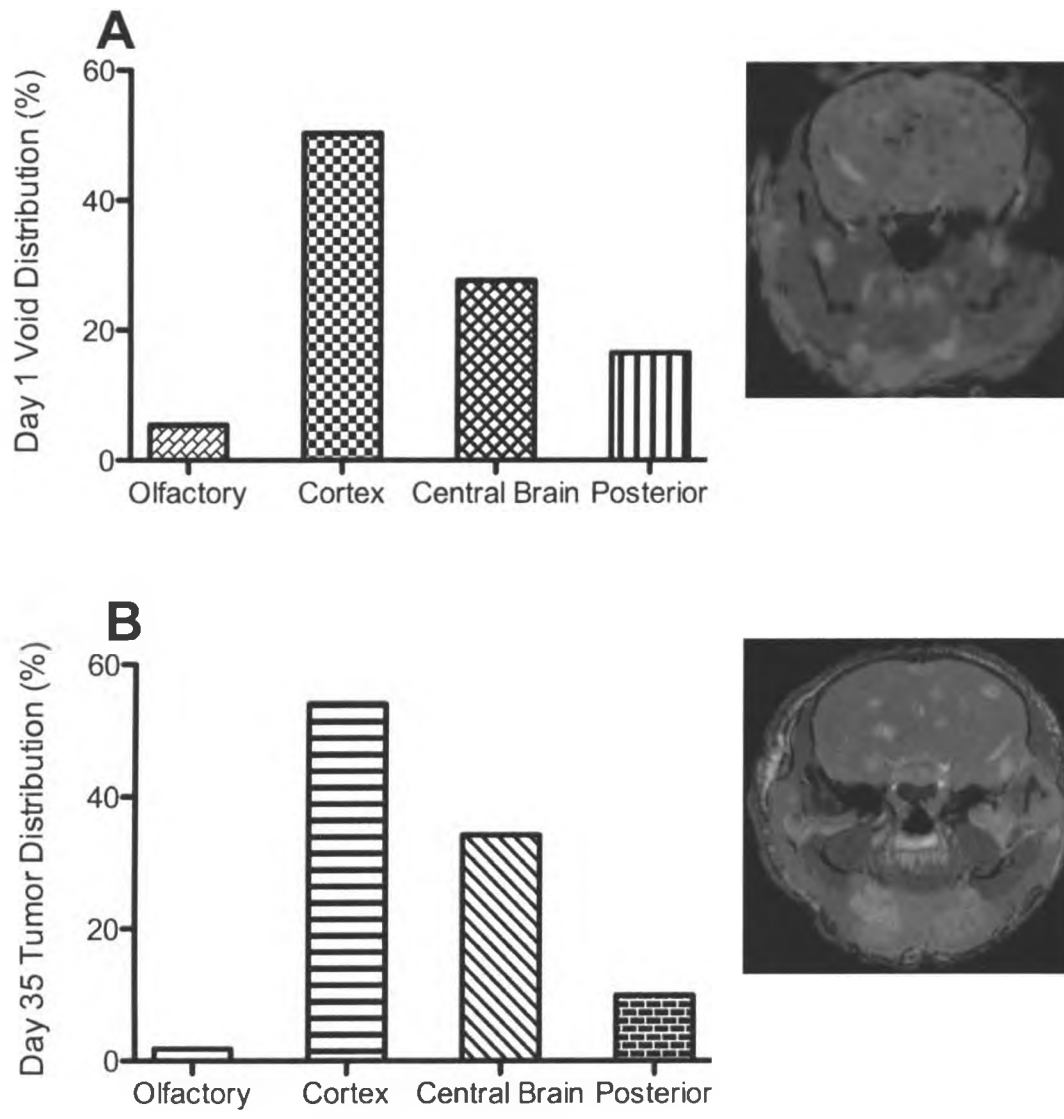

Figure 2.11: Comparing distribution of cancer cells after injection (day 1) A with the distribution of metastases at endpoint (day 35) B for mice in Group 4. The distribution of voids in the brain was similar to the distribution of metastases by the endpoint, where the majority of both formed in the cortex, central brain, posterior and olfactory in descending order. **Histogram A:** 50% of the voids detected in the mouse brain were located in the cortex region. 27% of the voids were located in the central brain. Smaller percentages of the voids were located in the posterior (16%) and olfactory (6%) regions. Histogram B: shows the distribution of metastases at day 35 post injection was similar to the distribution of voids for the cortex (53%) and the central (34%) brain regions. Only 10% of the metastases were located in the posterior brain and only 2% of the metastases were located in the olfactory region. Beside histogram A is an MRI image of a slice in the brain on day 1, which contained voids (hypointense). Beside histogram B is an MRI image of a slice in the brain on day 35, which contained tumors (hyerintense).

It is interesting also to note that the ratio of number of tumors at endpoint: void volume on day 1 is approximately 1 for the cortex and central brain regions and approximately 0.5 for the posterior and olfactory brain regions. This suggests that a much smaller proportion of the cells which arrest in the brain for the posterior and olfactory regions go on to form metastases compared to the cells which arrest in the cortex and central brain regions and that both the initial arrest and the survival of cells in particular brain regions is important.

2.3.4 Growth Rates Analysis

Figures 2.12, 2.13, 2.14 and 2.15 show examples of tumors that displayed exponential, logarithmic and linear growth. The majority of metastases displayed exponential growth, this was true for both Group 1 and Group 2. Exponential growth was observed in 89 ± 7.9% of brain metastases from Group 1. 71 ± 5.29% of brain metastases showed exponential growth in Group 2. 6.83 ± 1.91% of metastases in group 1 showed linear grown and 16.6 ± 8.1% of metastases in group 2 showed linear growth. 4.2 ± 5.9% of metastases showed logarithmic growth for group 1 and 12 ± 5.29% of metastases showed logarithmic growth for group 2. Growth rates were measured for a total of 122 and 79 tumors for group 1 and group 2, respectively. The majority of the growth rates measurements were for metastases that were located in the cortex and the central brain. Fewer growth rates measurements were made for metastases in the olfactory and posterior regions because fewer metastases were present in these regions at day 19. Appendix 1 shows additional growth curves for a representative mouse from each of Group 1 and 2.

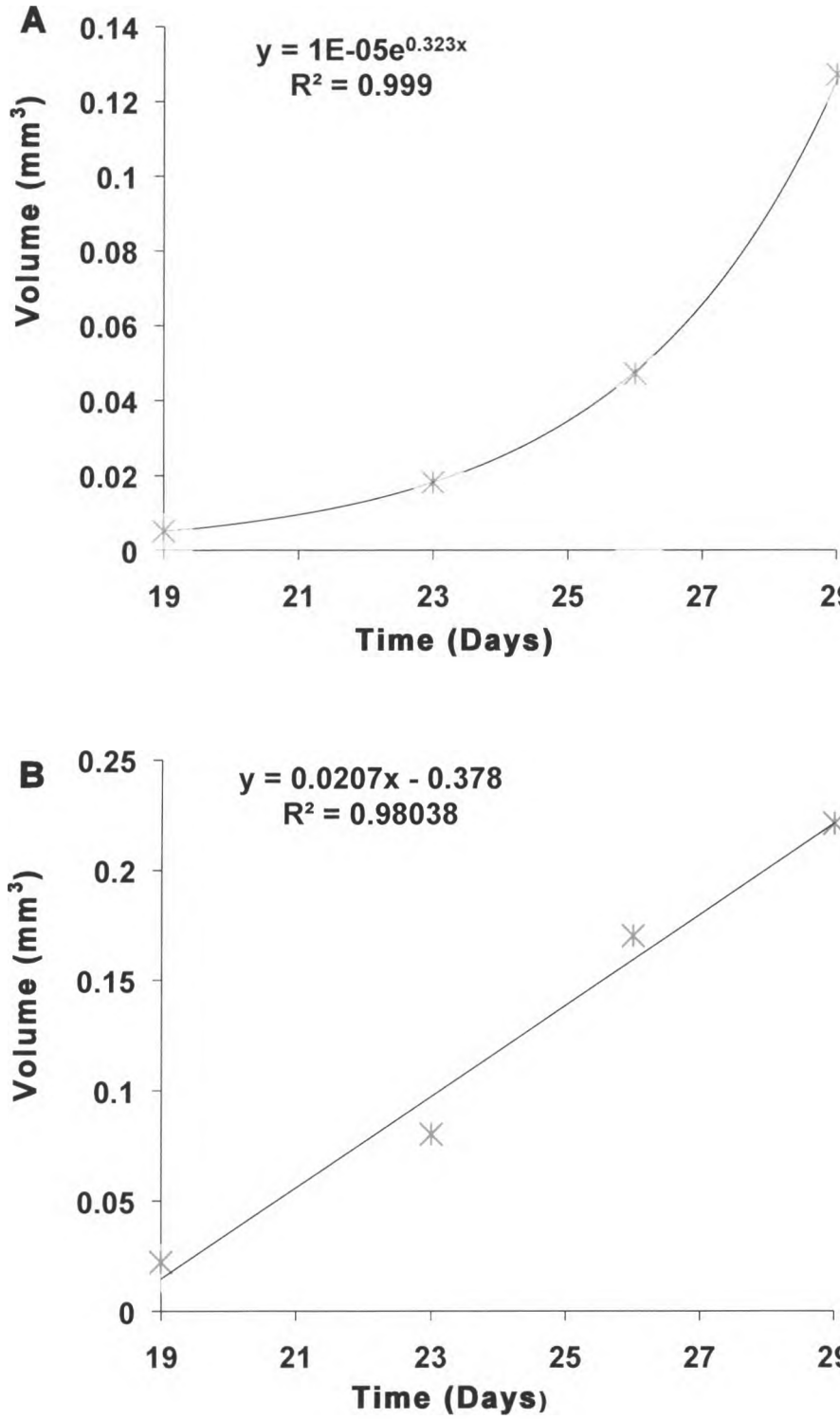

Figure 2.12: Example of tumors that showed exponential A and linear B growth. Tumor volume at days: 19, 23, 26 and 29, was plotted on a volume vs. time Cartesian coordinate system. Shown are sample growth curves for tumors from Group 1, 89% of mice in this group showed exponential growth and 6.83% of tumors showed linear growth.

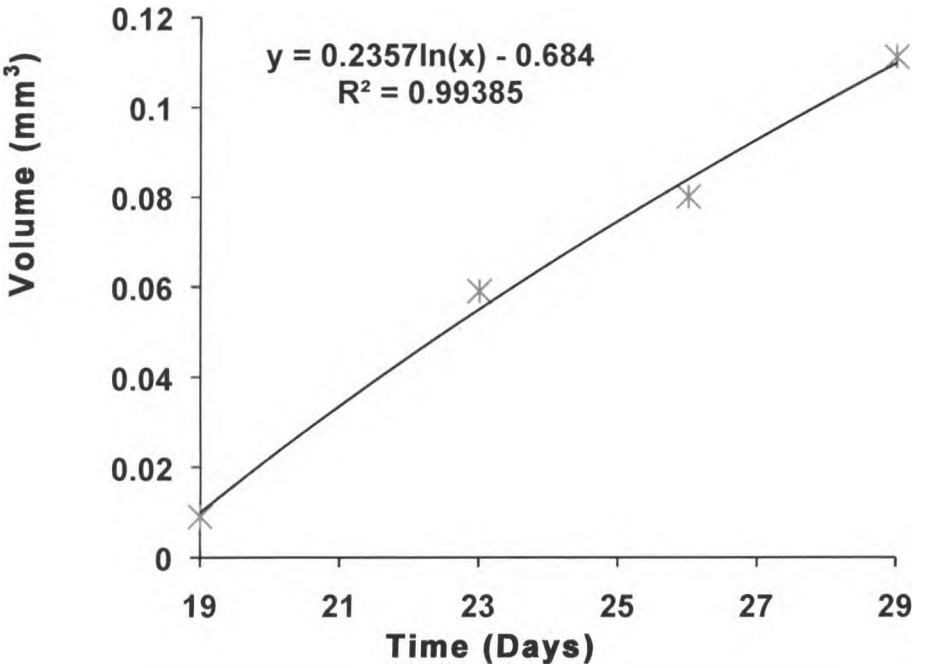

Figure 2.13: Example of a tumor that showed logarithmic growth. Tumor volume at days: 19, 23, 26 and 29, was plotted on a volume vs. time Cartesian coordinate system. Shown is a sample growth curve for a tumor in Group 1 that had logarithmic growth. 4.2% of tumors showed logarithmic growth in group 1.

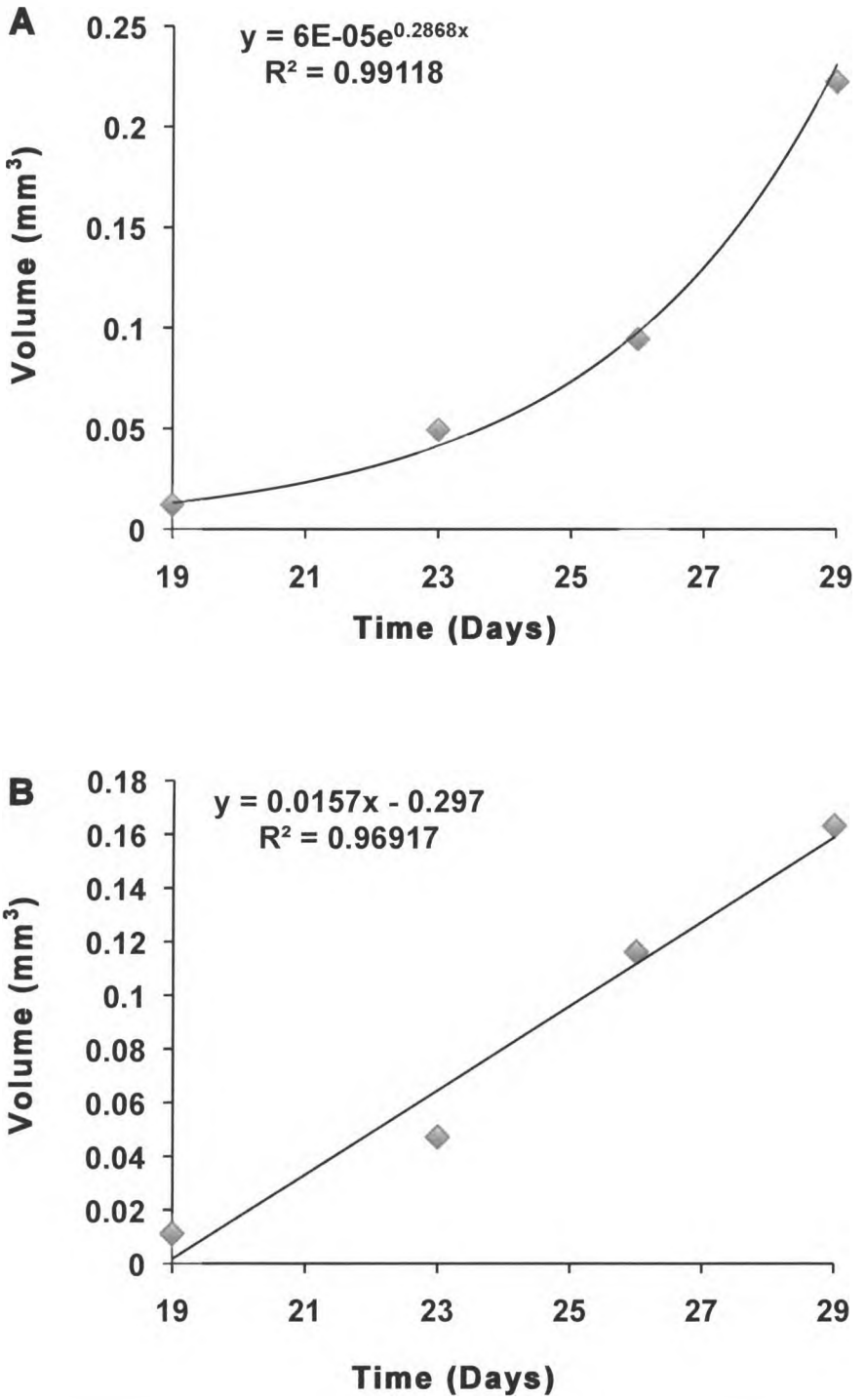

Figure 2.14: Example of tumors that showed exponential A and linear B growth. Tumor volume at days: 19, 23, 26 and 29, was plotted on a volume vs. time Cartesian coordinate system. Shown are sample growth curves for tumors from Group 2, 71% of mice in this group showed exponential growth and 16.6% of tumors showed linear growth.

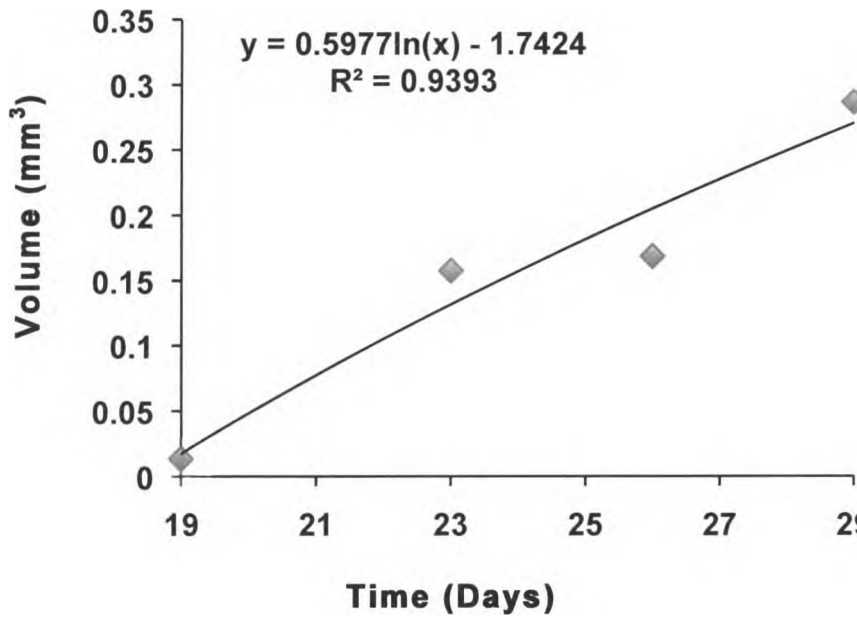

Figure 2.15: Example of a tumor that showed logarithmic growth. Tumor volume at days: 19, 23, 26 and 29, was plotted on a volume vs. time Cartesian coordinate system. Shown is a sample growth curve for a tumor in Group 2 that had logarithmic growth. 12% of tumors showed logarithmic growth in group 2.

Metastatic growth was most rapid at later time points. This was true for both Group 1 and Group 2 mice. The change in tumor volume was calculated between time points 19-23, 23-26 and 26-29. The mean change in tumor volume was significantly higher at the later time points ($P<.0001$), for both Group 1 (Figure 2.16A) and Group 2 (Figure 2.16B).

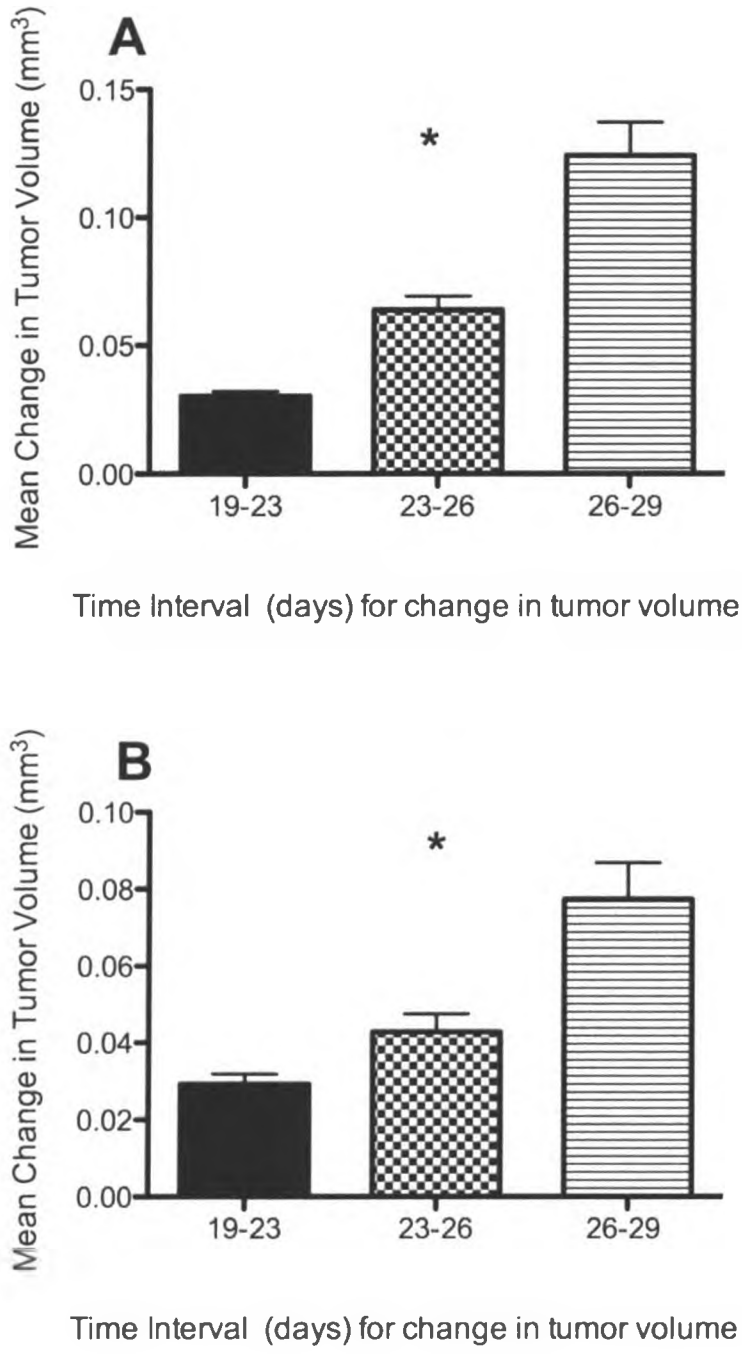

Figure 2.16: **Mean change in tumor volume for group 1 (A) and group 2 (B) metastases.** Kruskal-Wallis test confirmed that the change in tumor volume was statistically significant where *= P<0.0001 for both groups.

The mean change in tumor volume for the individual regions is summarized in Figure 2.17 for group 1 (A) and group 2 (B). The data was compiled of metastases that were first identified on day 19 and were found in the olfactory, cortex, central brain and posterior regions for all mice in the study. Only the cortex in both groups and the central brain in group 1 showed a trend similar to Fig. 2.16, where the change in tumor volume was most rapid at later time points. A higher number of metastases were accounted for in these regions and the number of metastases may have affected the trend.

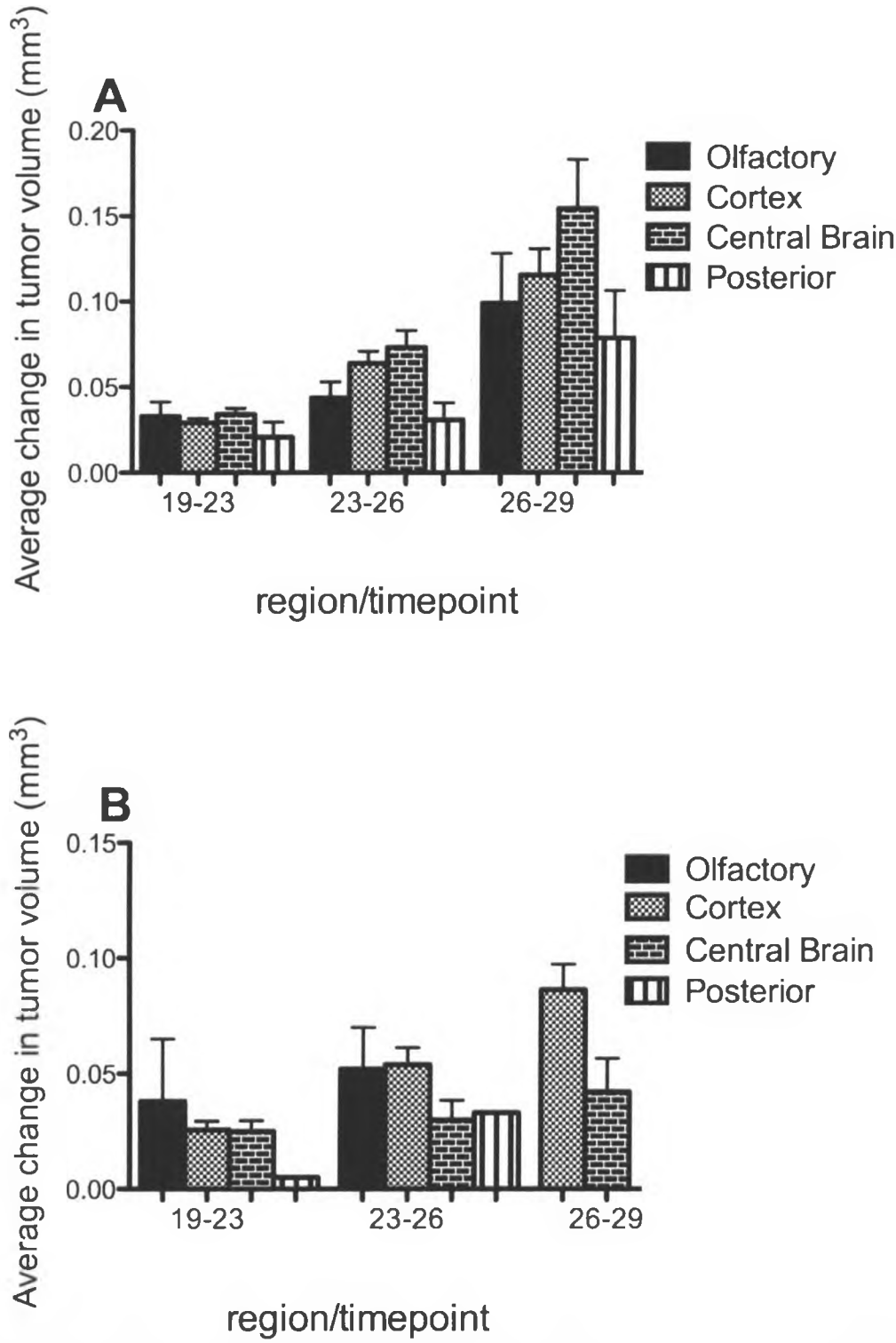

Figure 2.17: Plots of average change in tumor volume for group 1(A) and group 2 (B) for tumors that were first identified on day 19 in the olfactory, cortex, central brain and posterior regions. The tumor data was compiled between all mice in the study for both groups. Only the cortex in both groups and the central brain in group 1 showed a trend similar to Fig. 2.16, where the change in tumor volume was most rapid at later time points.

2.3.5 Histological Analysis

Figure 2.18 shows representative H&E stained sections from a mouse brain and illustrates the varied appearance of the metastases. Metastases appeared in both the parenchyma and the meninges and in all areas of the brain. Most metatases appeared as groupings of smaller clusters of cells (A,B) and were surrounded by spaces that were likely fluid filled. Smaller metastases were also detected as individual cells or small cell clusters (C,D).

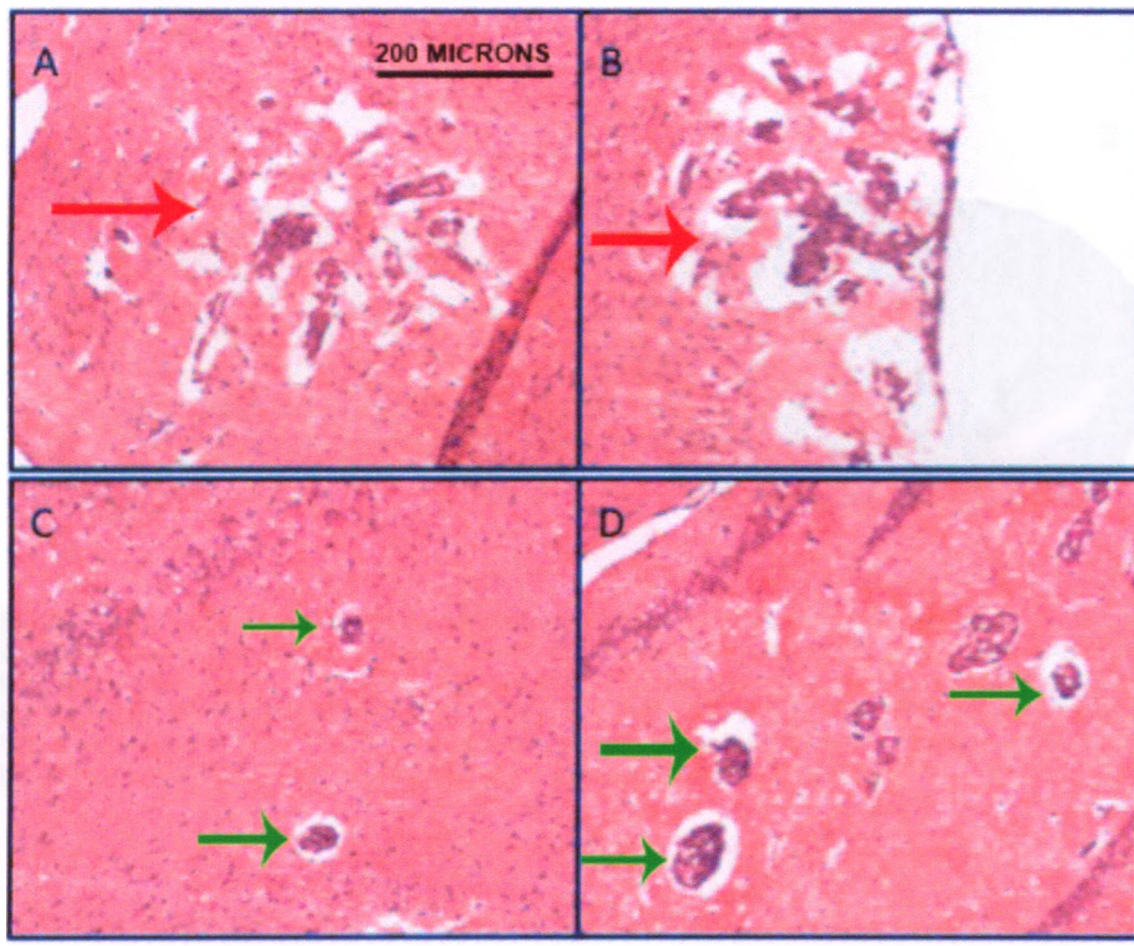

Figure 2.18: Representative H&E stained sections of the mouse brain showing different tumor morphologies present. A and B 'large' metastasis. C and D micro-metastasis. The red arrows point to macro-metastases and the green arrows indicate micro-metastases.

Figure 2.19 displays metastases in a 10 micron thick H&E stained brain section and the complementary 200 micron thick MR image slice. These slices are at in the cortex brain region. Three metastases are outlined. The metastasis outlined in pink had an area of 0.715mm^2 measured from the 2D histological section and a volume of .121mm^3 measured from the 3D image slice. The metastasis outlined in blue had an area of 1.178mm^2 measured from the histology section and a volume of .337mm^3 measured from the image data.

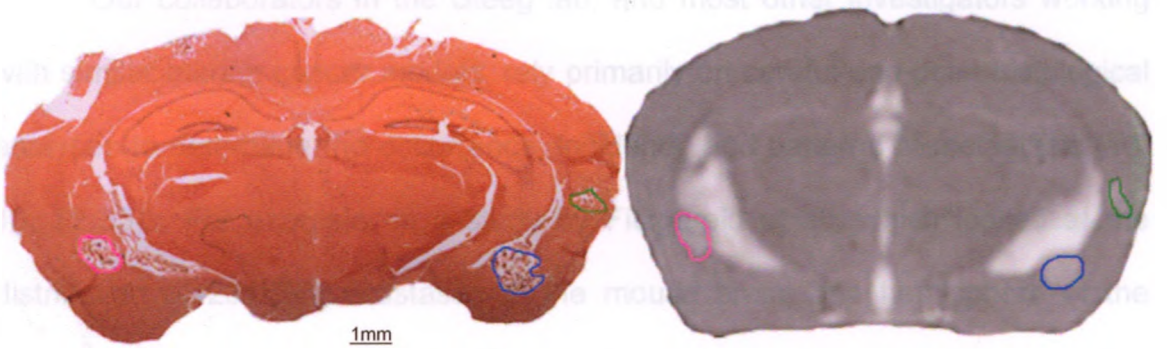

Figure 2.19: Comparison of a histology section containing metastases with its complimentary MRI image. Three different metastases are outlined in pink, green or blue on both histology and MRI. The tumor outlined in pink had a measured area of 0.715mm^2 from the 2D histology and measured volume of .121mm^3 from the 3D image. The tumor outlined in blue had a measured area of 1.178mm^2 and a measured volume of .337mm^3. The tumor outlined in green had a measured area of .441mm^2 and a measured volume of .085mm^3.

2.4 DISCUSSION

The main goal of this study was to perform an in vivo serial MRI investigation of the spatial and temporal aspects of breast cancer metastasis to the brain. Our murine experimental model utilizes two human breast cancer cell lines injected into nude mice. The parental cell line, known as MDA-MB-231, was originally isolated from a pleural effusion (35). Two modified versions of this cell line have been used in this thesis: (i) a derivative line, the MDA-MB-231-BR (231BR) cell line which was developed by in vivo passage to select highly brain metastatic cells (34) and (ii) a subclone, the MDA-MB-231-BR/Her2 (231BR-Her2) cell line, which are 231BR cells transfected with Her2 (33).

Our collaborators in the Steeg lab, and most other investigators working with similar murine cancer models, rely primarily on careful end-point histological analyses to determine the occurrence, incidence and patterns of metastasis (13, 16, 32-33). For example, in a study by Fitzgerald et al., which looked at the distribution of 231BR metastases in the mouse brain, one hemisphere of the brain was interrogated by cutting 10 serial sagittal sections, each 5-10 μm thick, every 300 μm (32). The locations of clusters of metastatic growth were identified by bright-field observation using a 5x objective lens. This technique has several limitations: (1) It is invasive, therefore analysis can only be done at the endpoint of the study where the animal would have to be sacrificed, (2) Analysis cannot be done for the whole brain, the analysis is limited to small sections of the brain and (3) the tissue becomes distorted when the chemicals are added, this affects the anatomical appearance of the tissue and may lead to a false analysis of the data.

Compared to histological analysis, MRI provides a more rapid and complete accounting of cell and tumor burden, and permits repeated sampling of individual mice over long periods of time. With MRI we were able to image entire brain volumes in vivo with scan times of approximately one hour per animal, in contrast to the many hours required for histological assessment of cell and tumor distribution of just a portion of a mouse brain, and only at a single time point. The reality is that histology provides only a snapshot, of a subset of tissue.

In this study the first step for analysis of the image data was to manually count the number of metastases in the whole brain, at each image timepoint, for all mice. Since the image data was acquired in 3D the whole brain could be interrogated. This involved counting a total of 2888 metastases (Table 2). There was no statistically significant difference in the mean number of metastases for mice in Groups 1 and 2, which received 175, 000 231-BR/Her2 and 231BR cells, respectively. At the endpoint the average tumor count for mice injected with 231BR cells was 123 and the average tumor count for mice injected with 231BR/HER2 cells was 113. This agreed with the results of a similar study by Palmieri et al. (33) where a histological analysis of H&E stained brain sections also showed no difference in the numbers of metastases that formed at endpoint after cardiac injection of 231BR or 231BR/Her2 cells.

The next step in the image analysis was to measure the volumes of the individual metastases, at each timepoint, for all mice. The mean tumor volume was larger for mice in Group 1 that received 175,000 231BR/HER2 cells, compared to mice in Group 2 that received 175,000 231BR cells. This was true at all four imaging timepoints. At the endpoint the mean volume of the

metastases in Group 1 mice was 0.165 ± 0.015 mm^3, while the mean volume of the metastases in Group 2 mice was 0.091 ± 0.012 mm^3. Palmieri et al. also looked for differences in the size of the metastases for the two cell lines. Metastases were classified as either "small" (< 50 $microns^2$) or "large" (> 50 $microns^2$) using a 16 mm^2 ocular grid. A classification approach was taken because it is very difficult to measure the actual size of these metastases from a histological section due to the fact that the majority of metastatic growth manifests as clusters of small numbers of cells (Figure 2.16), or micrometastases, and the precise boundaries of an individual metastasis are hard to determine. They found that the 231BR/Her2 cells formed 3 times as many "large" metastases compared with the 231BR cells. This trend for larger metastases with 231BR/Her2 cells, observed in both studies, is consistent with the high rate of clinical detection of brain metastases in patients with Her-2–amplified tumors (5-8).

While the results of these two studies cannot be compared directly, because different numbers of cells were injected (175,000 versus 250,000), and because the analysis is obviously quite different, it is interesting that the same general conclusions were arrived at. The fact that the mean number metastases was not statistically different between 231BR and 231BR/Her2 cells, in either study, suggests that the two different cell lines arrested in the brain and formed metastases with equal efficiency.

The major difference in the conclusions about the number and size of metastases was related to differences in the ability to detect and measure small versus large metastases. In the Palmieri paper the large majority of the

metastases that they counted in H&E stained brain sections were considered to be "small" metastases (>90%) (33). This is because when looking at the brain tissue under the microscope discrete cell clusters can be identified and these are counted individually. In the MR images these separate cell clusters create one larger mass that appears as a hyperintense region in the image. The fluid filled spaces in tumors cause them to appear hyperintense in T2 weighted MRI images, whereas histology cannot determine whether or not the tumors are fluid filled, the different appearance of tumors between these two types of analysis is likely attributed to this property. The smallest measured metastasis had a volume of 0.005 mm^3; the reproducibility of this measurement can be called into question since the volume measurement of tumors is largely dependant on the user. For example the border of the tumor in general had the lowest tumor signal intensity and defining its borders may vary from user to user. As a result the true tumor volume may be called into question but when comparing tumor volumes from different cell lines and regions it is important for the user to remain consistent.

One of the interesting findings to come from our analysis of tumor volumes in the whole brain was that in mice where fewer metastases developed the volume of the metastases was larger. We compared the endpoint metastases of mice injected with 175,000 231BR/HER2 cells (Group 1) and mice injected with 50,000 231BR/HER2 cells (Group 3). The mice injected with 50,000 cells developed fewer metastases (mean of 18 versus 113) but they were on average significantly larger than the metastases that formed when 175,000 cells were injected. This was also observed when all metastases from Groups 1 and 2 were

assessed. Mice in Groups 1 and 2 were classed as having fewer or greater than 50 metastases at endpoint. The tumor volume was significantly larger in mice with fewer than 50 metastases, compared to those with greater than 50 metastases. This result suggests that metastatic growth may be influenced by the availability of resources in the brain microenvironment. This observation raises new questions in regards to the nature of metastatic growth, namely: (i) what role and to which degree does signaling between the tumor cell(s) and brain microenvironment play? (ii) does signaling between neighboring tumor cell(s) affect the rate of metabolism? (iii) is the consumption of resources amongst neighboring tumors competitive or symbiotic?

Histological analyses only provide data for one timepoint. The longitudinal nature of MRI allowed us to follow the progress of metastasis formation over time within a single animal. By monitoring metastasis development over time and measuring the volume of individual metastases at each timepoint is the ability to generate tumor growth curves (Figures 2.10&2.11 and Appendix 1). Our growth rate analysis showed that most metastases exhibit exponential growth with the greatest growth occurring between days 26 and 29.

The 3D high-resolution bSSFP images permitted the whole brain to be studied, and allowed for visualization of metastases in all three orientations (Figure 2.4) something that would be practically impossible using conventional histological techniques. The 3D MR image data allowed us to assess the distribution of metastases in the whole brain and within specific brain regions. Metastases were found in all regions of the brain. However, the distribution of metastases conformed to a pattern. The majority of metastases formed in the

cortex of the brain. Regardless of cell line, more than 50% of the metastases were located in the cortex in all mice. The central brain region contained the next largest proportion of metastases, followed by the posterior and olfactory brain regions. Many metastases formed along grey-white matter junctions and in all regions of the brain metastases appeared near ventricles.

Song et al. (23) have recently investigated tumor formation by MRI in a nude rat model of 231BR brain metastasis and showed that 100% of mice had MRI visible metastases in the cerebral cortex, but only 55% of mice had metastases detected in images of the olfactory bulb and cerebellum. Fitzgerald et al. assessed H&E sections of brain tissue from mice injected with 175,000 231BR cells and also reported a non-random distribution (32). They found that 100% of mice had metastases in the frontal region of the cortex, 95% of mice had metastases in the parietal/temporal cortex and 90% of mice had metastases in the hippocampus and medulla oblongata. Fewer metastases were found in the ventral portions of the brain. It should be noted that in these two studies the proportion of mice that developed metastases in certain brain regions was reported, whereas this study determined the numbers of metastases and the relative distribution of metastases amongst brain regions.

In this thesis we began to ask why these differences in spatial distribution of metastases exist. We measured the volumes of the brain regions to determine if more metastases were counted in the cortex because the cortex was the largest brain region. This indicated that the volume of the brain region is not likely the major determinant of the incidence of metastases. The volumes of the cortex

and the central brain regions, for example, are nearly equal despite large differences in the numbers of metastases.

Next we asked whether differences in the spatial distribution of metastases were related to the initial arrest of cancer cells in the brain. Cells were labeled with iron oxide nanoparticles to allow their detection by MRI. Iron labeling did not affect cell viability, as indicated by the trypan blue exclusion assay and flow cytometric analyses of apoptosis and necrosis. Iron labeled cells appeared as discrete regions of signal hypointensity in brain images acquired on day 1 after the cell injection. As cells proliferated and metastases developed the iron label was diluted and most of the individual cells were no longer detectable.

The ability to detect iron labeled cancer cells with MRI allowed us to quantify initial numbers of cells that arrested in the mouse brain and visualize the distribution of these cells throughout the whole, intact organ, which is not possible with other in vivo imaging techniques. One group of mice (Group 4) was imaged on day 1 post injection and then on day 35 post injection and these two image sets were compared (Figure 2.8). The void volume in each brain region was determined and the spatial distribution of the signal voids on day 1 was compared with the spatial distribution of the brain metastases observed at endpoint. The distribution of signal voids on day 1 was similar to the distribution of metastases on day 35; the greatest percentages of both voids and tumors were observed in the cortex, followed by the central brain, and then the posterior and olfactory brain regions.

On day 1, 51% of the voids were located in the cortex and on day 35, 54% of the metastases were located in the cortex. This suggests that the number of metastases that develop in a brain region depends on the numbers of arresting cells. The fact that the cortex has the highest percentage of voids on day 1 might be explained by the fact that the cortex has the highest number of gray/white matter junctions (36). Furthermore, the cardiac output is highest in this region, cells arrive in the brain via the C7 branch of the internal carotid artery, from there some of the cells travel through the bifurcations: posterior communicating artery, anterior choroidal artery and the anterior cerebral artery but the majority of cells will travel through the middle cerebral artery which does not bifurcate from the internal carotid. The output is highest in middle cerebral artery and it supplies oxygenated blood to the frontal lobe, parietal lobe and temporal lobe. These regions mostly correspond to the cortex in this study, and this likely indicates why the majority of cells arrest in this region (47).

The percentage of metastases in the posterior and olfactory brain regions on day 35 was less than the percentage of voids on day 1. While 16% of the voids observed on day 1 were located in the posterior brain region, only 10% of the brain metastases were located in the posterior brain on day 35. Similarly, 6% of the voids observed on day 1 were located in the olfactory region and only 2% of the metastases observed on day 35 were located in the olfactory region. This suggests that for the posterior and olfactory brain regions a smaller proportion of the cells that were arrested there on day 1 went on to form metastases. It could be that not as many cells that arrest in the posterior and olfactory regions survive,

or that cells arresting in these regions are not exposed to the same growth stimuli as cells in the cortex and central brain regions.

For Groups 1-3 cancer cells were also iron labeled. In these mice this was done so that images could be acquired on day 0 or day 1 after injection to assess the success of the intracardiac injection. It is important to point out that this injection technique is challenging and that 100% success with these injections is not common. There is some variability in the size and position of the heart in the nude mice, which contributes to the ability to accurately target the left ventricle. The skill of the technician is also very important. In this study one trained technician performed all of the injections (CS). The cells must be deposited into the left ventricle of the beating heart for delivery of the cells to the brain and the rest of the body. If the cells are injected into the right ventricle by accident then they will first flow through the lungs and the majority will be trapped there in the capillaries. If the cells are injected into the heart tissue itself then tumors develop on the heart muscle. While the use of MRI may seem an expensive way to evaluate the success of an injection in the long run it saves time and money because only those mice, which have received "good" injections, are imaged serially for the month after the cell injection.

In vivo imaging modalities have helped with the current understanding of metastasis. Each modality has strengths for studying the steps in the metastatic process, but each is also limited by technical constraints. Although optical techniques, such as bioluminescence (BLI), are sensitive to small numbers of cells they are limited by the penetration of light through optically opaque tissues,

and are also limited by spatial resolution, even in mice (37, 38). With surgical exposure, optical microscopic methodologies, such as intravital video microscopy (IVVM), can achieve single-cell detection (39, 40); however, the small FOVs of this technique only allow examination of a small fraction of the overall target organ, and single animals can be followed only for short periods of time (e.g., hours) unless specialized window chambers are used (41, 42). CT can produce images of the entire mouse anatomy at high spatial resolution, however, it has poor soft-tissue contrast and there are currently no CT contrast agents that allow for the tracking of cells in vivo. High-frequency ultrasound can produce images of high spatial and temporal resolution, but the detection of tumors by US is limited by the penetration of high-frequency sound waves in tissue and by bone/air–tissue interfaces (43). PET and SPECT are high-sensitivity imaging techniques that are capable of detecting small numbers of cells (44-46) (hundreds of cells) throughout the entire organism. However, the spatial resolution of PET and SPECT is quite low, which makes it difficult to differentiate small groups of cells within target organs, and impossible to detect single cells. In this thesis we demonstrate how MRI can be used to study the process of cancer metastasis with high spatial resolution, good soft-tissue contrast, and single-cell sensitivity, with the ability to image an entire organ or animal longitudinally over time.

2.5 References

1. Weil RJ, Palmieri DC, Bronder JL, Stark AM, Steeg PS. Breast cancer metastasis to the central nervous system. Am J Pathol 2005;167(4):913-20.

2. Lin NU, Bellon JR, Winer EP. CNS metastases in breast cancer. J Clin Oncol 2004;22(17):3608-17.

3. DiStefano A, Yong Yap Y, Hortobagyi GN, Blumenschein GR. The natural history of breast cancer patients with brain metastases. Cancer 1979;44(5):1913-8.

4. Kamar FG, Posner JB. Brain metastases. Semin Neurol 2010;30(3):217-35.

5. Bendell JC, Domchek SM, Burstein HJ. Central nervous system metastases in women who receive trastuzumab-based therapy for metastatic breast carcinoma. Cancer 2003;97(12):2972-7.

6. Pestalozzi BC, Zahrieh D, Price KN. Identifying breast cancer patients at risk for central nervous system (CNS) metastases in trials of the international breast cancer study group (IBCSG). Ann Oncol 2006;17(6):935-44.

7. Church DN, Modgil R, Guglani S. Extended survival in women with brain metastases from HER2 overexpressing breast cancer. Am J Clin Oncol 2008;31(3):250-4.

8. Stemmler HJ, Kahlert S, Siekiera W, Untch M, Heinrich B, Heinemann V. Characteristics of patients with brain metastases receiving trastuzumab for HER2 overexpressing metastatic breast cancer. Breast 2006;15(2):219-25.

9. Baculi RH, Suki S, Nisbett J, Leeds N, Groves M. Meningeal carcinomatosis from breast carcinoma responsive to trastuzumab. J Clin Oncol 2001;19(13):3297-8.

10. Yoneda T, Williams PJ, Hiraga T, Niewolna M, Nishimura R. A bone-seeking clone exhibits different biological properties from the MDA-MB-231 parental human breast cancer cells and a brain-seeking clone in vivo and in vitro. J Bone Miner Res 2001;16(8):1486-95.

11. Chen EI, Hewel J, Krueger JS. Adaptation of energy metabolism in breast cancer brain metastases. Cancer Res 2007;67(4):1472-86.

12. Kim LS, Huang S, Lu W, Lev DC, Price JE. Vascular endothelial growth factor expression promotes the growth of breast cancer brain metastases in nude mice. Clin Exp Metastasis 2004;21(2):107-18.

13. Palmieri D, Lockman PR, Thomas FC. Vorinostat inhibits brain metastatic colonization in a model of triple-negative breast cancer and induces DNA double-strand breaks. Clin Cancer Res 2009;15(19):6148-57.

14. Tsai MS, Shamon-Taylor LA, Mehmi I, Tang CK, Lupu R. Blockage of heregulin expression inhibits tumorigenicity and metastasis of breast cancer. Oncogene 2003;22(5):761-8.

15. Yano S, Shinohara H, Herbst RS. Expression of vascular endothelial growth factor is necessary but not sufficient for production and growth of brain metastasis. Cancer Res 2000;60(17):4959-67.

16. Thomas FC, Taskar K, Rudraraju V. Uptake of ANG1005, a novel paclitaxel derivative, through the blood-brain barrier into brain and experimental brain metastases of breast cancer. Pharm Res 2009;26(11):2486-94.

17. Lunt SJ, Cawthorne C, Ali M, et al. The hypoxia-selective cytotoxin NLCQ-1 (NSC 709257) controls metastatic disease when used as an adjuvant to radiotherapy. Br J Cancer 2010.

18. Ford NL, Martin EL, Lewis JF, Veldhuizen RA, Holdsworth DW, Drangova M. Quantifying lung morphology with respiratory-gated micro-CT in a murine model of emphysema. Phys Med Biol 2009;54(7):2121-30.

19. Ferretti S, Allegrini PR, O'Reilly T. Patupilone induced vascular disruption in orthotopic rodent tumor models detected by magnetic resonance imaging and interstitial fluid pressure. Clin Cancer Res 2005;11(21):7773-84.

20. Ben-Hur T, van Heeswijk RB, Einstein O. Serial in vivo MR tracking of magnetically labeled neural spheres transplanted in chronic EAE mice. Magn Reson Med 2007;57(1):164-71.

21. Kedziorek DA, Muja N, Walczak P. Gene expression profiling reveals early cellular responses to intracellular magnetic labeling with superparamagnetic iron oxide nanoparticles. Magn Reson Med 2010;63(4):1031-43.

22. Townson JL, Ramadan SS, Simedrea C. Three-dimensional imaging and quantification of both solitary cells and metastases in whole mouse liver by magnetic resonance imaging. Cancer Res 2009;69(21):8326-31.

23. Song HT, Jordan EK, Lewis BK. Rat model of metastatic breast cancer monitored by MRI at 3 tesla and bioluminescence imaging with histological correlation. J Transl Med 2009;7:88.

24. Wang J, Xie J, Zhou X, et al. Ferritin enhances SPIO tracking of C6 rat glioma cells by MRI. Mol Imaging Biol 2010.

25. Serkova NJ, Renner B, Larsen BA. Renal inflammation: Targeted iron oxide nanoparticles for molecular MR imaging in mice. Radiology 2010;255(2):517-26.

26. Heyn C, Ronald JA, Ramadan SS. In vivo MRI of cancer cell fate at the single-cell level in a mouse model of breast cancer metastasis to the brain. Magn Reson Med 2006;56(5):1001-10.

27. Arbab AS, Janic B, Haller J, Pawelczyk E, Liu W, Frank JA. In vivo cellular imaging for translational medical research. Curr Med Imaging Rev 2009;5(1):19-38.

28. Arbab AS, Janic B, Jafari-Khouzani K. Differentiation of glioma and radiation injury in rats using in vitro produce magnetically labeled cytotoxic T-cells and MRI. PLoS One 2010;5(2):e9365.

29. Nohroudi K, Arnhold S, Berhorn T, Addicks K, Hoehn M, Himmelreich U. In vivo MRI stem cell tracking requires balancing of detection limit and cell viability. Cell Transplant 2010;19(4):431-41

30. Smirnov P, Poirier-Quinot M, Wilhelm C. In vivo single cell detection of tumor-infiltrating lymphocytes with a clinical 1.5 tesla MRI system. Magn Reson Med 2008;60(6):1292-7.

31. Shapiro EM, Sharer K, Skrtic S, Koretsky AP. In vivo detection of single cells by MRI. Magn Reson Med 2006;55(2):242-9.

32. Fitzgerald DP, Palmieri D, Hua E. Reactive glia are recruited by highly proliferative brain metastases of breast cancer and promote tumor cell colonization. Clin Exp Metastasis 2008;25(7):799-810.

33. Palmieri D, Bronder JL, Herring JM. Her-2 overexpression increases the metastatic outgrowth of breast cancer cells in the brain. Cancer Res 2007;67(9):4190-8.

34. Yoneda T, Williams PJ, Hiraga T, Niewolna M, Nishimura R. A bone-seeking clone exhibits different biological properties from the MDA-MB-231 parental human breast cancer cells and a brain-seeking clone in vivo and in vitro. J Bone Miner Res 2001;16(8):1486-95.

35. Cailleau RM, Young R, Olive M, Reeves WJ Jr 1974 Breast tumor cell lines from pleural effusions. J Natl Cancer Inst 53:661–674.

36. Hwang TL, Close TP, Grego JM, Brannon WL, Gonzales F. Predilection of brain metastasis in gray and white matter junction and vascular border zones. Cancer 1996;77(8):1551-5.

37. Cirstoiu-Hapca A, Buchegger F, Lange N, Bossy L, Gurny R, Delie F. Benefit of anti-HER2-coated paclitaxel-loaded immuno-nanoparticles in the treatment of disseminated ovarian cancer: Therapeutic efficacy and biodistribution in mice. J Control Release 2010;144(3):324-31.

38. Pendharkar AV, Chua JY, Andres RH. Biodistribution of neural stem cells after intravascular therapy for hypoxic-ischemia. Stroke 2010.

39. Ito S, Nakanishi H, Ikehara Y. Real-time observation of micrometastasis formation in the living mouse liver using a green fluorescent protein gene-tagged rat tongue carcinoma cell line. Int J Cancer 2001;93(2):212-7.

40. Scher RL. Role of nitric oxide in the development of distant metastasis from squamous cell carcinoma. Laryngoscope 2007;117(2):199-209.

41. Gaustad JV, Brurberg KG, Simonsen TG, Mollatt CS, Rofstad EK. Tumor vascularity assessed by magnetic resonance imaging and intravital microscopy imaging. Neoplasia 2008;10(4):354-62.

42. Vajkoczy P, Goldbrunner R, Farhadi M. Glioma cell migration is associated with glioma-induced angiogenesis in vivo. Int J Dev Neurosci 1999;17(5-6):557-63.

43. Boyd NF, Martin LJ, Bronskill M, Yaffe MJ, Duric N, Minkin S. Breast tissue composition and susceptibility to breast cancer. J Natl Cancer Inst 2010.

44. Ben-Haim S, Israel O. Breast cancer: Role of SPECT and PET in imaging bone metastases. Semin Nucl Med 2009;39(6):408-15.

45. Boretius S, Kasper L, Tammer R, Michaelis T, Frahm J. MRI of cellular layers in mouse brain in vivo. Neuroimage 2009;47(4):1252-60.

46. Terrovitis J, Kwok KF, Lautamaki R. Ectopic expression of the sodium-iodide symporter enables imaging of transplanted cardiac stem cells in vivo by single-photon emission computed tomography or positron emission tomography. J Am Coll Cardiol 2008;52(20):1652-60.

47. Moore KL, Dalley AR. Clinically Oriented Anatomy, 4th Edition, Lippincott Willams & Wilkins, Toronto. 1999.

Chapter 3: Characterizing Breast Cancer Metastasis to the Brain.

DISCUSSION

In this thesis, we investigated breast cancer metastasis to the brain using Cellular MRI. The Steeg model of breast cancer metastasis to the brain has been used to evaluate the response of drugs developed to treat brain metastases, identify gliosis at the onset of metastasis, examine tumor distribution patterns and evaluate the metastatic potential of various cell lines (1-4). In all of these studies they have used histology but its limited sampling of the brain serves as an estimate for what is occurring throughout the whole brain. Furthermore its use can only be applied at the endpoints of studies. By using MRI we were able to corroborate several of their findings and also give new insight into the nature of metastasis since MRI is able to investigate the whole brain non-invasively.

3.1 Clinical Similarities

We showed that metastases formation was highest in the cortex of the brain at the time of first detection to the endpoint of the study using both the MDA-MB-231BR and MDA-MB-231BR/HER2 cell lines. Our findings were consistent with both Fitzgerald et al. (3) and Song et al. (5) and also several post-mortem clinical studies (6, 8). In 1988, Posner and Delattre investigated the

distribution of metastases of 288 patients that were reported to have had brain metastases from various types of primary cancers (6). They analyzed CT scans of these patients that were done between January 1979 and October 1985. They found that single and multiple metastases were most often located in hemispheric brain regions which could be identified as the cortex region in our mouse model.

This was true for various primary cancer sites, however, brain metastases that had originated from a primary tumor that was pelvic or gastrointestinal had an overrepresentation in the posterior fossa 53% (posterior region in mouse model) compared to the rest of the brain. Fewer than 10% of metastases formed in this region for primary tumors that weren't pelvic or gastrointestinal, this was consistent with our data where fewer than 10% of metastases formed in the posterior region of the brain. These findings are also consistent with Stephen Paget's "seed and soil" hypothesis (7), where certain sites are predisposed to certain types of secondary tumors. This finding indicates that the brain microenvironment in the posterior region or "posterior fossa" interacts differently with metastatic pelvic cancer cells than others.

Hwang and colleagues also found metastasis formation was highest in frontal and parietal regions (cortex of mouse brain) but metastases formation was predisposed to these regions due to the large amount of gray and white matter junctions (8). They found that over 64% of metastases formed in close proximity to gray-white matter junctions, 11.4% in gray matter, 15.7% in white matter and 8.6% uncertain. According to Hwang tumor emboli are predisposed to form in these regions primarily due to mechanical factors. Experimental evidence has suggested that clusters of cells are necessary for the formation of tumor emboli

(9) and they measure roughly between 100 and 200 μm, whereas arterioles that supply that supply gray white matter junctions are roughly between 50 and 150 μm; altogether size restriction leads to the arrest of metastatic cells in these regions.

In our study we did not evaluate the distribution of gray and white matter junctions in the mouse brain but we did correlate the distribution of cells in the brain regions at day 1 to the distribution of metastases at the final endpoint. We found that 50% of the voids on day were found in the cortex on day 1 and 53% of metastases were located in this region at the day 35 endpoint. Also, we showed that 27% of voids arrested in the central brain on day 1 and by day 35, 34% of metastases were in this region. One of the setbacks of visualizing metastases in the mouse brain using a b-SSFP pulse sequence is the reduced gray-white matter contrast and we did not evaluate the portion of gray-white matter junctions in these areas. However like Hwang and colleagues we showed that brain metastases are predisposed to certain areas. A follow up study using an MRI pulse sequence that provides superior gray white matter contrast in brain regions may allow us to measure the proportion of gray-white matter junctions in the various brain regions of our mouse model described in this study.

The finding from our study does indeed support the notion that metastasis formation is largely dependant on hemodynamic processes but it is not mutually exclusive from the "seed and soil" hypothesis. Metastasis has been described as an inefficient process (10) and cells go on to "seed" or proliferate only when they reach the appropriate "soil" or microenvironment. This is true in this study considering over 175 000 cells were injected into each mice but only a very small

fraction of those cells formed metastases and only in the brain. Also, 16% of voids were found in the posterior region on day 1 but only 10% of metastases were found here by day 35. This indicates that the "soil" or microenvironment in the posterior region is not as hospitable as the cortex.

3.2 Limitations of the study

In previous sections we emphasized the limitations of histology in comparison to MRI. While MRI does allow us to visualize the whole brain non-invasively and track metastatic cancer cell, it does not give us information about cell viability, heterogeneous cell populations in tumors or changes in the brain brain microenvironment. The relationship between histology and MRI is not competitive but rather should be considered collaborative. In this study MRI validated the findings of the Steeg lab: i.) no difference in the number of metastases formed between mice injected with 231BR and 231BR/HER2 cells and ii.) Metastases that were the progeny of 231BR/HER2 cells were larger. In a similar scenario, when performing cell tracking studies MRI requires the use of histology or to validate cell viability when we are detecting what is perceived to be viable metastatic cell populations. Future histological studies may closely examine the brain microenvironment in the cortex since metastases had a propensity to form there.

Furthermore, the resolution of MRI in this study was 100 microns in plane, although we detected over 100 metastases in some mice many metastases would be undetected on account of the limited resolution, whereas the histological analysis done by the Steeg lab had a 50 micron resolution and they

detected over 200 metastases despite the limited sampling. In spite of this the detection capabilities of MRI are constantly improving and has the potential to resolve smaller metastases with adequate SNR within a reasonable scan time.

The clinical relevance of the mouse model of breast cancer metastasis to the brain used in this thesis may also be called into question. Well over 100 metastases were detected by the endpoint in most mice. Clinical reports generally indicate that brain metastases are detected as single lesions and when multiple lesions are reported they are generally less than 10 metastases. The high number of metastases found at the endpoint in our model is due to the large number of cells that are injected into the mice. We detected as few as 22 metastases in one mouse injected with 50000 cells. It would be interesting to determine how few cells may need to be injected until an endpoint number of brain metastases that is synonymous with clinical records are detected.

There was significant variability regarding the number of metastases in the brain by the endpoint for both Group 1 and Group 2. Some mice had fewer than 50 metastases present in the brain by the endpoint while others had over 100 tumors. In a similar scenario, there was variability with regards to the number of voids detected on day 1 amongst Group 4 mice. It is highly likely that the number of cells delivered to the brain strongly influences the number of metastases that will develop there by the endpoint.

One possible explanation for this is that cardiac output to the brain affects the delivery of metastatic breast cancer cells to the brain, which in turn affects the number of metastases that form. Those cells that reach the brain travel through the C7 section of the internal carotid artery. It is possible that at the time of

injection the blood flow in this region is much lower than the other arterial branches of the internal carotid artery and those mice that received few cells may have had a lower cardiac output through this artery.

Another likely reason for the variability is that there are not just 'good' and 'bad' injections but there are other things related to the injection technique that may result in the injection and delivery of fewer or greater numbers of cells. For example after cells are injected into the left ventricle of the heart, the blood flows to the aorta which then branches into multiple arteries that deliver oxygenated blood to various organs in the body. Rapid blood flow in neighboring aortic branch arteries relative to carotid artery may influence the delivery of high numbers of cells delivered to the rest of the body relative to the brain.

3.3 The vascularized brain microenvironment and metastases

The role of angiogenesis in the development of brain metastasis has been investigated and debated. A study by Kim and colleagues showed that elevated VEGF expression contributed to the ability of metastatic breast cancer cells to form metastases (11). Conversely, Kusters et al. showed brain metastases from a melanoma lineage did not depend on neo-angiogenesis but instead opted to grow around preexisting blood vessels (12), the brain is a highly vascularized organ. The nature of metastasis is complicated and it is quite possible that both events may have occurred for brain metastases detected in our model, regardless of the type of cells injected. The ability to visualize the vasculature within and around metastases throughout the whole brain would

shed light on this debate and reveal if one event is more common than the other. We did not examine the vasculature in the mouse brain with MRI in this thesis.

However other imaging modalities such as micro-CT have the potential to resolve this issue. In CT visualization of the brain vasculature in mice is dependant on the contrast agent that is administered intracardially, it increases the attenuation coefficient of the blood vessels relative to the brain parenchyma. One group administered a radio opaque silicone contrast agent to a mouse and performed a micro-CT scan of the brain (13). They found that 71% of the Circle of Willis and its branch anatomy could be visualized. After MRI imaging at the endpoint of a study, mice could be perfused with a similar silicone based contrast agent and this CT technique could be applied to mice with brain metastases. The resulting CT images could then be registered to the MRI images to visualize the vasculature within and around the brain metastases throughout the whole brain. It should be noted that this technique is performed at the endpoint of the study and does not allow us to visualize the development of the vasculature within and around metastases at varying time points.

JuanYin and colleagues developed a technique to measure cerebral blood volume within and around metastases using cellular MRI (14); they injected mice intravenously with USPIO nanoparticles and T2* imaging allowed them to determine that cerebral blood volume was higher within and around metastases in the brain. This technique indicated that some metastases were vascularized but the blooming artifact from the USPIO masked the vasculature and the amount of degree of vascularization within and around the metastases could not be determined.

3.4 Evaluating Treatments

One of the major constraints for treating brain metastases with drugs is getting passage across the blood brain barrier (BBB); such is the case with trastuzumab (18). Drugs such as paclitaxil, lapatinib and cedinirab have been developed which are capable of crossing the BBB and targeting brain metastases (14-16). Tumor response to these drugs has most often been measured with histology in preclinical studies. As before the limited sampling and inability to non invasively image the brain limited the amount of information that could be obtained when treating brain metastases. In Chapter 2 we constructed growth curves of brain metastases using volume data measured from serial MRI. This technique for monitoring tumor growth could also be used to monitor tumor response to various treatments. Noninvasive imaging of brain metastases would allow us to measure early response to treatment at various doses. Similarly it may be applied to measure tumor response to radiation treatment as well.

3.5 Final Word

Brain metastasis is a fatal secondary complication of breast cancer. The one year patient survival rate is less than 20% (19), for the patient and his/her family this is emotional and physical burden. Even when the patient appears to live a disease-free survival after combating the primary disease, recurrent brain metastases may appear years later. Treatment for patients with brain metastases is at best palliative.

Progress has been made in understanding the complicated nature of brain metastasis through preclinical mouse models. They are the basis for assessing novel clinical treatments and for understanding changes in the brain microenvironment at the onset of metastasis. Cellular MRI allows us to visualize the development of brain metastases from its early single cell stages to forming a proliferative mass. Furthermore it is more than just a snapshot of a section of the brain and tumor, we are visualizing the entire brain in 3D. We have shown that the distribution of brain metastases is not random and that some brain regions are more predisposed to metastasis formation than others. Also, we have shown MRI is effective at measuring the metastatic potential of different cell lines.

In spite of the progress of brain metastasis research, the window of hope for patients diagnosed with brain metastases is very small. Much more progressive research will be required if we are to ever beat the disease. Communication about new findings and ideas regarding brain metastasis between scientists of various scientific backgrounds will connect more pieces to the brain metastasis puzzle. Emphasis of the severity of brain metastasis will inspire new generations of scientists to dedicate themselves to the eradication of the disease. As long as there is a will, drive and determination amongst scientists investigating brain metastasis, hope will grow for women and men fighting the disease.

3.6 References

1. Palmieri D, Lockman PR, Thomas FC, et al. Vorinostat inhibits brain metastatic colonization in a model of triple-negative breast cancer and induces DNA double-strand breaks. Clin Cancer Res 2009;15(19):6148-57.

2. Thomas FC, Taskar K, Rudraraju V, et al. Uptake of ANG1005, a novel paclitaxel derivative, through the blood-brain barrier into brain and experimental brain metastases of breast cancer. Pharm Res 2009;26(11):2486-94.

3. Fitzgerald DP, Palmieri D, Hua E, et al. Reactive glia are recruited by highly proliferative brain metastases of breast cancer and promote tumor cell colonization. Clin Exp Metastasis 2008;25(7):799-810.

4. Palmieri D, Bronder JL, Herring JM, et al. Her-2 overexpression increases the metastatic outgrowth of breast cancer cells in the brain. Cancer Res 2007;67(9):4190-8.

5. Song HT, Jordan EK, Lewis BK, et al. Rat model of metastatic breast cancer monitored by MRI at 3 tesla and bioluminescence imaging with histological correlation. J Transl Med 2009;7:88.

6. Delattre JY, Krol G, Thaler HT, Posner JB. Distribution of brain metastases. Arch Neurol 1988;45(7):741-4.

7. Paget S. The distribution of secondary growths in cancer of the breast. The Lancet. 1889;1:99-101.

8. Hwang TL, Close TP, Grego JM, Brannon WL, Gonzales F. Predilection of brain metastasis in gray and white matter junction and vascular border zones. Cancer 1996;77(8):1551-5.

9. WATANABE S. The metastasizability of tumor cells. Cancer 1954;7(2):215-23.

10. Chambers AF, Groom AC, MacDonald IC, Dissemination and growth of cancer cells in metastatic sites. Nat Rev Cancer. 2002 Aug;2(8):563-72.

11. Kim LS, Huang S, Lu W, Lev DC, Price JE. Vascular endothelial growth factor expression promotes the growth of breast cancer brain metastases in nude mice. Clin Exp Metastasis 2004;21(2):107-18.

12. Kusters B, Leenders WP, Wesseling P. Vascular endothelial growth factor-A(165) induces progression of melanoma brain metastases without induction of sprouting angiogenesis. Cancer Res 2002;62(2):341-5.

13. Abruzzo T, Tumialan L, Chaalala C. Microscopic computed tomography imaging of the cerebral circulation in mice: Feasibility and pitfalls. Synapse 2008;62(8):557-65.

14. JuanYin J, Tracy K, Zhang L. Noninvasive imaging of the functional effects of anti-VEGF therapy on tumor cell extravasation and regional blood volume in an experimental brain metastasis model. Clin Exp Metastasis 2009;26(5):403-14.

15. Sutherland S, Ashley S, Miles D, et al. Treatment of HER2-positive metastatic breast cancer with lapatinib and capecitabine in the lapatinib expanded access programme, including efficacy in brain metastases--the UK experience. Br J Cancer 2010;102(6):995-1002.

16. Edelman MJ, Belani CP, Socinski MA, et al. Outcomes associated with brain metastases in a three-arm phase III trial of gemcitabine-containing regimens versus paclitaxel plus carboplatin for advanced non-small cell lung cancer. J Thorac Oncol 2010;5(1):110-6.

17. Weil RJ, Palmieri DC, Bronder JL, Stark AM, Steeg PS. Breast cancer metastasis to the central nervous system. Am J Pathol 2005;167(4):913-20.

18. Baculi RH, Suki S, Nisbett J, Leeds N, Groves M. Meningeal carcinomatosis from breast carcinoma responsive to trastuzumab. J Clin Oncol 2001;19(13):3297-8.

Appendix A

MDA-MB-231BR/HER2 excel growth rate plots (mouse 5)

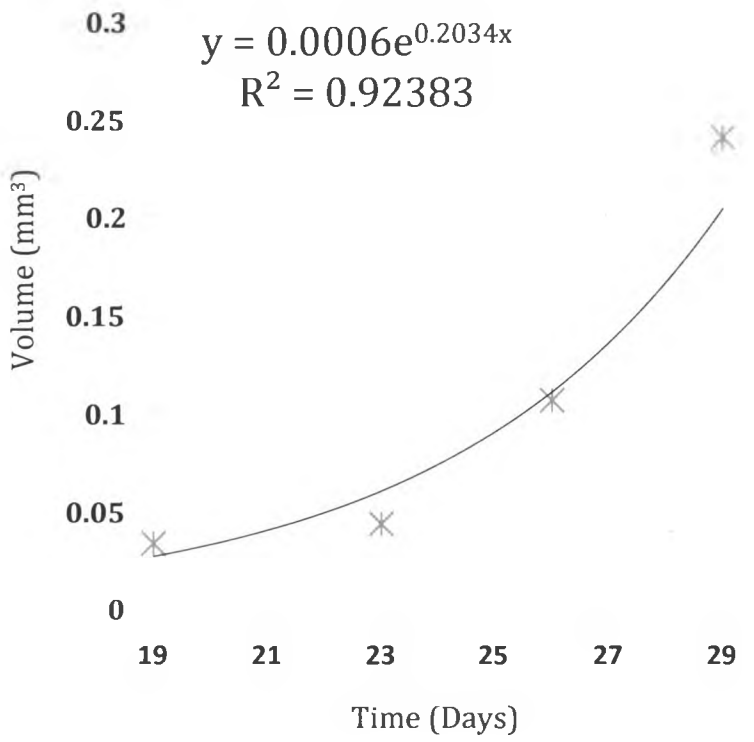

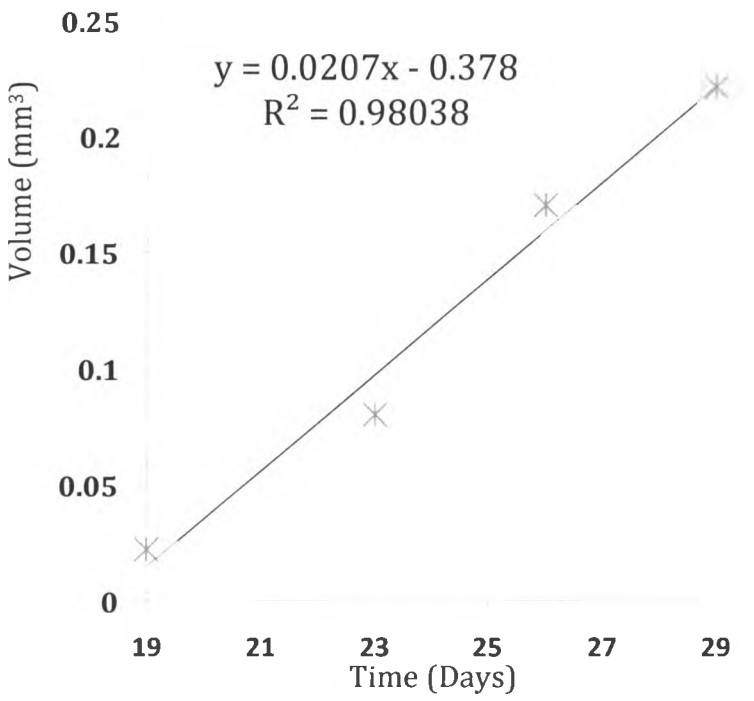

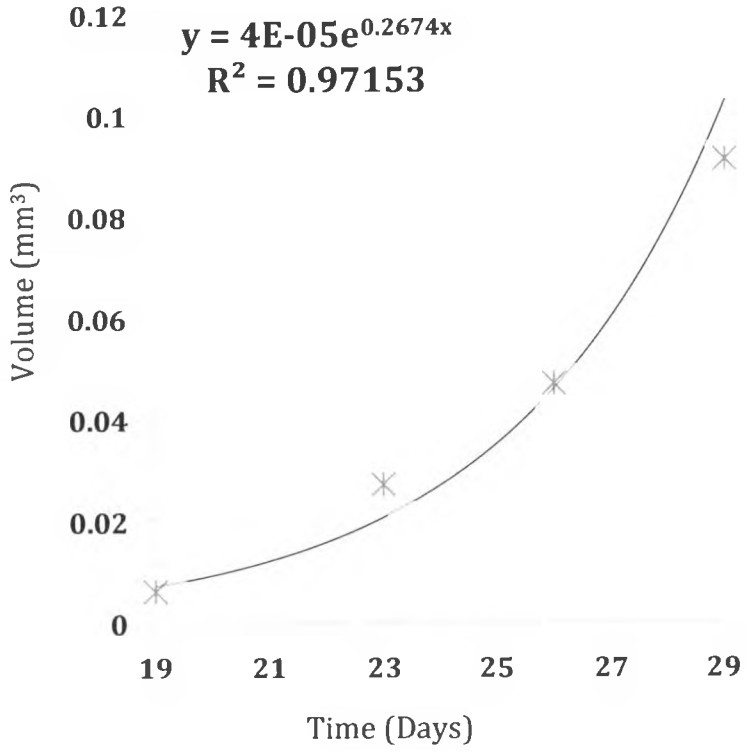
y = 4E-05e^0.2674x
R² = 0.97153
0.12
0.1
0.08
0.06
0.04
0.02
0
Volume (mm³)
19
21
23
25
27
29
Time (Days)

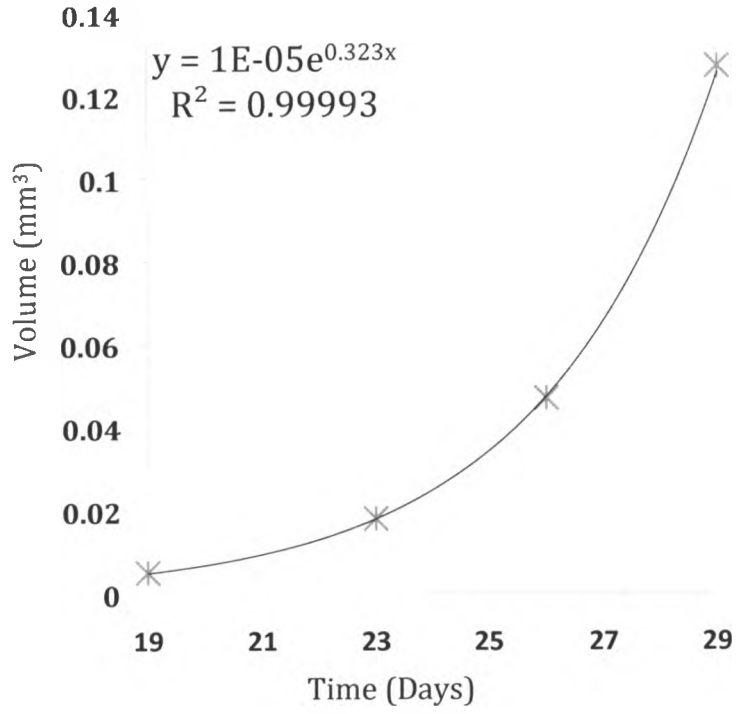
y = 1E-05e^0.323x
R² = 0.99993
0.14
0.12
0.1
0.08
0.06
0.04
0.02
0
Volume (mm³)
19
21
23
25
27
29
Time (Days)

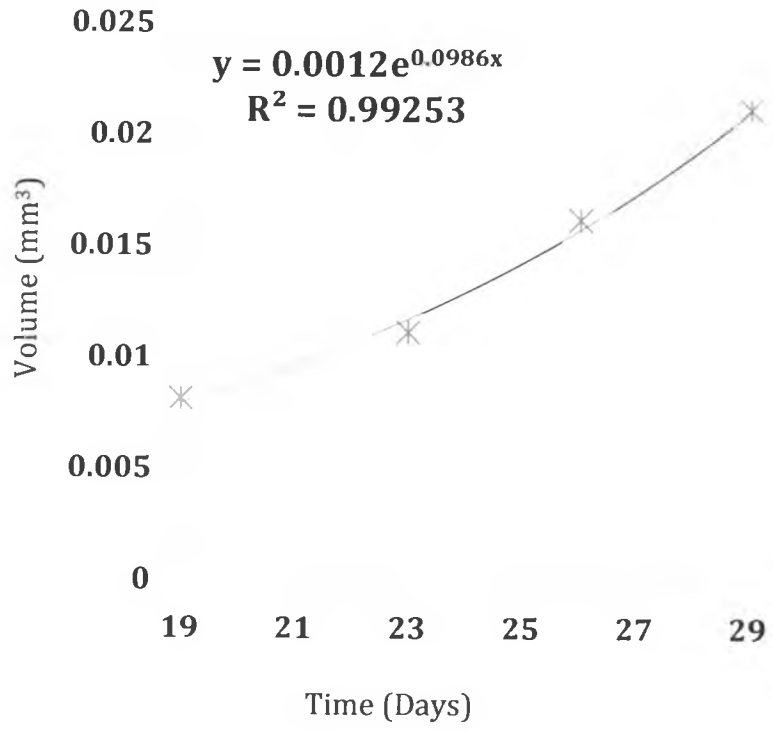
y = 0.0012e^0.0986x
R² = 0.99253
Volume (mm³)
0.025
0.02
0.015
0.01
0.005
0
19
21
23
25
27
29
Time (Days)

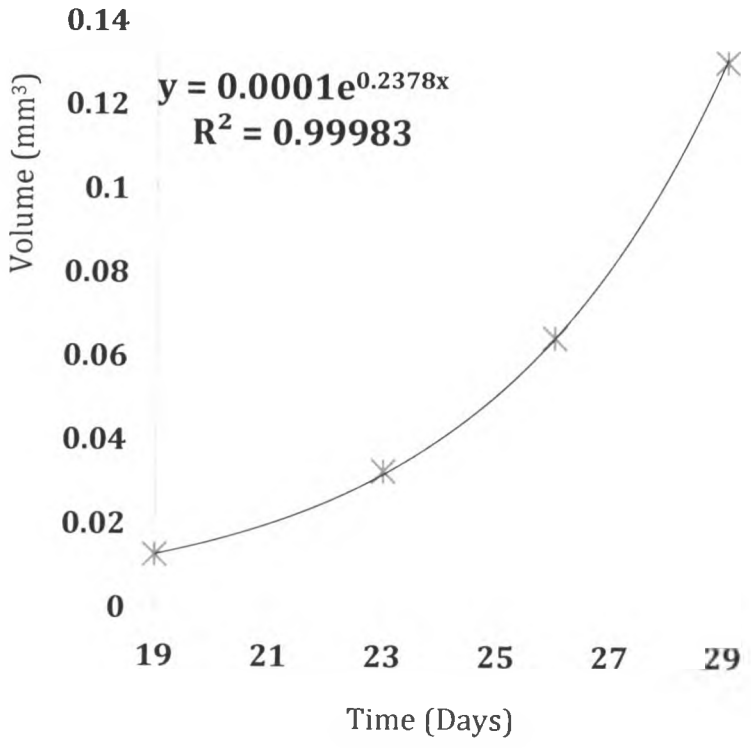
y = 0.0001e^0.2378x
R² = 0.99983
Volume (mm³)
0.14
0.12
0.1
0.08
0.06
0.04
0.02
0
19
21
23
25
27
29
Time (Days)

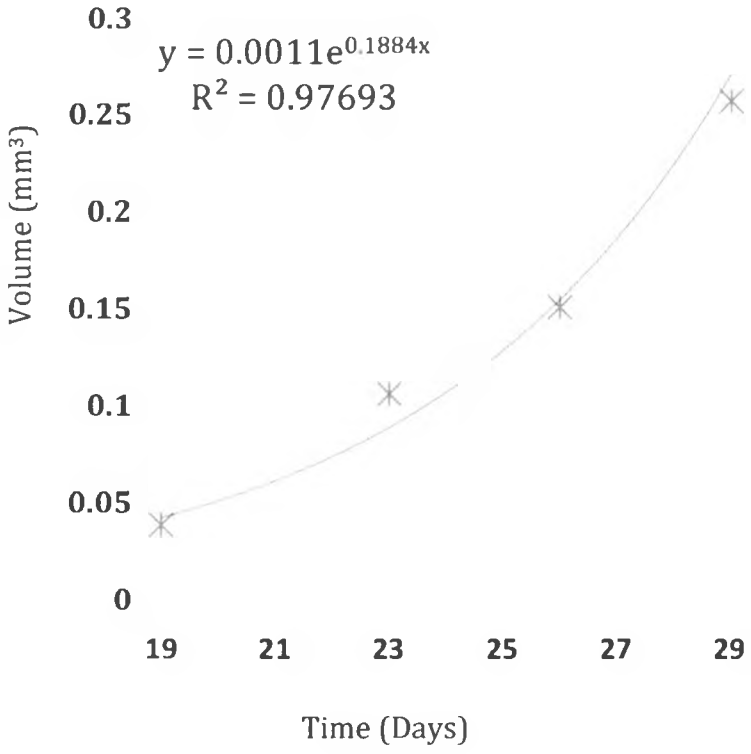
y = 0.0011e^0.1884x
R² = 0.97693
Volume (mm³)
0.3
0.25
0.2
0.15
0.1
0.05
0
19
21
23
25
27
29
Time (Days)

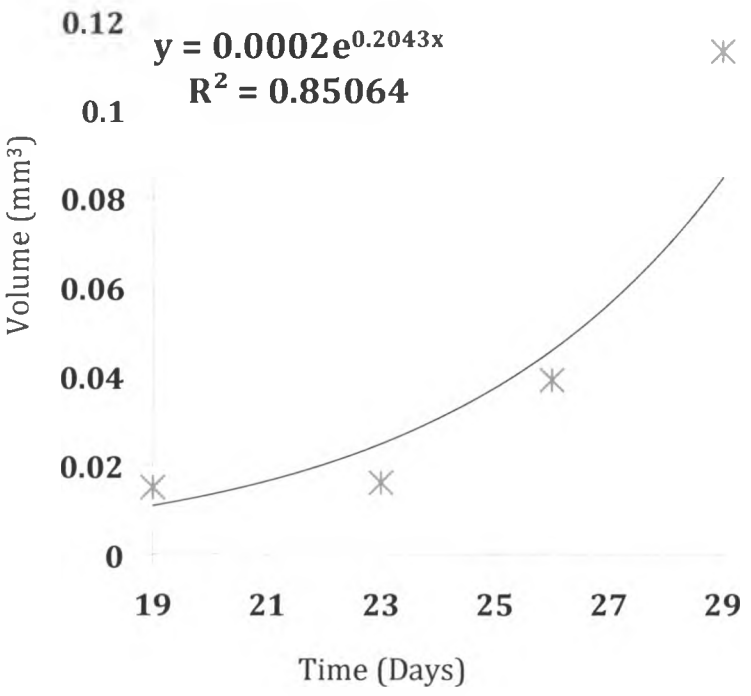
y = 0.0002e^0.2043x
R² = 0.85064
Volume (mm³)
0.12
0.1
0.08
0.06
0.04
0.02
0
19
21
23
25
27
29
Time (Days)

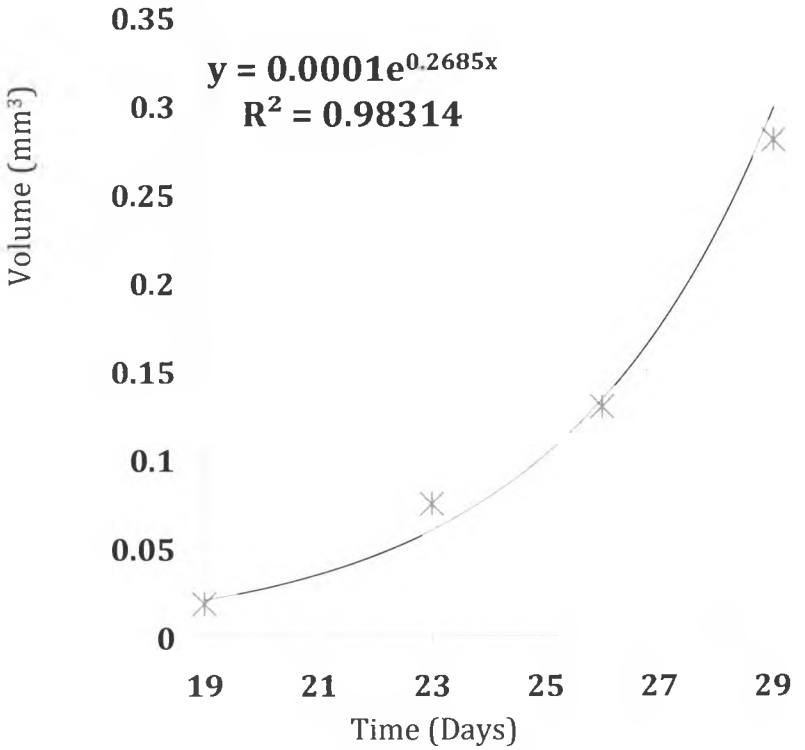
y = 0.0001e^0.2685x
R² = 0.98314
Volume (mm³)
0.35
0.3
0.25
0.2
0.15
0.1
0.05
0
19
21
23
25
27
29
Time (Days)

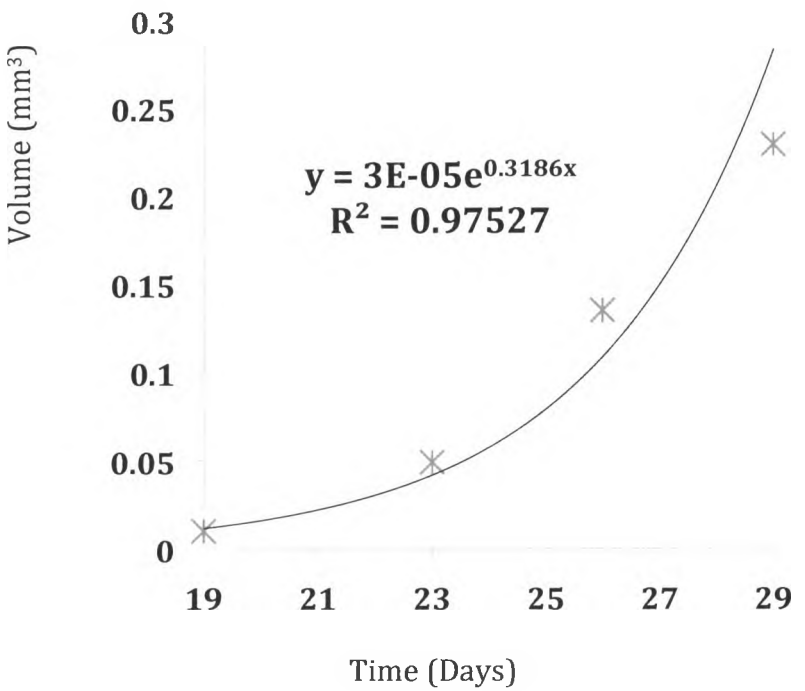
y = 3E-05e^0.3186x
R² = 0.97527
Volume (mm³)
0.3
0.25
0.2
0.15
0.1
0.05
0
19
21
23
25
27
29
Time (Days)

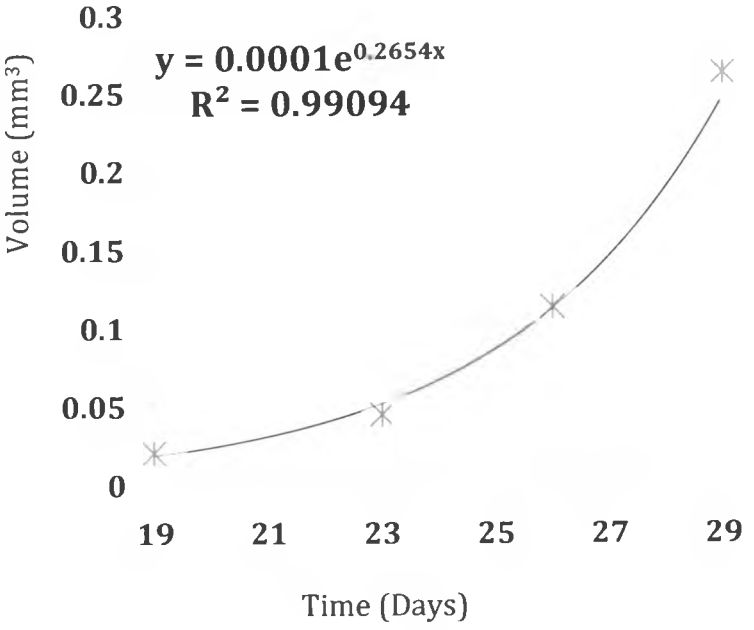
y = 0.0001e^0.2654x
R² = 0.99094
Volume (mm³)
0.3
0.25
0.2
0.15
0.1
0.05
0
19
21
23
25
27
29
Time (Days)

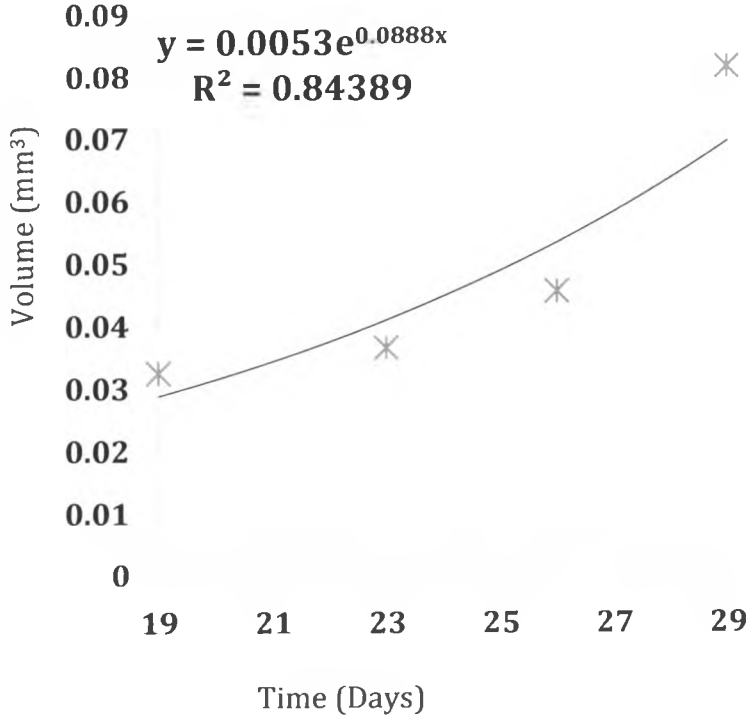
y = 0.0053e^0.0888x
R² = 0.84389
Volume (mm³)
0.09
0.08
0.07
0.06
0.05
0.04
0.03
0.02
0.01
0
19
21
23
25
27
29
Time (Days)

Appendix B

MDA-MB-231BR excel growth rate plots (mouse 4)

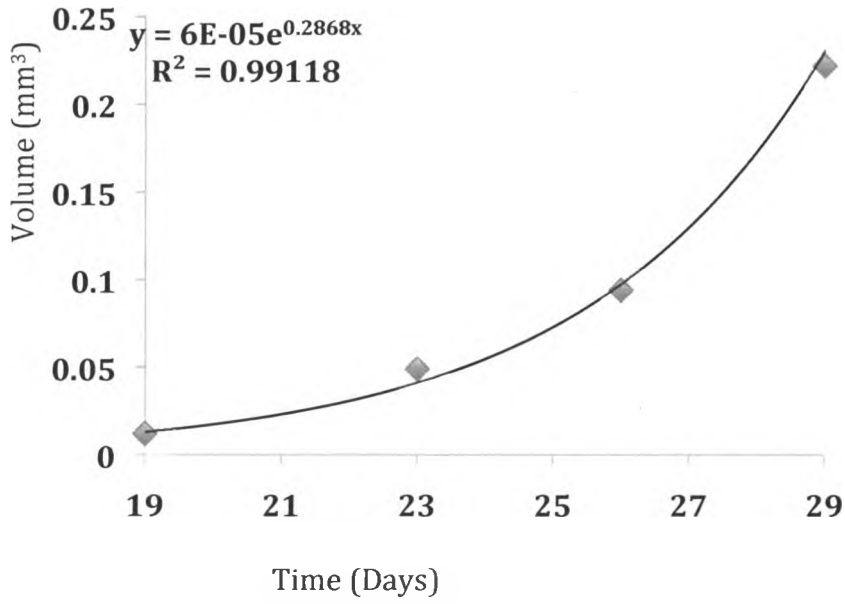

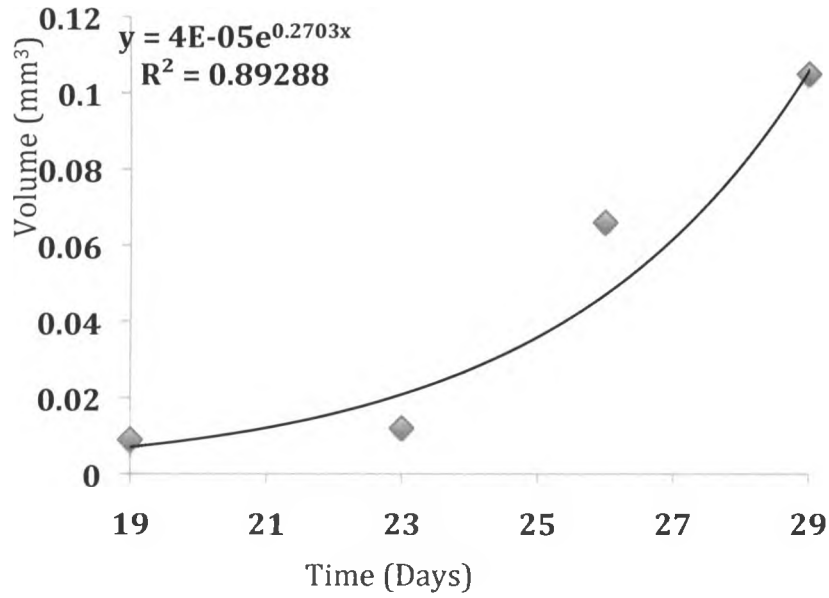

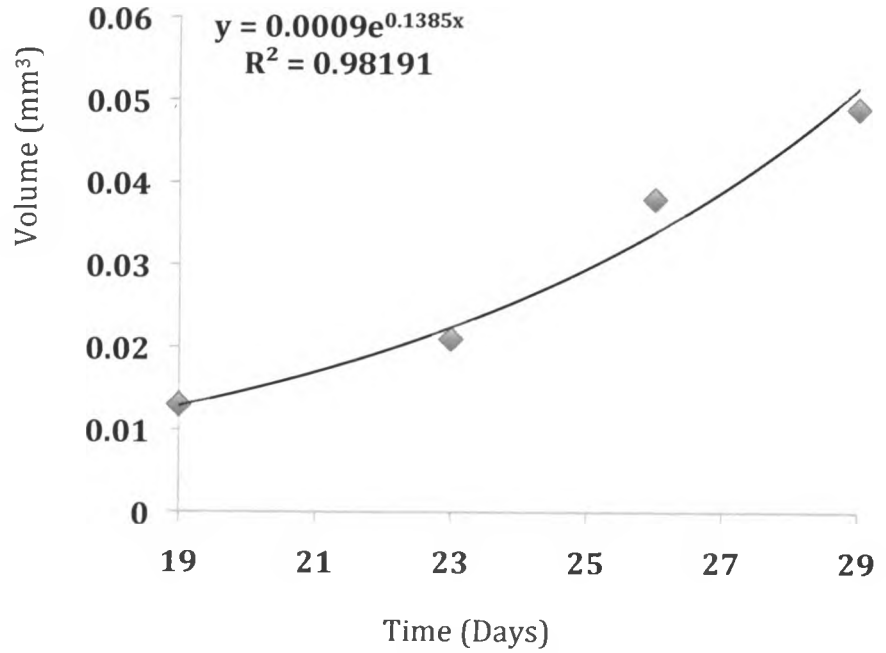
y = 0.0009e^0.1385x
R² = 0.98191
Volume (mm³)
0.06
0.05
0.04
0.03
0.02
0.01
0
19
21
23
25
27
29
Time (Days)

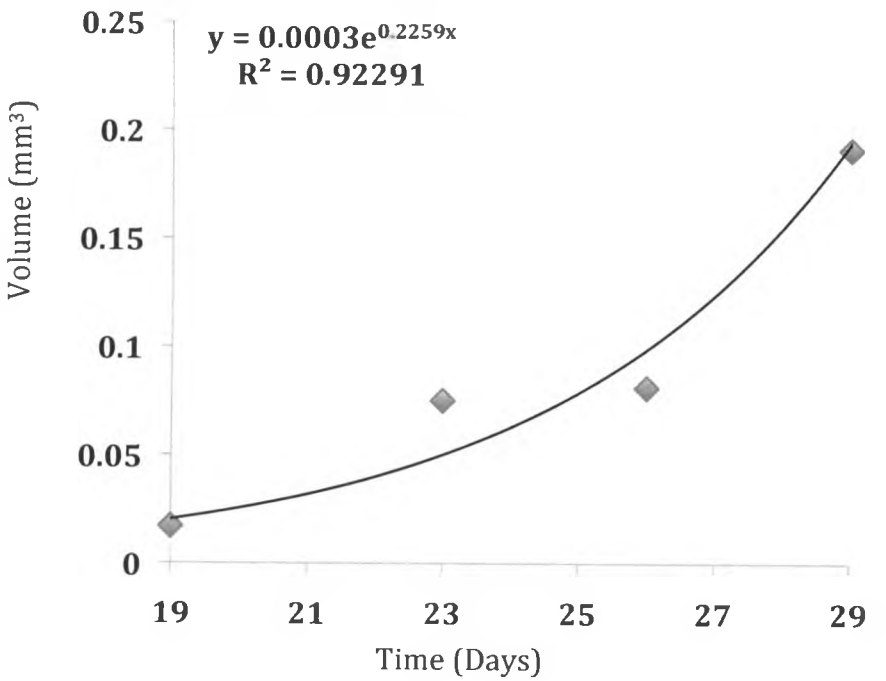
y = 0.0003e^0.2259x
R² = 0.92291
Volume (mm³)
0.25
0.2
0.15
0.1
0.05
0
19
21
23
25
27
29
Time (Days)

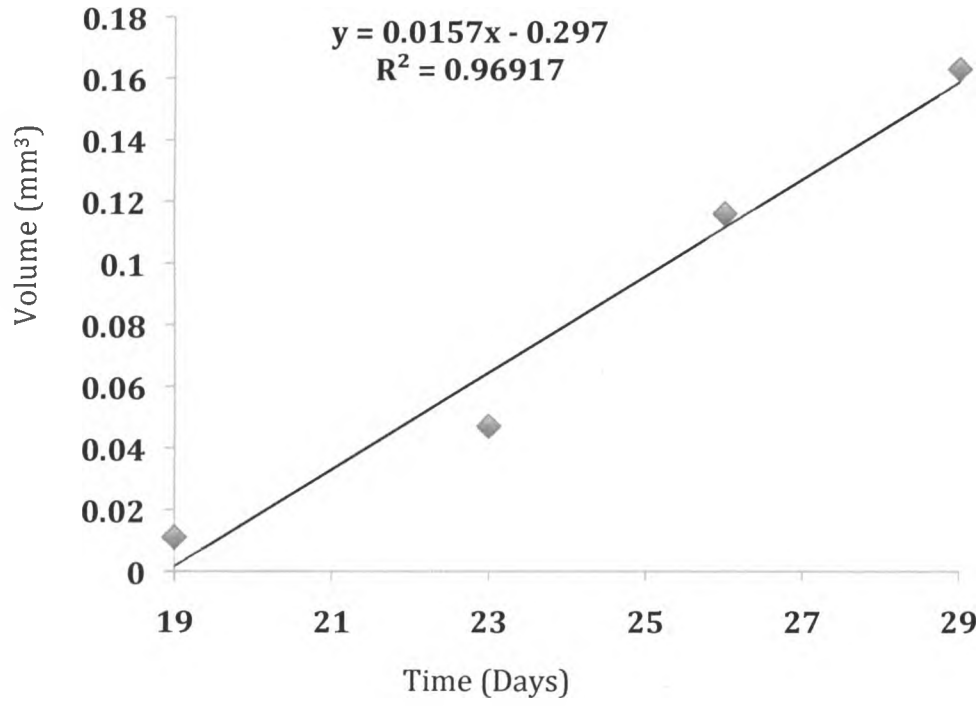
y = 0.0157x - 0.297
R² = 0.96917
Volume (mm³)
0.18
0.16
0.14
0.12
0.1
0.08
0.06
0.04
0.02
0
19
21
23
25
27
29
Time (Days)

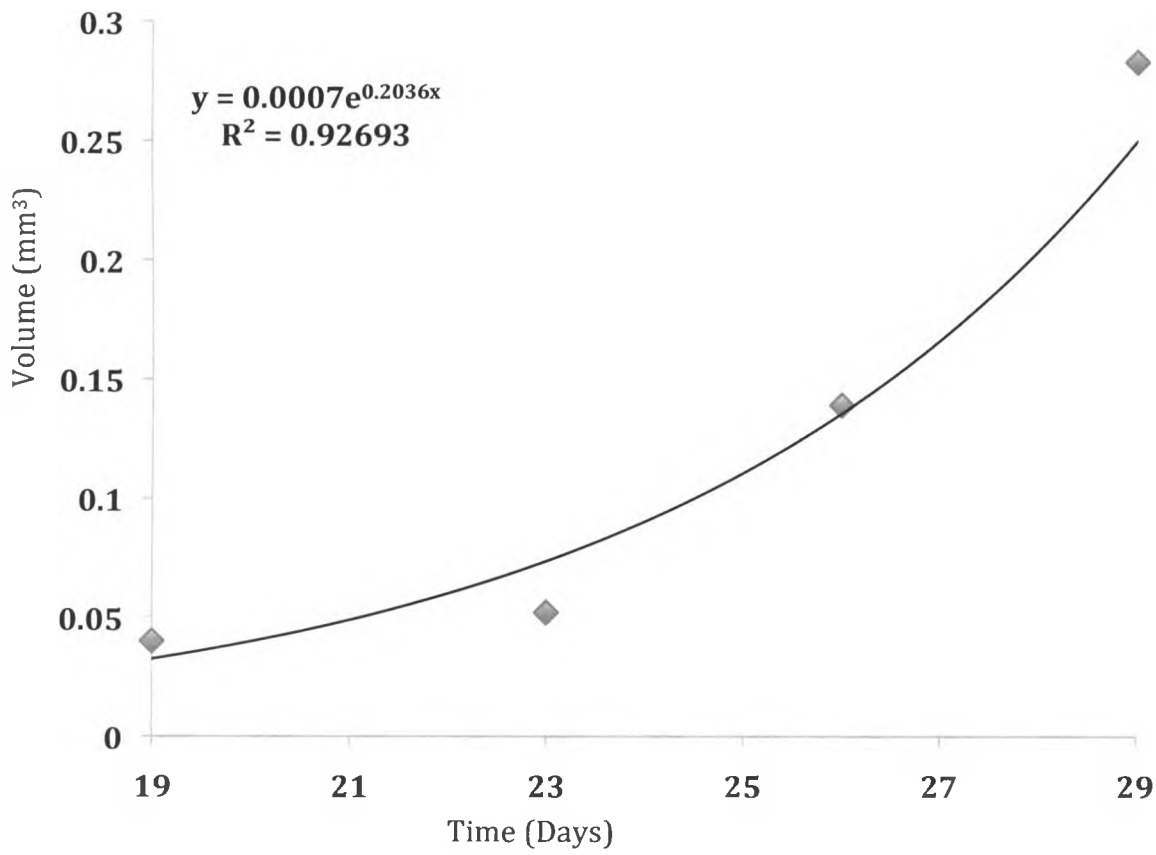
y = 0.0007e^0.2036x
R² = 0.92693
Volume (mm³)
0.3
0.25
0.2
0.15
0.1
0.05
0
19
21
23
25
27
29
Time (Days)

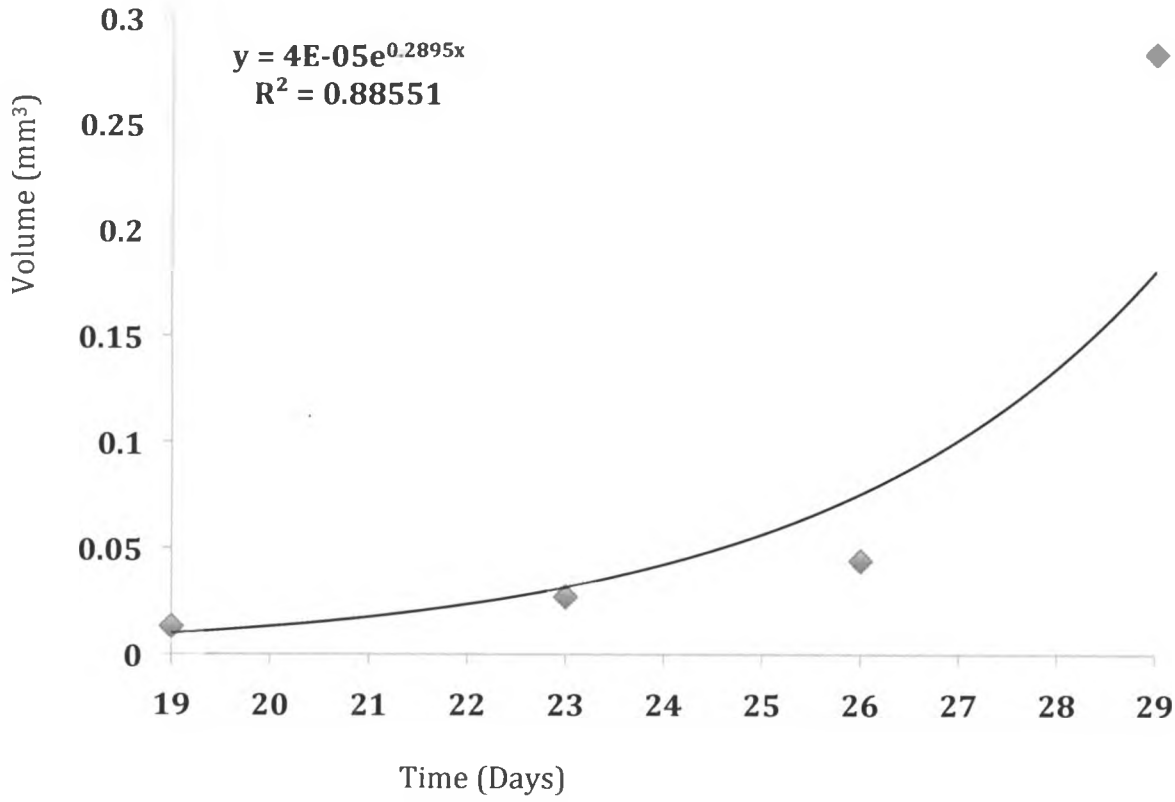
y = 4E-05e^0.2895x
R² = 0.88551
Volume (mm³)
0.3
0.25
0.2
0.15
0.1
0.05
0
19
20
21
22
23
24
25
26
27
28
29
Time (Days)

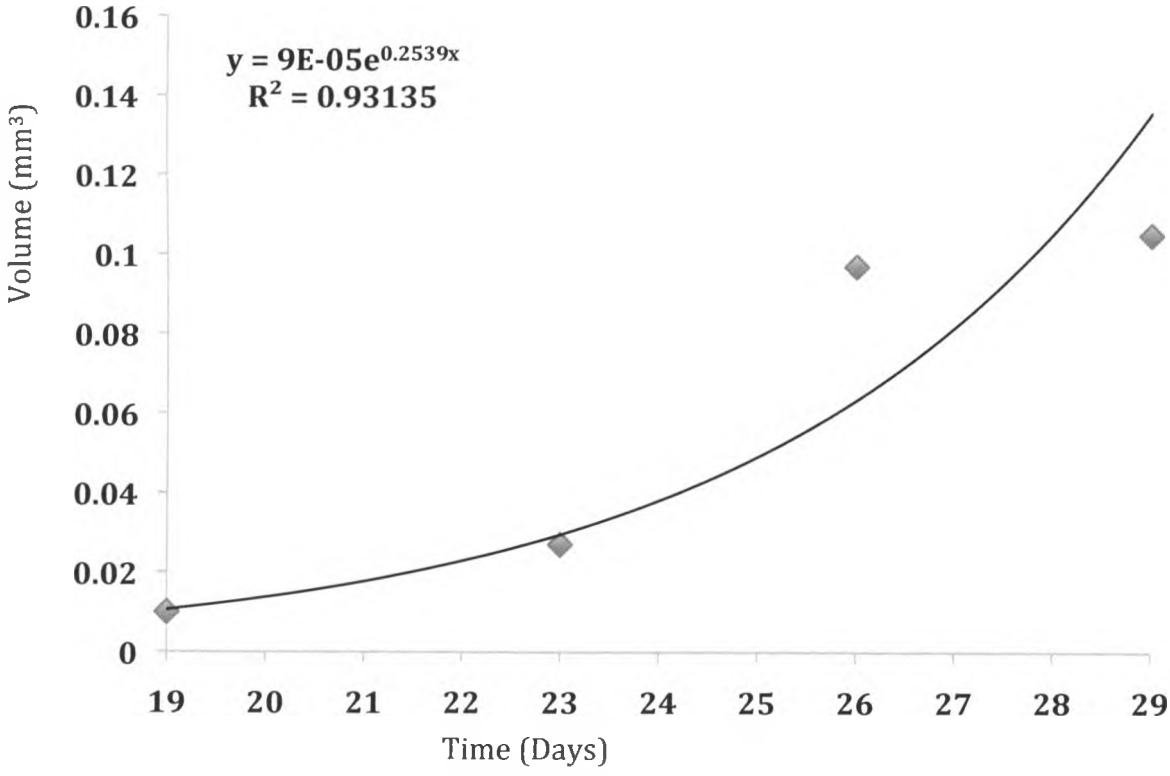
y = 9E-05e^0.2539x
R² = 0.93135
Volume (mm³)
0.16
0.14
0.12
0.1
0.08
0.06
0.04
0.02
0
19
20
21
22
23
24
25
26
27
28
29
Time (Days)

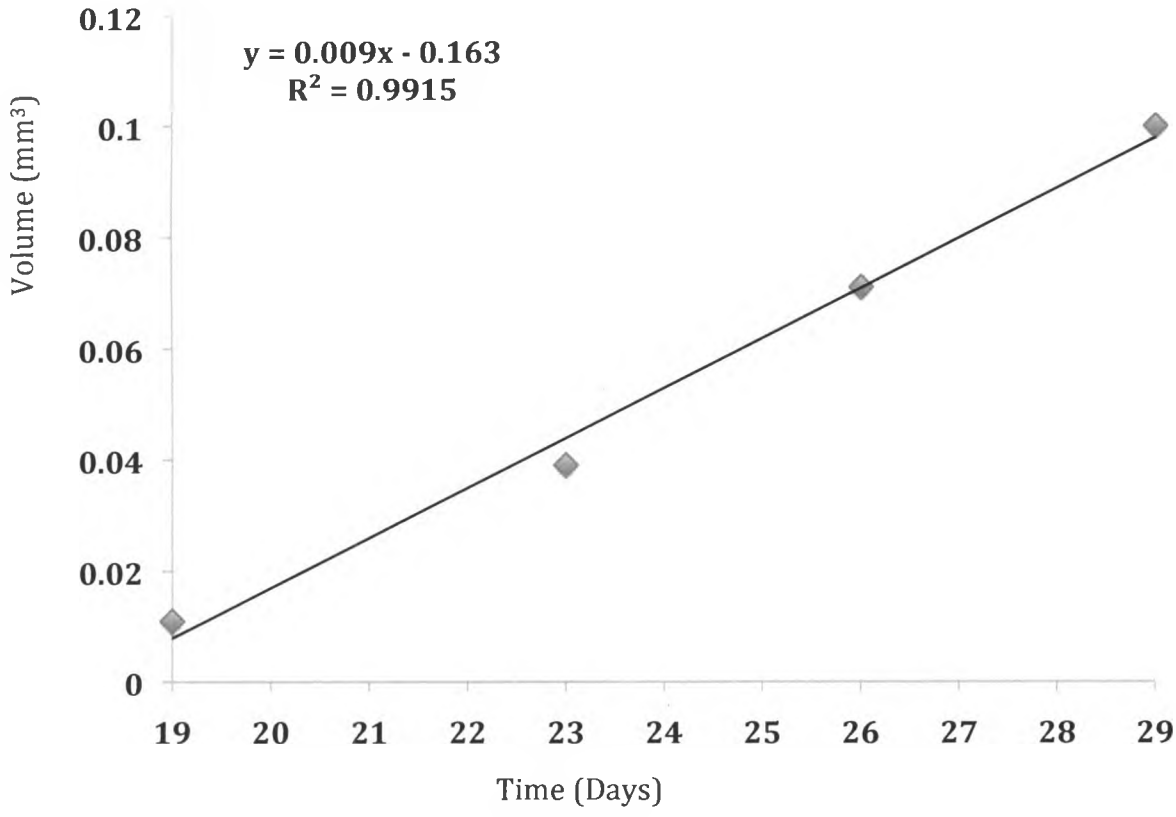
y = 0.009x - 0.163
R² = 0.9915
Volume (mm³)
0.12
0.1
0.08
0.06
0.04
0.02
0
19
20
21
22
23
24
25
26
27
28
29
Time (Days)

Western

04.01.2010
***This is the 3rd Renewal of this protocol**
*A Full Protocol submission will be required in **2011**

Dear Dr **Foster**

Your Animal Use Protocol form entitled:

MRI of Metastasis in the Mouse Brain.

has had its yearly renewal approved by the Animal Use Subcommittee.

This approval is valid from **04.01.2010 to 03.31.2011**

The protocol number for this project remains as **2007-041**

1. This number must be indicated when ordering animals for this project.
2. Animals for other projects may not be ordered under this number.
3. If no number appears please contact this office when grant approval is received.
   If the application for funding is not successful and you wish to proceed with the project, request that an internal scientific peer review be performed by the Animal Use Subcommittee office
4. Purchases of animals other than through this system must be cleared through the ACVS office. Health certificates will be required.

REQUIREMENTS/COMMENTS
Please ensure that individual(s) performing procedures on live animals, as described in this protocol, are familiar with the contents of this document.
The holder of this *Animal Use Protocol* is responsible to ensure that all associated safety components (biosafety, radiation safety, general laboratory safety) comply with institutional safety standards and have received all necessary approvals. Please consult directly with your institutional safety officers.

c.c. M. Pickering, W. Lagerwerf

The University *of* Western Ontario
Animal Use Subcommittee / University Council on Animal Care
Health Sciences Centre. • London, Ontario • CANADA – N6A 5C1
PH: 519-661-2111 ext. 86770 • FL 519-661-2028 • www.uwo.ca / animal